FIRAT UNIVERSITY
GRADUATE SCHOOL OF NATURAL AND APPLIED SCIENCES
TÜRKİYE

THEORETICAL MODELING AND EXPERIMENTAL CHARACTERIZATION OF ERBIUM-BASED HYDROXYAPATITES DOPED WITH DIFFERENT ELEMENTS AND QUANTUM CHEMICAL STUDY OF SOME BASIC ORGANIC COMPOUNDS

Lana Omar AHMED

Doctoral Thesis

DEPARTMENT OF PHYSICS
Division of
Atomic and Molecular Physics

JUNE 2023

FIRAT UNIVERSITY
GRADUATE SCHOOL OF NATURAL AND APPLIED SCIENCES
TÜRKİYE

Department of Physics

Doctoral Thesis

THEORETICAL MODELING AND EXPERIMENTAL CHARACTERIZATION OF ERBIUM-BASED HYDROXYAPATITES DOPED WITH DIFFERENT ELEMENTS AND QUANTUM CHEMICAL STUDY OF SOME BASIC ORGANIC COMPOUNDS

Author
Lana Omar AHMED

Supervisor
Prof. Dr. Niyazi BULUT

JUNE 2023
ELAZIG

FIRAT UNIVERSITY
GRADUATE SCHOOL OF NATURAL AND APPLIED SCIENCES
TÜRKİYE

Department of Physics

Doctoral Thesis

Title:	Theoretical Modeling and Experimental Characterization of Erbium-Based Hydroxyapatites Doped with Different Elements and Quantum Chemical Study of Some Basic Organic Compounds
Author:	Lana Omar AHMED
Submission Date:	25 May 2023
Defense Date:	15 June 2023

THESIS APPROVAL

This thesis, which was prepared according to the thesis writing rules of the Graduate School of Natural and Applied Sciences, Fırat University, was evaluated by the committee members who have signed the following signatures and was unanimously approved after the defense exam made open to the academic audience.

		Signature
Supervisor:	Prof. Dr. Niyazi BULUT Firat University, Faculty of Science	Approved
Chair:	Prof. Dr. Sinan AKPINAR Firat University, Faculty of Science	Approved
Member:	Prof. Dr. Hikmet KEMALOĞLU Firat University, Faculty of Science	Approved
Member:	Assoc. Prof. Dr. Emine TANIŞ Kirsehir Ahi Evran University , Faculty of Engineering and Architecture	Approved
Member:	Assoc. Prof. Dr. Tankut ATEŞ Malatya Turgut Özal University, Faculty of Engineering and Natural Sciences	Approved

This thesis was approved by the Administrative Board of the Graduate School on

.... / .... / 20 ....

Signature

Prof. Dr. Burhan ERGEN
Director of the Graduate School

DECLARATION

I hereby declare that I wrote this Doctoral Thesis titled “Theoretical Modeling and Experimental Characterization of Erbium-Based Hydroxyapatites Doped with Different Elements and Quantum Chemical Study of Some Basic Organic Compounds ” in consistent with the thesis writing guide of the Graduate School of Natural and Applied Sciences, Firat University. I also declare that all information in it is correct, that I acted according to scientific ethics in producing and presenting the findings, cited all the references I used, express all institutions or organizations or persons who supported the thesis financially. I have never used the data and information I provide here in order to get a degree in any way.

15 June 2023

Lana Omar AHMED

PREFACE

Bones and teeth are vital components of both humans and animals, and they can be harmed by cracks and fractures. To remain healthy, these parts must be fixed. Hydroxyapatite (HAp) in particular is an effective aid in the repair of these damaged areas. Because HAp is a bioactive, osteoinductivity, and osteoconductive implanting substance, using it to repair bones and teeth will almost certainly give favorable results (for example, its accelerated effects on bone growth) for the treatment. It is so important that the production of HAp must be done at lower costs. In addition, in comparison with the standard HAp, HAp samples have to be created with enhanced properties. In this situation, before experimental methods are performed, theoretical comments might yield some relevant conclusions.

I would like to express my heartfelt gratitude and appreciation to my supervisor, Prof. Dr. Niyazi BULUT, who has always assisted and supported me throughout my studies and project. I would also like to thank Assoc. Prof. Dr. Ömer KAYILI, for his guidance and great contributions to the practical study of my thesis. Thank you very much to my husband and parents for their constant support and willingness to give up their rights for the sake of my progress.

Lana Omar AHMED
ELAZIG, 2023

CONTENTS

ABSTRACT

Theoretical Modeling and Experimental Characterization of Erbium-Based Hydroxyapatites Doped with Different Elements and Quantum Chemical Study of Some Basic Organic Compounds

Lana Omar AHMED

Doctoral Thesis

FIRAT UNIVERSITY
Graduate School of Natural and Applied Sciences

Department of Physics

June 2023, Page: iv + 102

In this thesis, different hydroxyapatites based on erbium are theoretically and experimentally characterized, and certain basic organic compounds are subjected to quantum chemical analysis. This is the first theoretical and experimental analysis of co-doped hydroxyapatite (HAp) structures including yttrium (Y), cerium (Ce), praseodymium (Pr), and erbium (Er). By altering the concentration of Y, Ce, and Pr amounts of 0.13, 0.26, 0.39, 0.52, 0.65, and 0.78 at.%, while Er was maintained fixed at 0.39 at.%, the materials were created utilizing a wet chemical process. The produced samples underwent spectroscopic, thermal, and *in vitro* biocompatibility testing. The energy bandgap, density of states, and linear absorption coefficient were calculated theoretically. The research was done on the impacts of Y, Ce, and Pr concentration on thermal, morphological, and structural factors. The creation of the HAp structure in the samples was verified by Raman and Infrared (FTIR) spectroscopies. Theoretical studies showed that except for the sample containing 0.39 at.% of the dopant, which showed a drop in the bandgap, increasing the quantity of Y increased density from 3.1724 g cm^{-3} to 3.1824 g cm^{-3} and lowered bandgap energy from 4.196 eV to 4.156 eV. In addition by adding Ce atoms at various amounts, the density increased from 3.1745 to 3.1950 g cm^{-3} and the bandgap energy decreased gradually from 4.1591 eV to 4.1053 eV, except for 0.26Ce-0.39Er-HAp and 0.52Ce-0.39Er-HAp, where the energy bandgap raised. Also, the theoretical results demonstrated an increase in the density from 3.154 to 3.179 g cm-3, as well as steady decreases in the bandgap from 4.1739 to 4.0618 eV by adding Pr atoms. The values of linear absorption appeared reduced with an increase in photon energy. The cell viability was affected by the co-dopant content, and this value was found higher than 83% for all the samples.

Quantum mechanical methods were used to examine the corrosion-inhibiting properties of 10 molecules (Benzene (C1), Phenol (C2), Toluene (C3), Benzoic acid (C4), Acetophenone (C5), Chlorobenzene (C6), Bromobenzene (C7), Benzaldehyde (C8), Naphthalene (C9), and Anthracene (C10). The results demonstrated that the behavior of organic-based corrosion inhibitors is connected to the performance of good corrosion inhibitors.

Keywords: Hydroxyapatite, bandgap, X-ray diffraction, spectroscopic analysis, cell viability, DFT, corrosion inhibitors

ÖZET

Farklı Elementlerle Katkılanmış Erbiyum Esaslı Hidroksiapatitlerin Teorik Modellenmesi ve Deneysel Karakterizasyonu ve Bazı Temel Organik Bileşiklerin Kuantum Kimyasal Çalışması

Lana Omar AHMED

Doktora Tezi

FIRAT ÜNİVERSİTESİ
Fen Bilimleri Enstitüsü

Fizik Anabilim Dalı

Haziran 2023, Sayfa: iv + 102

Bu tezde, erbiyum bazlı farklı hidroksiapatitlerin teorik ve deneysel olarak karakterize edilmesi ve bazı temel organik bileşiklerin kuantum kimyasal analizlerine tabi tutulması amaçlanmaktadır. Bu, itriyum (Y), seryum (Ce), praseodim (Pr) ve erbiyum (Er) dahil olmak üzere ortak katkılı hidroksiapatit (HAp) yapılarının ilk teorik ve deneysel analizidir. Y, Ce ve Pr konsantrasyonlarının 0.13, 0.26, 0.39, 0.52, 0.65 ve 0.78 at.%'lik konsantrasyonlarının pratik olarak her 10 kalsiyum atomunda değiştirilmesiyle, Er ise 0.39 at.%'de sabit tutulurken, malzemeler oluşturuldu ıslak bir kimyasal işlem kullanarak. Üretilen numuneler spektroskopik, termal ve *in vitro* biyouyumluluk testlerine tabi tutuldu. Enerji bant aralığı, durum yoğunluğu ve lineer absorpsiyon katsayısı teorik olarak hesaplandı. Y, Ce ve Pr konsantrasyonunun termal, morfolojik ve yapısal faktörler üzerindeki etkileri üzerine araştırmalar yapılmıştır. Numunelerde HAp yapısının oluşturulması, Raman ve Kızılötesi (FTIR) spektroskopileri ile doğrulanmıştır. Teorik çalışmalar, bant aralığında düşüş gösteren %0.39 at.% katkı maddesi içeren numune dışında, Y miktarını artırmanın yoğunluğu 3.1724 g cm^{-3}'ten 3.1824 g cm^{-3}'e yükselttiğini ve bant aralığını düşürdüğünü göstermiştir. enerji 4.196 eV'den 4.156 eV'ye. Ayrıca çeşitli miktarlarda Ce atomları eklenerek yoğunluk 3,1745'ten 3,1950 gcm^{-3}'e yükselmiş ve bant aralığı enerjisi 0,26Ce-0,39Er-HAp ve 0,52Ce-0,39Er- hariç kademeli olarak 4,1591 eV'den 4,1053 eV'a düşmüştür. HAp, enerji bant aralığının yükseldiği yer. Ayrıca teorik sonuçlar, Pr atomlarının eklenmesiyle yoğunluğun 3,154'ten 3,179 gcm^{-3}'e yükseldiğini ve bant aralığında 4,1739'dan 4,0618 eV'ye sürekli düşüşler gösterdi. Doğrusal absorpsiyon değerleri ortaya çıktıfoton enerjisindeki artışla azaldı. Hücre canlılığı ko-dopant içeriğinden etkilenmiş ve bu değer tüm örnekler için %83'ün üzerinde bulunmuştur.

10 molekülün (Benzen (C1), Fenol (C2), Toluen (C3), Benzoik asit (C4), Asetofenon (C5), Klorobenzen (C6), Bromobenzen (C7) korozyon önleyici özelliklerini incelemek için kuantum mekanik yöntemler kullanılmıştır. , Benzaldehit (C8), Naftalin (C9) ve Antrasen (C10) Sonuçlar, organik bazlı korozyon inhibitörlerinin davranışının, iyi korozyon inhibitörlerinin performansıyla bağlantılı olduğunu göstermiştir.

Anahtar Kelimeler: Hidroksiapatit, bant aralığı, X-ışını kırınımı, spektroskopik analiz, hücre canlılığı, DFT, korozyon inhibitörleri

LIST OF FIGURES

Page

LIST OF TABLES

LIST OF APPENDICES

Page

LIST OF SYMBOLS ABBREVIATIONS

Symbols

μ : Dipole moment

a, b and c : Lattice parameters

at.% : Atomic percent

C_p : Specific heat capacity

D_S : Crystallite size (calculated from Scherrer equation)

D_{WH} : Crystallite size (calculated from Williamson-Hall equation)

Eg : Band gap energy

eV : Electron volt

ε : Lattice strain

h : Hour

min : Minute

ºC : Degree Celsius

u : Anisotropic energy density

u : Anisotropic energy density

V : Volume of the unit cell

wt.% : Weight percent

X_C% : Crystallinity percentage calculated from general equation

X_{CL}% : Crystallinity percentage calculated from Landi equation

α, β, γ : Angles

ΔE : Energy difference

ΔN : Electron transmit fraction

θ : Diffraction angle

λ : Wavelength

σ : Lattice stress

LIST OF ABBREVIATIONS

Abbreviations

AD :	Anno Domini (in the year of the lord)
BC :	Before Christ
DFT :	Density functional theory
DOS :	Density of states
DTA :	Differential thermal analysis
EDX :	Energy dispersive X-ray
FTIR :	Fourier transform infrared
FWHM :	Full width at half maximum
HAp :	Hydroxyapatite
HOMO :	Higher Occupied Molecular Orbital
IB :	Index of bioactivity
SEM :	Scanning electron microscopy
TGA :	Thermogravimetric analysis
XRD :	X-ray diffraction
α-TCP :	Alpha tricalcium phosphate
β-TCP :	Beta tricalcium phosphate
LUMO :	Lower Unoccupied Molecular Orbital

1. INTRODUCTION

Since the beginning of human existence on this planet, people have been striving to improve their quality of life and obtain their needs. Science would be the only aspect that improves and simplifies human life. Furthermore, one of the most essential areas of research is material science.

In material science, researchers have investigated the relationships between the structures, characteristics, preparation processes, and application functions, which is an interdisciplinary field concerned with recognizing and applying the properties of materials. It consists of various types of materials, with biomaterials being one of the most important and useful types [1].

Biomaterials are natural or synthetic materials that are used to replace damaged tissue or organs when they interact with a biological system. The origins of biomaterials can be traced back to gold and ivory. Egyptians and Romans used these materials before the twentieth century. Biomaterials differ from other materials in that they are biocompatible with the human biological system. As a result, it's a fascinating material in the medical field, and it's used in a variety of medical application fields [2, 3]. Synthetic biomaterials have been used in place of natural biomaterials for the past fifty years, and the field has grown rapidly. They are used in medical devices because they improve performance and reproducibility. As a result of this progress, biomaterials are being used more frequently. Whenever and wherever, devices including hip joints, heart valves, and bone implants have saved or made life better for a huge number of people [4, 5]. The application of biomaterials is expanding every day because of human illnesses and accidents. Furthermore, as the population grows, more patients require orthopedic surgery [6]. These investigations already relate to the use of biomaterials for bone regeneration, cardiovascular fixing, and recovery [7, 8]. Metal, polymer, composite, and ceramic biomaterials with variable degrees of bioactivity have been divided into separate groups based on their chemical, structural, and biological features [9]. For load-bearing applications such as the replacement of joints, screws, and bone plates, metallic materials are typically used. Polymer biomaterials have been commonly used in non-load-bearing clinical applications including facial prosthesis, cardiovascular prosthesis, drug delivery, and cartilage. Enhanced polymers were used as fillers, anti-adhesion materials, and coatings and were available in a variety of forms (film, liquid, and gel). Composite materials, on the other hand, are a relatively new class of biomaterials that can be natural, synthetic, or a combination of both, and were extensively used in orthopedic surgery [10, 11].

Ceramic biomaterials are another kind and are amazingly biocompatible, brittle, and corrosion-resistant. They can be used in the replacement of bone and bone regeneration due to their brittleness. In addition to the load-bearing applications, they are poor resistance, which is why they mainly use tissue implants as a covering on solid surfaces. Bioceramic products exhibit the excellent properties necessary in orthopedics and have a strong focus on biomedical applications

[10]. Hydroxyapatite (HAp) is one of the most significant ceramics because it is nearly identical to the inorganic component of bones and teeth. It also has some essentially vital characteristics. Due to its excellent biocompatibility, thermal stability, high bioactivity, and nontoxicity, it has found widespread use in the biomedical field. Because of its poor mechanical properties, hydroxyapatite's use in orthopedics is restricted. Moreover, hydroxyapatite can replace its ions with a variety of foreign ions, optimizing biocompatibility, mechanical properties, and microstructure [12, 13]. Sol-gel, hydrothermal, mechanochemical, combustion, spray pyrolysis, and wet chemical techniques have all been constructed to synthesize HAp nanostructures. Besides, the hydroxyapatite properties can be altered or controlled by the synthesis methods [14]. The wet chemical procedure was introduced to synthesize HAp nanoparticles with the lowest and most homogeneous impurity and is widely used by researchers due to their low cost, clarity, and low-temperature response [15]. Rare earth elements are nowadays one of the most widely used materials in biotechnology. Erbium (Er) is a rare element of the globe and is found in ribbons and kidneys. Additionally, (Er) can be added as a dopant to help enhance the biological properties of hydroxyapatite [16]. Erbium is also essential for doping into another material, for increased luminescence and biocompatibility, as the emission of erbium is good and biocompatible. This element is therefore used in optical engineering and the process of bone healing [17].

In this thesis, erbium (Er)-based hydroxyapatite (HAp) samples doped with different elements will be modeled by using the density functional theory (DFT) calculations and the as-modeled systems will also be produced experimentally using the wet chemical route. The theoretical parameters such as the bandgap and density of states (DOS) will be estimated. The experimental characterization of the samples will be done using X-ray diffraction (XRD), Fourier transforms infrared (FTIR) spectroscopy, thermogravimetric analysis (TGA), differential thermal analysis (DTA), and scanning electron microscopy (SEM). The effects of the selected different elements on the as-investigated properties will be determined both theoretically and experimentally and reported. It is thought that there will be contributed to the literature after obtaining all the results related to this thesis.

2. A SHORT HISTORY OF BIOMATERIALS

The term "biomaterial" was developed in the mid-twentieth century, although biomaterials have been around for much longer [18]. The background of biomaterials reveals a constant increase in interest in utilizing foreign materials to treat and restore the human body, and the capacity to utilize increasingly complex substances for these reasons. The first use of biomaterials for medical reasons goes back to 3000 BC in Egypt with the use of linen sutures, as well as from AD 600 with the use of seashells for prosthetic teeth [18].

The 18th and 19th centuries showed significant advances in biomaterials. Researchers started to notice that a material's biocompatibility plays a significant influence on its effectiveness when used in a biological system. Doctors Lapuyade and Sicre from Toulouse introduced the first metal wire method for bone fracture repair in 1775. H. S. Levert's study of metal implants (gold, silver, lead, and platinum) and bone fixation plates in dogs from the mid to late 1800s focused on the biocompatibility of metal implants. Adolf Fick invented the first effective glass contact lens in 1888, while Leonardo da Vinci sketched the concept much earlier, in 1508 [19].

Other significant milestones in the invention and development of biomaterials occurred from the second half of the 19th century to the first half of the 20th century [5].

2.1 Types of Biomaterials

Metallic materials, polymers, ceramics, composites, and natural materials are the major categories of materials utilized in the manufacture of bio-implants and bio-devices [20].

2.1.1 Metals

Resistance, strength, toughness, and fracture are all excellent mechanical properties of metallic biomaterials. Figure 2.1 showed an important type of metallic material utilized in many medical applications, including load-bearing implants such as hip and knee prostheses, as well as it showed the tools such as pins, screws, and plates. But, due to the corrosive properties of certain metals in the human body, their usage would be limited. As a result, the corrosion and wear resistance of metals employed in the body must be adequate. Therefore, alloys (metals consisting of two or more elements) are employed for metallic implants. Stainless steel, Co-Cr Mo, and Ti alloys are the three types of metallic biomaterials [21, 22].

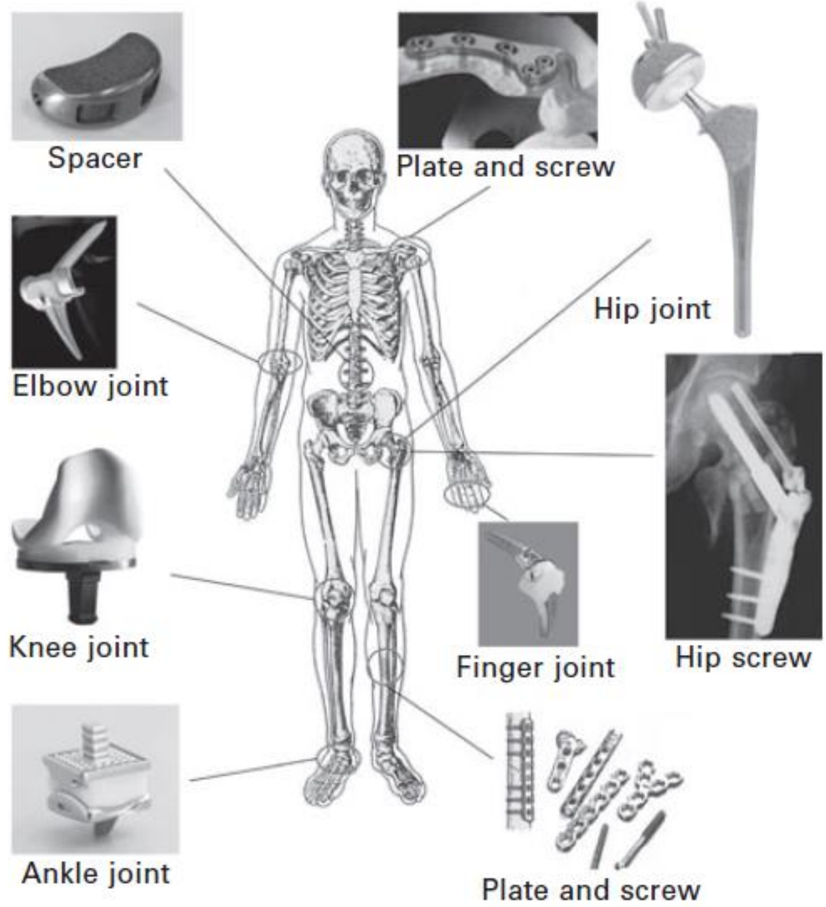

Figure 2.1. Metals used in biomedical devices. Plates, pins, orthodontists, rods, and hip replacements are all made from metal [23].

This applies to any sort of hard tissue in our organs. Despite metallic biomaterials offering unique mechanical characteristics, they have significant drawbacks in that they readily corrode after implantation in the body and have toxicity, which may affect the living organs where they are fixed. When choosing metals and alloys, the host system's surrounding environment must be considered [24].

2.1.2 Biopolymers

In the mid-twentieth century, a breakthrough in polymer findings led to a wide range of polymers being used for medical purposes [25]. Polymers are observed in both synthetic and natural forms and are composed of groups of joined atoms that come together to create molecules with a high molecular weight. As shown in Figure 2.2, synthetic polymer materials such as (polyethylene, polypropylene, and poly (methyl methacrylate): PMMA.) are widely used as medical materials due to their unique properties such as biodegradability, biocompatibility, lightweight, flexibility, reasonable cost, and non-corrosive, and ease of manufacturing to generate different forms [26]. Due to their lower strength than metals, only a few polymers have been used for bone implants [27].

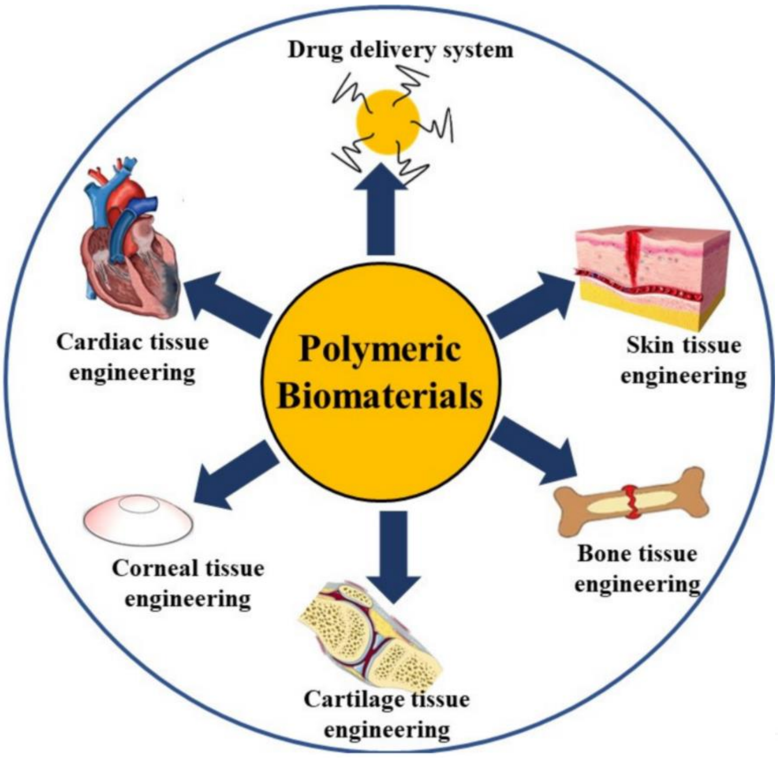

Figure 2.2. Polymeric biomaterial uses in various biological fields [28].

2.1.3 Bioceramics

Bioceramics are synthetic materials that are refractory polycrystalline compounds used in the human musculoskeletal system to repair and replace damaged or diseased tissue [29]. Before 1925, pure metals were commonly used in surgical implant materials. The metallic alloys were first employed in surgical implants, such as Vitallium, in 1930. L.L. Hench discovered new materials in 1969, including glass and ceramics that could bond with the bone. L.L. Hench has begun testing bioceramic implants for soldiers who were injured in the Vietnam War; however, some of the implants have been rejected by the body. As a result, Hench examined biocompatible materials. As a consequence, he discovered bioglass and his interest in bioceramics grew fast as result of his discovery [30, 31]. For many years, bioceramics have been extensively employed for medical uses due to highly desirable properties such as chemical stability, biocompatibility, and non-toxicity. Because of their hardness and brittleness, bioceramics are only suitable for some load-bearing applications in medicine. They also have high compressive strength and wear resistance, and as a result of these qualities, they have been approved in dental repairs and certain specific orthopedic applications as a portion of a synthetic joint. Bone defect repair, alveolar bridge maintenance, augmentation, hip joint implant, and ear implant are some of the medical applications for bioceramics. Because of their biocompatibility and the ability to restore, they have also been employed in drug delivery systems. The use of bioceramics in healthcare applications has saved or improved the lives of millions of people [32, 33].

Bioceramics have important functions such as having a low friction coefficient for lubrication joint surfaces, being able to be put on the surfaces of the heart muscle to avoid blood coagulation, and acting as a stimulating substance for bone development [34]

2.1.3.1 Types of Bioceramics

Bioceramics are divided into three categories based on their structural function and characteristics (inert bioceramics, bioactive bioceramics, and biodegradable bioceramics)

2.1.3.1.1 Inert Bioceramics

Bioinert ceramics are materials that, due to their chemical stability, do not react with the host tissue when implanted in a living system. Alumina (Al_2O_3) and Zirconia (ZrO_2) are the two most common forms. Compared to Cobalt-Chrome alloy or Stainless Steel, they have more interesting mechanical properties, greater bending and compressive strength, and higher biocompatibility. Alumina was first used for artificial bone and joint implants in the 1980s due to its desired qualities [35]. Alumina ceramics have a hexagonal crystal structure that gives the highest chemical stability when implanted in the human body (i.e. crystallographic stability). On the other hand, Zirconia exhibits three crystallographic phases: cubic, monoclinic, and tetragonal. Mechanical stress, temperature fluctuation, and moisture are all factors that cause a phase change. The phase change sometimes can cause self-damage to the ceramic [36].

2.1.3.1.2 Bioactive Ceramics

Bioactive ceramics are materials that form a direct bond with the host tissue after being implanted into a live system. The bioactive materials are mostly made of ceramics, glass, or glass-ceramics, and they contain calcium (Ca) and silicon (Si) ions, as well as calcium phosphates (CaP) like HAp. Larry Hench, 50 years ago, was the first to investigate the use of glass in the body for bone repair. The interfacial bond between the host tissue and the implanted materials is tolerated by forming a bioactive carbonate-hydroxyl layer that is identical to the inorganic composition phase of bone [37, 38]. In comparison to other glass and glass-ceramics used in medical applications, the glass-ceramic has improved mechanical characteristics such as bending strength, young modulus, and fracture toughness. This enables glass-ceramics to be employed in certain load-bearing compression sectors in bone orthopedics. Adopted to increase bioactive ceramic usage were mostly focused on two areas. In the beginning, construct (organic-inorganic) composites for use in tissue regeneration and coatings on the surface of metallic surfaces for applications requiring high mechanical characteristics. Next, make a porous substance with a proper bioactive reaction that can be enhanced by adding biological molecules or inorganic therapeutic ions used in hard tissue engineering [39]. In terms of their index of bioactivity, the material bioactivity rate may be divided into two types (IB). The first category includes materials with an IB value of more than 8, like (glass-ceramic and bioactive glass), which actively react with tissues, causing intrinsic healing and regeneration as well as bonding to hard and soft tissue. The second one has an IB value of more than 0 but less than 8, and these materials are just osteoconductive, such as (HAp and TCP) [40].

2.1.3.1.3 Biodegradable Ceramics

Biodegradable ceramics are ceramics that break down chemically in the bodily fluid after being implanted in the body. In addition, as compared to bioinert ceramics, the biodegradable ceramics' interface with bone is not as stable. Tricalcium phosphate (TCP), hydroxyapatite (HAp), octacalcium phosphate (OCP), and calcium phosphate salts (Caps) are examples of biodegradable ceramics. Calcium phosphate degradation is influenced by the medium's pH and the material's solubility. It differs for each structure in the following order: HAp $<<$ β-TCP$<$ α-TCP. The degradation degree of calcium phosphates increases when surface area increases, crystal grain size decreases, crystallinity decreases, and grain size decreases. Calcium phosphates have been deployed in medical applications like periodontal treatment, alveolar ridge development, and maxillofacial surgery for nearly 30 years. At human body temperature, only two-member calcium phosphates are stable: dicalcium phosphate DCP at pH less than 4.2 and hydroxyapatite HAp at pH equal to or higher than 4.2. Because of the stoichiometry Ca/P ratio, certain molecules in calcium orthophosphate can be employed in medicinal applications. Calcium phosphates with a Ca/P ratio of less than one cannot be utilized for medical purposes. Due to their acidity, they cause an increase in solubility. Furthermore, the Ca/P ratio has a direct impact on the mechanical properties and solubility rate of calcium phosphate [29, 31, 41, 42].

Hydroxyapatite and Tricalcium phosphate are the two calcium orthophosphates that have the greatest compromises in medicinal applications. The solubility of Hydroxyapatite is equal to that of biological apatites, but when compared to HAp, the solubility of TCP is very fast. That seems to be, HAp has the highest chemical stability in the human aqueous media. Calcium phosphate ceramics have been utilized in bone and dental treatment for nearly two decades since calcium phosphate is the primary mineral component in these organs. Calcium phosphate is used in a variety of hard tissue prostheses, including middle ear surgery, spine surgery, head reconstructive surgery, and filling abnormalities [41, 43, 44]. Calcium phosphate compounds have a variety of behaviors depending on where they are implanted in the living process. For example, hydroxyapatite HAp may take a century to dissolve from an implantation fracture, but CSD (calcium sulfate dihydrate) could disappear entirely in a few weeks. The implantation of biodegradable ceramics in the boney substitutes has three distinguishing characteristics. The solubility of this ceramic in the body is the first characteristic. The use of ceramic to separate it from the body is a second element connected with rapidity. The affinity to change into a new chemical via a dissolution precipitation process is the third characteristic. Sintering temperatures for calcium phosphate ceramics range from 1000 to 1500 degrees Celsius and the material is subsequently compacted to get the desired form. One of the most common applications of calcium phosphate ceramics is in porous structures. As a result of the porous structure, bone development can occur in the pores of the implanted calcium phosphate, which can result in an interface between the implanted ceramic and the bone. Finally, it provides the prosthesis with excellent mechanical stability. The porous structure serves as a scaffold for bone growth [41, 45, 46].

2.1.4 Composites

The composite is made up of two (or more) materials; at least one of them is solid and comes from metal, ceramic, or polymer. In comparison to conventional materials, the goal of the composite material is to get a compound with better stiffness, strength, and toughness, as well as excellent resistance to creep, corrosion, wear, and fatigue. It would also obtain a set of specialized properties including electrical, thermal, and optical with a suitable range of components [47]. Unfortunately, mixed materials are difficult to deal with and are rather costly. The matrix, which is a continuous phase, is armored with a reinforcement (that is a secondary phase), which is also generally the discontinuous phase, in the composite material. Composite materials have grown in popularity over time, and they are now used in a variety of sectors around the world. As a result, various composite biomaterials have been developed and evaluated for a variety of medicinal purposes [48].

2.1.5 Natural Biomaterials

Natural materials primarily consist of natural polymers including collagen and glycosaminoglycans, which are employed in clinical uses. Collagen is a fibrous protein that links and supports various tissues in the body, including skin, bone, tendons, muscles, and cartilage. This is the most abundant protein found in the body of a mammal, such as humans. The most prevalent heteropolysaccharide in the body is a glycosaminoglycan. Glycosaminoglycans are present mostly on cell surfaces or in the extracellular matrix (ECM). These materials demonstrated certain benefits, including their resemblance to macromolecular compounds and easy of detection by the biological environment, as well as their non-toxicity and biodegradability [49].

2.2 Biocompatibility

A biomaterial is a material that could be injected into human tissues without causing any harm. Biocompatibility is a term used to describe biomaterials. It is described as a material's capacity to exist in the human body and its compatibility [20]. Biomaterials should not be mutagenic, allergic, carcinogenic, or toxic. Moreover, toxic substances may cause membrane damage and injury, which may influence the cell's metabolic process. Consequently, cell breakdown and death may occur as a result of these occurrences [50, 51]. As a result, while choosing metallic materials for the implant, corrosion should be considered, as the human body's living system is an exceedingly corrosive medium for metallic materials. Because the human biological system contains a variety of ions, the breakdown of oxygen and hydroxyl during chemical reactions causes the metal to corrode. The substance formed during the corrosion process reacts with live tissue, causing implant failure and putting the patient's health at risk [52]. Additionally, certain biomaterials have a biocompatibility characteristic, whereas others would not. As a result, for some purposes, such as coating, two or more biomaterials will have been utilized simultaneously [53]. Biocompatibility refers to the ability of a biomaterial employed in medicine to be safe and functioning within living tissues. Due to their circumstances and the processes employed to transfer the biomaterial to the recipient, biocompatibility varies from one recipient to another [54]. As a result, any material used in medical applications must first be examined to see if it is biocompatible with the human biological system or not [32].

3. CALCIUM ORTHOPHOSPHATES: BASIC INFORMATION

The chemical similarity of calcium orthophosphates to the mineral component of mammal bones and teeth is the primary motivating factor behind their application as bone replacement materials [57-60]. As a consequence, additionally, by being non-toxic, they are biocompatible, not detected as foreign substances in the host, as well as, most significantly, display both bioactive properties [34] and combine with live tissue through the same mechanisms that are involved in the remodeling of healthy bone. This results in a tight physicochemical connection between the implants and the bones, which is known as osteointegration [61]. More specifically, calcium orthophosphates are osteoconductive (capable of providing a scaffold or template for new bone production) and promote osteoblast adhesion and proliferation [62, 63]. Nonetheless, one of the biggest drawbacks of using calcium orthophosphates as load-bearing bioceramics is their mechanical characteristics, which are brittle and have low fatigue resistance [31, 64, 65]. Because porosity of more than 100 m is considered a necessity for appropriate vascularization and bone cell colonization, the poor mechanical behavior is much more apparent for extremely porous bioceramics and scaffolds [66-68]. Calcium orthophosphates are thus primarily used as fillers and coatings in the biomedical field, making them unsuitable for the healing of major osseous deformities [59, 60].

3.1 Hydroxyapatite: A Basic Introduction

One of the most important components of bioceramics is hydroxyapatite (HAp) [69]. Hydroxyapatites (HAP) are a naturally occurring mineral type of calcium apatite that accounts for approximately 50% of the weight of the bone and has good osteoconductive and osteointegration capabilities [70-72]. As well as tooth enamel has approximately (97 wt%) hydroxyapatites [73]. In addition, many kinds of cancer cells in the body are prevented by HAp molecules [69].

The name "apatite" refers to a group of compounds (not just calcium phosphates) that have a general formula of $M_{10}(XO_4)_6Z_2$, in which M^{2+} is a cation, XO_4^{3-} is an anion, and Z^- is an anion. HAp's molecular chemical formula is $Ca_{10}(PO_4)_6(OH)_2$, wherein M, X, and Z stand for calcium (Ca^{2+}), phosphorus (P^{5+}), and hydroxyl radical (OH^-), correspondingly. As a result, the weights of Ca, P, and OH, respectively, composed 39%, 18.5%, and 3.38% of the total [74].

Carbonate-apatite is a major component of bone minerals, and it is also a major component of hard tissue in some circumstances, such as tooth structure [75]. Because of its bioactivity and osteoconductive qualities in vivo, hydroxyapatite (HAp) is one of the most often used apatites as bioceramic in medicine and dentistry [76-78]. The chemical similarity of HAp to the inorganic material of bone and teeth makes it a better bioceramic or biomaterial than other bioceramics like

Bioglass or A-W glass-ceramic. Hydroxyapatite is a naturally occurring inorganic component present in human hard tissues like teeth and bone. These materials are mainly employed for human body implants. Eggshells, coral, fish bones, chicken bones, and other materials can be used to produce natural hydroxyapatite [79]. Because of its hemostatic property and bone repair function, hydroxyapatite has recently attracted interest [80, 81].

The most significant calcium phosphate in the human body is hydroxyapatite, with a Ca/P composition of 1.67 [82]. HAp has a single phase and hexagonal system unit cell structure, with $a=b\neq c$, $\alpha=\beta=90°$, and $\gamma=60°$. The system corresponds to the P63/m spacing group, with estimated lattice parameters of a=b=0.9418 nm and c=0.6884 nm and volume of unit cell V=0.5288 nm^3. In addition, as illustrated in Figure 3.1, HAp is composed of Ca^{2+}, PO_4^{3-}, and OH^- groups that are arranged in a certain orientation [74].

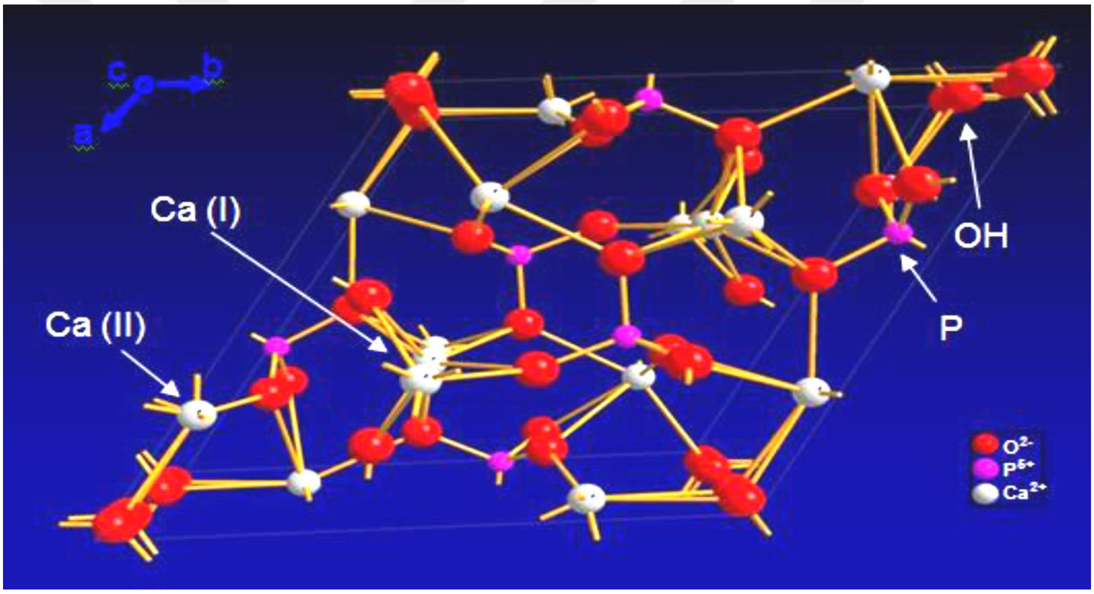

Figure 3.1. Hydroxyapatite $Ca_{10}(PO_4)_6(OH)_2$ molecular structure [74].

Ca (I) and Ca (II) are the two calcium sites of the HAp unit cell, as displayed in Figure 3.1. The first site Ca (I) is surrounded by nine oxygen atoms in the position of four calcium atoms per unit cell inside the parallel column to the c- axis. The other Ca (II) site has six calcium atoms per unit cell and is known as an anion channel [74].

One of the rare earth elements is erbium (Er). The bone has the largest concentration of erbium, whereas the liver has the lowest concentration. It has excellent biocompatibility and can improve hydroxyapatite's biological characteristics. It has been found that Er affects bone repair. Er is non-toxic, bioactive, and biocompatible, making it more attractive for medicinal uses [16, 83].

3.1.1 Synthesis Methods of HAp

Various procedures have been used effectively to prepare purified HAp powders. The two primary methods for producing HAp powders are wet and dry procedures. Precipitation, hydrolysis, sol-gel, hydrothermal, emulsion, and sonochemical processes can all be used to synthesize aqueous solutions of Ca and P ions in wet chemical techniques. There are two types of dry methods: solid-state reactions and mechanochemical procedures. Classical dry techniques offer the advantage of creating highly crystalline HAp from very cheap source materials. The downsides are either the high particle size in solid-state synthesis or the poor phase purity of HAp with in mechanochemical approach. According to the literature on synthesizing HAp, progress in producing HAp utilizing dry techniques, particularly solid-state methods, has been limited in recent years [84]. Chaudhari *et al*. synthesized the HAp using the following reaction [85]:

$$10\ CaO + K_2HPO_4 + 4H_2O \rightarrow Ca_{10}(PO_4)_6(OH)_2 + 12KOH \tag{3.1}$$

Khoo *et al*. extracted natural HAp from bovine femurs using calcination at various temperatures. The composition, crystallinity, and crystallite size of the extracted natural HAp were found to be affected by particle size and calcination temperature [86].

HAp could be synthesized with coral [87], seashells [88], eggs [89-91], and bodily fluids[92]. For the production of hydroxyapatite from eggshells, many procedures have been identified. The hydrothermal process is one of them. The process of producing HAp from eggshells has been widely published [93]. This process of producing HAp from eggshells in a phosphate solution at high temperatures is a significant approach for producing useful biological materials [89]. This approach uses $Ca(OH)_2$ and $CaHPO_4.2H_2O$ for starting ingredients to make fine hydroxyapatite single crystals using a hydrothermal process. The main benefit of the hydrothermal approach is that HAp produced in this way has higher crystallinity and homogeneity. This methodology is simple and provides all of the HAp properties, but it is difficult and time-consuming [89].

The microwave irradiation process, as shown in Figure 3.2, needs a chelating agent, such as ethylenediamine tetraacetic acid (EDTA) [94]. This is an indirect method in which the first step in the synthesis of HAp is the creation of calcium precursor from eggshells. Preparation of HAp improves sinterability and stability at high temperatures, as well as stoichiometry, morphology, and osteoblast cell adhesion [95]. Microwave-assisted biomimetic production, according to Türk et al., could be a potential method for producing HAp powders in less time [96].

HAp is also produced using a high-energy mechanochemical activation technique. Attrition milling and ball milling are the two procedures involved [97]. The starting powders receive enough hydroxyl groups from the mechanochemical process to generate a single phase of hydroxyapatite. This method is straightforward and suggested for the mass production of high-crystalline hydroxyapatite [98].

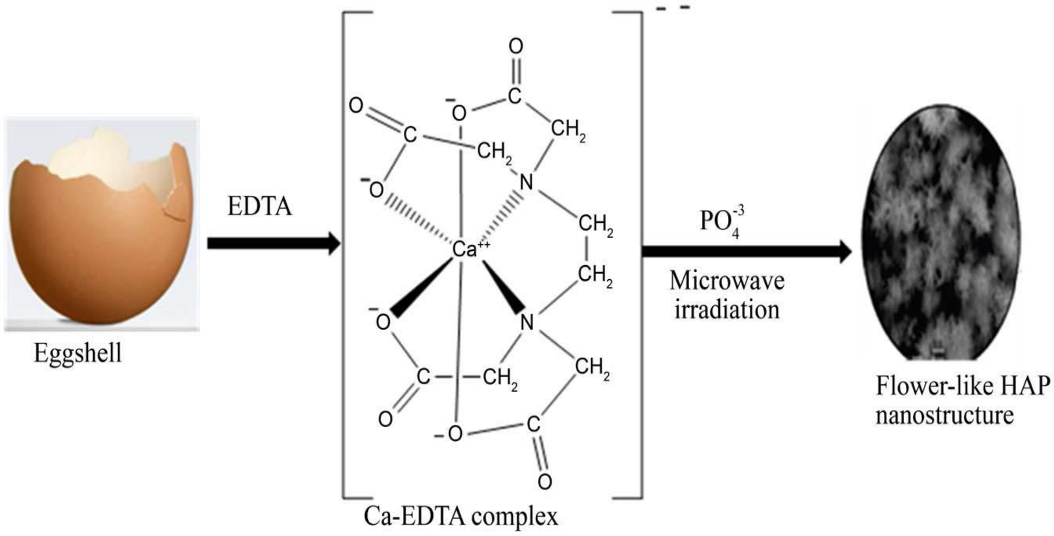

Figure 3.2. Egg shell hydroxyapatite nanostructure prepared by microwave irradiation

Nanohydroxyapatite can be produced from egg shell using a simple sol-gel precipitation process. The powders are polycrystalline and range in size from 5 to 90 nanometers. The nano-Hap synthesized was shown to be pure [99] and have better bioactivity compared to hydroxyapatite coarser crystals [100]. Bernard *et al*. described synthesizing HAp via neutralizing a suspension of lime $Ca(OH)_2$ with an orthophosphoric acid solution at low temperatures. It's a straightforward and non-polluting procedure [101].

$$6H_3PO_4 + 10Ca(OH)_2 \rightarrow Ca_{10}(PO_4)_6(OH)_2 + 18H_2O \quad 3.2)$$

Guo *et al*. used the reverse microemulsion process to produce nano-sized HAp particles with varied hydrophile-lipophile balances (HLB). In comparison to the standard precipitation approach, microemulsion-prepared HAp particles had a lower particle size and a higher degree of particle agglomeration [102].

Biomimetic preparation is fundamentally dependent on biologic systems that process and store specific information at the molecular level [103-105]. In the last few decades, the production of synthetic bone has advanced as a result of the extension of this principle [106]. A biomimetic technique was used to produce hydroxyapatite (HAp)-gelatin (GEL) nano composites [107].

3.1.1.1 Wet Chemical Method

The wet chemical technique is employed to synthesize hydroxyapatite. This process is significantly faster than the conventional process. Due to their high surface area, simplicity, easy availability, relative simplicity of driving, and use of low-cost raw materials, this process is significantly faster than conventional techniques. Wet chemical precipitation is one of the most popular processes, and it can be regarded as one of the most prevalent methods. Wet procedures have been used the most often to synthesize HAp samples with a nano-scale structure and consistent morphology [84]. İnce *et al* used a wet chemical method to produce Ni/Mg co-doped HAps and investigated their structural characteristics. They showed that using a wet chemical process, it is simple to make co-doping nanocrystalline HAp from basic materials. Furthermore, they discovered that the adding of Ni resulted in a significant reduction in crystallite size, lattice parameters, and crystallinity. The transition from the HAp to the β-TCP phase was noted. Because of the difference in ionic radius between Mg and Ca (0.065 nm) and (0.099 nm), correspondingly, phase transformation of HAp to -TCP occurs [108].

3.1.2 Lanthanide-Doped into Hydroxyapatite

Some rare earth elements or lanthanides, including Gd^{3+}, Y^{3+}, Pr^{3+}, La^{3+}, Nd^{3+}, and Ce^{3+}, are being supplemented to HAp to improve its biological characteristics and improve bone regeneration, according to a recent study [124]. The rare earth elements are a group of 17 metals that range from lanthanum to lutetium. Lanthanides are divided into two categories: light and heavy [125]. Because of their unique optical, magnetic, and catalytic properties, these elements can be employed in a variety of nanomedical applications, including treatment, imaging, and diagnostics [126]. In comparison to non-doped composites, HAp synthesized handled with lanthanide showed improved biological features such as biocompatibility, cell adhesion, and proliferation [127].

Among them, Ce^{3+} is inexpensive and has been shown to improve the biological properties (e.g., antibacterial activity, cell viability, and biodegradability) of pure HAp [12, 128-130]. Ce-containing ceramics have been used in medical applications including Alzheimer's disease, dental fillings, drug delivery, catheters, burn wound healing, and cancer therapy due to their exceptional properties [131]. As well as Erbium (Er^{3+}) is found in the human body, with a large concentration in the ribs and a lower amount in the kidneys and liver [132]. Er-doped HAps can be employed in biophotonic applications, according to researchers [133]. Furthermore, due to its light emission spectra and high biocompatibility, a good dopant for the HAp structure has been suggested Er. [17]. Yttrium (Y^{3+}) is one of the lanthanide group elements and is applied to improve the mechanical strength of ceramics [134-136]. Y-doped calcium oxyhydroxyapatite [$Ca_{10-x}Y_x(PO_4)_6(OH)_{2-x}O_x$] has been investigated for use as a humidity sensor due to its greater hydrophilic nature [137]. Furthermore, as compared to pure HAp, Y-doped HAp exhibits higher electrical conductivity [137]. Also, Y-doped HAp is a great candidate for orthopedic implants because it has good electrical conductivity and hydrophilicity [135, 137-140]. Moreover, Y-doped HAp has a high level of stability in a variety of environments [138, 139, 141] and when compared to pure HAp, it enhances osteoblast adhesion [142]. Similarly, praseodymium (Pr) is useful in a variety of industries and medical disciplines due to certain special properties [143]. Praseodymium and other lanthanide ions exhibit biological features that are most similar to the Ca^{2+} ion in terms of ionic radius [144]. Their coordinate range and binding behavior are two further aspects of these similarities that are not restricted to their ionic radii. Additionally, they have a higher charge, a high affinity for the Ca^{2+} sites on biological molecules, and a greater attraction for water molecules [145]. According to recent investigations, the human body contains lanthanide elements, which may be detected in the liver, spleen, lung, and bone [146].

3.1.3 Properties of Hydroxyapatite

Hydroxyapatite is a calcium phosphate with form and composition identical to human hard tissues [147] which has a hexagonal structure [148, 149] and a 1.67 stoichiometric Ca/P ratio, which is the same as bone apatite [148, 150, 151]. As compared to other calcium phosphates, one of the most essential properties of hydroxyapatite has been its stability. Regarding physiological parameters such as temperature, pH, and body fluid composition, hydroxyapatite is the best stable calcium phosphate compound thermodynamically [148].

The advancement of nanotechnology has had a significant influence on materials science. Nanomaterials have got a lot of interest recently for adsorption, catalysis, and optical uses, especially as biomaterials are included [152]. Because of its similarity in size, crystallography, and chemical composition to human hard tissue, nano-hydroxyapatite is receiving interest as a biomaterial used in prosthetic applications. The component of this material is found in bone and tooth enamel.

Furthermore, HAp possesses the following properties: biocompatibility, osteoconductivity, bioactivity, non-toxicity, and non-inflammatory characteristics [152].

3.1.4 Some Applications of Hydroxyapatite

Currently, hydroxyapatite is developing in popularity as a dental and orthopedic implant product [153, 154]. Because of critical biological features including such lack of immuno-reaction as well as the absence of postoperative morphological change or volume decrease, HAp composites are used in clinical orthopedics for spacing or filling bone defects, according to Oonishi. High-density polyethylene wear particles are avoided with HAp implants bonded with cement. HAp is also utilized as a coating on metals for cement less stability and in femoral plugs in hip replacement surgery. Porous metal interfaces are employed for quick and powerful cement less fixing; HAp coating of porous metal enhances outcomes [155].

Improved osteointegration, osteoblast adhesion, and calcium mineral deposition on the interface of scaffolds using HAp polymeric composites promoted new bone tissue growth [156]. To stimulate mineralization in bone repair, HAp-enhanced surface characteristics can be employed to promote cell responsiveness and proliferation. HAp has been employed in a variety of biomedical sectors; including bone cement matrices, controlled medication release, tooth paste additives, and dental implants [157].

Palazzo *et al* revealed that the characteristics of HAp nanocrystals could be modified to create HAp/biomolecule conjugates customized for certain treatment purposes [158]. Nano HAP was used for both bioimaging and medicinal purposes [159].

4. GAUSSIAN09 PROGRAM

Chemists, chemical engineers, biochemists, physicists, as well as other scientists all use the Gaussian software applications. It employs basic quantum mechanics equations to estimate energies, molecular structures, and spectroscopic data such as NMR, IR, UV, and others, as well as much more advanced computations. Gaussian 70 was first produced in 1970 by John Pople with his research team at Carnegie-Mellon University. Gaussian09 is the most recent version in the Gaussian collection of applications, and it has been regularly upgraded since then. Gaussian09 has useful capabilities and improvements that will allow researchers to simulate molecular systems of increasing size more accurately and under a wider range of real-world situations. Some of these characteristics include the ability to simulate reactions of very large systems, analyze excited states in the gas phase and also in solution, forecast more spectra, new and improved methodologies and algorithms, ease-of-use characteristics, and performance enhancements. Gaussian09 provides a number with very reliable energy techniques for estimating thermochemical values, Photochemistry as well as other Excited State Operations, and Solvent Effects for optimizing structures and guessing most molecular features [160].

4.1 Gaussian Methods

The theoretical method is a series of approximations that are used to model a system. These approximations were linked with a computation method and used to atomic orbitals described by the basis set (see section 4.2), to calculate molecular orbitals as well as energy. Semiempirical, ab initio, density functional, and molecular mechanics techniques are the four primary types of methods. The choice of a theoretical model is determined by the size of the system and the level of approximation [161].

4.1.1 Ab Initio Method

This kind of computing is dependent only on theoretical ideas and does not make use of any experimental results. The various methods share the same fundamental idea but are different in the mathematical assumptions they employ. Despite the truth that the computations are extremely time-consuming, they are the most common types of models. The essential ab initio concept is the Hartree Fock (HF) [161].

The Hartree–Fock (HF) technique is an approximation approach for determining the wave function and energy of a quantum many-body system in a stationary state within computational physics and chemistry. The Hartree–Fock technique is also known as the self-consistent field approach (SCF) in earlier publications. Hartree needed the final field calculated from the charge distribution to be "self-consistent" with the expected initial field when deriving what is now known as the Hartree equation as an approximate solution to the Schrödinger equation. As a consequence, self-consistency is a condition for the method [162].

The Hartree–Fock technique is most commonly used to solve the Schrödinger equation for atoms, molecules, nanostructures, and solids, but it has additionally been widely used in nuclear physics. Because calculations in atomic structure theory could involve a spectrum with multiple excited energy levels, the Hartree–Fock approach for atoms implies that the wave function is a single configuration state function including quantum numbers and that the energy level would be not always the ground state [163].

4.1.2 Semiempirical Method

Throughout the calculation, semiempirical approaches employ a set number of empirical data. For illustration bond lengths of a certain kind, have a constant value regardless of the system (For instance, a C=C bond, would always be considered equal to 134 pm). This significantly reduces processing time but it is not quite reliable. Semiempirical techniques are typically applied for very large systems since they can manage massive quantities of calculation.

4.1.3 Density Functional Theory (DFT)

DFT methods have become increasingly popular since the results achieved are equivalent to those obtained with ab initio techniques while requiring significantly less central processing unit (CPU) time. DFT differs from approaches that are relying on HF computations in that the electron density, rather than a wave function, is employed to calculate the energy. B3LYP (the most prevalent DFT model), PW91 Gradient-corrected technique, and VWN are examples of DFT methods [161].

The electronic structure of atoms, molecules, and solids is calculated using density functional theory (DFT), a quantum-mechanical (QM) approach employed in chemistry and physics. Since the 1970s, it has proven particularly popular in computational solid-state physics. But, it has been not till the 1990s that advancements to the approach found it acceptable for quantum-chemical deployments, leading to a surge of application areas. When compared to electron-correlated wave function-based approaches which include Miller–Plesset perturbation theory or coupled cluster, DFT's actual strength is its favorable price/performance ratio. As a result, bigger (and usually very significant) molecular systems could be investigated with adequate precision, extending the predictive potential inherent within the electronic structure concept. As a consequence, DFT is currently perhaps the most extensively utilized approach for determining electronic structure. The

Nobel Prize in physics and chemistry was awarded to Walter Kohn in 1998 for his discovery of density-functional theory [164].

Most electronic structure computations use the Born–Oppenheimer approximation. By considering that the electronic and nuclear movements could be separated, it considerably simplifies the Schrödinger equation. Although this hypothesis is true in the majority of circumstances, adjustments beyond the adiabatic (Born–Oppenheimer) level are occasionally necessary. Eberhard Gross and Nikitas Gidopoulas investigated DFT over the Born–Oppenheimer assumption and introduced a non-adiabatic solution for the electronic equation in a novel context that self-consistently connects the electronic and nuclear wave functions [165].

The creation of new and more precise density functionals is a developing topic of study. It is noted that certain functionals are considerably better suited to specific applications than others, although attempts are being made to build more general-purpose functionals. Truhlar's group at the University of Minnesota is one of the groups working on functionals with broad applicability. New functionalities, of usual, must be checked for application and correctness. The most popular method for this is to compare the results generated by these functionals to match the most accurate study results. The Minnesota group determined that DFT accuracy has improved significantly over the previous few decades; however, there are still certain issues, such as multi-reference systems [166].

4.1.4 Molecular Mechanics (MM)

Atoms are modeled as spheres, whereas bonds are modeled as springs in MM approaches. An algebraic equation, rather than a wave function or electron density, would be employed to calculate the energy in this method. The constants in the formula are extracted through experimental results or other computations and kept in a data library. These computations are very basic and we don't need to use complex programs like G09. We may perform our computation directly in Avogadro [161].

4.2 Basis Sets

The basis set is simply the limited collection of atomic-like functions in that the molecular orbital is produced by the linear combination of atomic orbitals (LCAO). The basis set can be Slater-type orbitals (STOs) [167] or Gaussian-type orbitals (GTOs) [168]. In chemistry, wave functions are known as "atomic orbitals" or "molecular orbitals." They are also known as "stationary states" or "energy eigenstates." As a result, molecular modeling depends on them [169, 170].

AOs (atomic orbitals) were described using Slater-Type Orbitals (STOs) and Gaussian-Type Orbitals (GTOs). GTOs have a benefit over STOs in that they are significantly easier to calculate while STOs characterize the shape of AOs more precisely than GTOs. Computing many GTOs and merging them to define an orbital is faster compared with computing an STO. As a result, configurations of GTOs are commonly employed to define STOs, which in turn characterize AOs.

The Gaussian Program's most basic and typical base is Slater-Type-Orbitals, which are simulated using 3 Gaussian functions apiece (STO-3G). In general, when n is smaller than three, the computations provide unsatisfactory results, STO-3G is referred to as the minimum basis set. For very small molecules or atoms, minimum basis sets can be used [171]. On a function-to-function comparison, STOs provide precise solutions for hydrogenlike atoms and outperform Gaussian functions for multi-electron situations.

The 3-21G basis set is the most widely utilized for geometry optimization [172, 173]. For the core orbitals, this technique employs three Gaussians and a two-to-one split for the valence functions. To enhance a basis set, d orbitals for all heavy (non-hydrogen) atoms are usually added. The d orbitals are included in the polarization basis sets, which are denoted by the sign "*". The 6-31G** basis set is a further evolution, whereby each hydrogen in the 6-31G* basis set is given a set of p orbitals [174].

To represent the wave function, John A. Pople advanced the construction of ab initio approaches employing Slater-type basis sets or Gaussian orbitals. He developed models by combining methodologies and basis sets, and then compared the experimental findings of the study [174]. Atomic orbitals of the Gaussian type have been widely utilized to determine atomic and molecule wave functions. They were engaged in the development of the Gaussian programs, which are now one of the most widely used computational chemistry packages [175].

The exchange functional and correlation functions are used in fundamental density functional theory (DFT) techniques. The functionals BP86, B3LYP, and BPW91 are used in the majority of recent DFT investigations. The method and the basis set together identify the chemical model as Gaussian, indicating a degree of theory. If no additional keywords are specified, the HF method will assume to be the default. Most methods additionally need a basis set; if no basis set keyword is given, STO-3G is used automatically. STO-3G, 3-21G, 6-21G, and 6-31G are some instances of basis sets. The standard * or ** sign can also be used to obtain single first-polarization functions. 6-31G*, also referred to as 6-31G(d), is 6-31G with extra d polarization functions on non-hydrogen atoms, whereas 6-31G**, also defined as 6-31G(d, p), is 6-31G* with p polarization functions on hydrogen atoms [176]. Some basis sets provide the + and ++ diffuse functions. 6-31+G consists of 6-31G plus diffuse s and p characteristics for non-hydrogen atoms, whereas 6-31++G includes diffuse functions for hydrogen atoms. cc (correlations-consistent basis) and pV (polarized valence basis) were presented by Thom Dunning as optimized basis sets with correlated wave functions [177]. The presence of a large basis set does not usually imply that the model will correlate with the experimental results [178, 179].

It's hard to identify the best methodology for scientific computations because there are so many different basis sets and optimization approaches. The basis set used in chemical computations could have a significant effect on the accuracy of the findings, especially when using correlated ab initio approaches [180]. The selection might be informed by knowledge of the newest advancements in the field's design, development, and optimization. Basis sets, for instance, have been used in the simulation and optimization of ultrasonic non-destructive testing. They play a critical role in structural materials including fiber composites and columnar-grained stainless steels [181].

4.3 Energy Band Gap

The energy difference between the top of the valence band and the bottom of the conduction band is referred to as the "band gap." Figure 4.1 depicted the energy band gap, which allows electrons to move from one band to another. The band gap energy is the minimal amount of energy required for an electron to jump from a valence band to a conduction band [182].

HOMO and LUMO are molecular orbitals in chemistry. The abbreviations represent the highest occupied molecular orbital and the lowest unoccupied molecular orbital, accordingly [183]. The HOMO–LUMO gap refers to the energy differential between HOMO and LUMO. HOMO and LUMO can also refer to as the frontier orbitals. The valence band is the HOMO level, while the conduction band is the LUMO level. The difference in HOMO and LUMO energies can be used to compute the energy band gap [184].

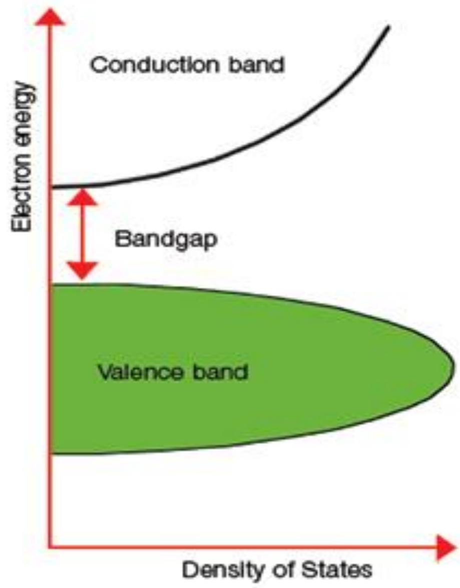

Figure 4.1. Illustration of energy band gap [185]

4.4 Uses of Gaussian 09 Software

Gaussian software, which is widely used in chemistry, chemical engineering, biochemistry, physical chemistry, and other chemistry-related fields, is currently the most frequently used international quantum chemistry calculation program. Molecular energy and structure, transition state energy and structure, chemical bond and reaction energy, molecular orbital, dipole moment, and multipole moment, atomic charge and potential, infrared and Raman spectroscopy, NMR, polarizability, and superiority can all be studied using Gaussian software. Chemical conversion rate, thermodynamic characteristics, potential energy surface scanning, reaction path, and other topics are being researched by using Gaussian programs. It can simulate the ground state or excited state, as well as the gas phase or solution system. Currently, the maximum is 09 Gaussian. GaussView is a Gaussian-supporting program that was created specifically for this purpose. It is a graphical user interface that corresponds to it. It is primarily used to observe molecules, set and submit Gaussian calculation assignments, and display the results of Gaussian calculations. It helps researchers in understanding the microscopic world on an atomic and molecular level, as well as improve abstraction and spatial imagination [186].

4.5 Corrosion Inhibiting

Metals are protected against corrosion by corrosion inhibitors. Inhibitors are chemicals in a corrosive medium that delay or stop metal corrosion [187-191]. Corrosion processes are responsible for a large number of deaths, particularly in the manufacturing industry. The only way to deal with it is to discourage it, as is evident. Corrosion inhibitors are one of the most well-known and successful strategies in the industry for avoiding or reducing metal surface damage or oxidation [192-194].

Because of their outstanding anti-corrosive properties, inhibitors have long been utilized in industry. However, many of them came as a result of side effects, resulting in environmental damage. Therefore, scientists began to search for ecologically acceptable compounds, such as organic inhibitors [195-202]. As a result, organic coatings have long been recognized as a low-cost technique for preventing metal corrosion [203]. The majority of organic inhibitors work by adsorbing onto metal surfaces [204]. Organic inhibitor molecules can adsorb onto corroding metals either physically or chemically [205].

The performance of the inhibitor can be investigated experimentally and/or theoretically by computational chemistry. Weight loss, linear polarization, potentiodynamic polarization, electrochemical impedance spectroscopy (EIS), UV visible spectroscopy, scanning electron microscope (SEM), X-ray spectroscopy (EDX) [206], and cyclic voltammetry [207] are commonly used to perform observations of corrosion inhibition efficiency and to check the inhibition mechanism. On the other hand, depending only on experimental approaches is costly, time-consuming, and hazardous to the environment [208]. For this reason, many researchers have been working in computational chemistry [187, 209-212].

Quantum chemical calculations are used to identify the structural characteristics of organic corrosion inhibitors that are associated with corrosion inhibition properties [209]. Density functional theory (DFT) is a quantum chemistry approach for measuring the electronic properties of molecules [213, 214] and analyzing inhibitor/surface connections in corrosion inhibition research. Different electronic characteristics derived from quantum chemistry techniques are employed for calculations of corrosion inhibition capabilities as well as to support experimental measurements [215-217].

5. MATERIAL AND METHODS

The experimental technique is outlined in detail in this section. The characterization technique is then explained, along with the instruments and experimental conditions that were employed.

5.1 Synthesis and characterization

Three groups of Er-based HAp samples with a constant amount of Er (0.39 at.%) co-doped with Ce or Pr or Y at various amounts of (0.13, 0.26, 0.39, 0.52, 0.65 and 0.78 at.%) were successfully prepared using wet chemical synthesis. For each synthesis, distilled water was used as a solvent for the as-used chemicals of calcium nitrate tetrahydrate ($Ca(NO_3)_2{\cdot}4H_2O$, Carlo-Erba), erbium nitrate pentahydrate ($Er(NO_3)_3{\cdot}5H_2O$, Sigma-Aldrich), cerium (III) nitrate hexahydrate ($Ce(NO_3)_3{\cdot}6H_2O$ Sigma-Aldrich), praseodymium (III) nitrate hexahydrate ($Pr(NO_3)_3{\cdot}6H_2O$, Alfa-Aesar), yttrium (III) nitrate hexahydrate ($Y(NO_3)_3{\cdot}6H_2O$, Sigma–Aldrich) and di-ammonium hydrogen phosphate ($(NH_4)_2HPO_4$). A flask was used to prepare a 100 mL solution of either $Ca(NO_3)_2{\bullet}4H_2O$, $Ce(NO_3)_3{\bullet}6H_2O$, $Pr(NO_3)_3{\bullet}6H_2O$, or $Y(NO_3)_3{\bullet}6H_2O$, which was then transferred to a beaker. A separate 100 mL solution of $(NH_4)2HPO_4$ was prepared and added slowly, drop by drop, to the first solution, resulting in the formation of a cloudy solution. The quantities of the mentioned chemicals and the names of each sample are provided in Table 5.1, Table 5.2, and Table 5.3. The pH of this solution was adjusted to 10.0 by adding an ammonia solution (Sigma-Aldrich), followed by mixing the final solution at 65 ºC for 75 minutes. The resulting mixture was then dried in an oven at 120 ºC for 22 hours to obtain dry powders. These powders were subsequently calcined in an electric furnace at 900 ºC for 2.5 hours.

To obtain XRD data, a Rigaku Rad B-DMAX II diffractometer was utilized with Cu-K radiation at a wavelength of 0.15406 nm. FTIR data in the wavenumber range of 400 cm-1 to 4000 cm-1 were obtained using a PerkinElmer Spectrum and the KBr method. Raman spectra were acquired using Renishaw's inVia confocal microscope and a 532 nm diode laser. The morphology of the samples was studied using a Leo Evo-40xVP scanning electron microscope (SEM). DTA (differential thermal analysis) and TGA (thermogravimetric analysis) were performed using Shimadzu DTA 50 and TGA 50 instruments, respectively, from room temperature to 900 °C, with a heating rate of 10 °C per minute.

Table 5.1. The moles of the as-used chemicals in the synthesis for Ce/Er co-doped HAp samples

Sample	$Ca(NO_3)_2 \cdot 4H_2O$ (mmol)	$Er(NO_3)_3 \cdot 5H_2O$ (mmol)	$Ce(NO_3)_3 \cdot 6H_2O$ (mmol)	$(NH_4)_2HPO_4$ (mmol)
0.13Ce-0.39Er-HAp	49.740	0.195	0.065	30.000
0.26Ce-0.39Er-HAp	49.675		0.130	
0.39Ce-0.39Er-HAp	49.610		0.195	
0.52Ce-0.39Er-HAp	49.545		0.260	
0.65Ce-0.39Er-HAp	49.480		0.325	
0.78Ce-0.39Er-HAp	49.415		0.390	

Table 5.2. The moles of the as-used chemicals in the synthesis for Pr/Er co-doped HAp samples

Sample	$Ca(NO_3)_2 \cdot 4H_2O$ (mmol)	$Er(NO_3)_3 \cdot 5H_2O$ (mmol)	$Pr(NO_3)_3 \cdot 6H_2O$ (mmol)	$(NH_4)_2HPO_4$ (mmol)
0.13Pr-0.39Er-HAp	49.740	0.195	0.065	30.000
0.26Pr-0.39Er-HAp	49.675		0.130	
0.39Pr-0.39Er-HAp	49.610		0.195	
0.52Pr-0.39Er-HAp	49.545		0.260	
0.65Pr-0.39Er-HAp	49.480		0.325	
0.78Pr-0.39Er-HAp	49.415		0.390	

Table 5.3. The moles of the as-used chemicals in the synthesis for Y/Er co-doped HAp samples

Sample	$Ca(NO_3)_2 \cdot 4H_2O$ (mmol)	$Er(NO_3)_3 \cdot 5H_2O$ (mmol)	$Y(NO_3)_3 \cdot 6H_2O$ (mmol)	$(NH_4)_2HPO_4$ (mmol)
0.13Y-0.39Er-HAp	49.740	0.195	0.065	30.000
0.26Y-0.39Er-HAp	49.675		0.130	
0.39Y-0.39Er-HAp	49.610		0.195	
0.52Y-0.39Er-HAp	49.545		0.260	
0.65Y-0.39Er-HAp	49.480		0.325	
0.78Y-0.39Er-HAp	49.415		0.390	

5.2 *In vitro* biocompatibility assay of Y, Ce, Pr /Er-HAp samples

The ceramic powders were individually weighed at a mass of 0.1 g each and placed in sterile tubes with a capacity of 2 mL under sterile conditions. Following that, 1 mL of DMEM (Dulbecco's Modified Eagle Medium) was added to the materials, and they were placed in an incubator for 72 hours. L929 cells (Mouse Fibroblast) were cultured in a flask at 37 degrees Celsius with 5% CO2 using high glucose DMEM medium, which consists of 10% FBS and 1% Penicillin-Streptomycin. The 96-well plate was filled with 10,000 L929 cells, allowing them to adhere and spread in the CO2 incubator overnight. After 24 hours, the medium in the well plate was removed and discarded, and instead, the wells were filled with filtered media that had been in contact with the compounds for 72 hours.

The cells were then cultured in the medium containing the materials for 24 hours in the incubator. MTT dye was diluted in PBS (phosphate buffer, pH 7.4) to a concentration of 5 mg/mL. After 24 hours, the soaking medium in the well plate was removed and discarded. Instead, each well was filled with 90 liters of DMEM. MTT (3-(4,5-dimethylthiazol-2-yl)-2,5-diphenyltetrazolium bromide) was added, and the plate was incubated. After incubation, the medium containing MTT in the well plate was removed and discarded. Each well was then treated with 100 mL of DMSO. The well plates were immediately evaluated at a wavelength of 540 nm after the addition of DMSO.

5.3 Computational Methodology

Chem. Bio Draw Ultra 14.0 was used to draw the structure of the molecules (Benzene (C1), Phenol (C2), Toluene (C3), Benzoic acid (C4), Acetophenone (C5), Chlorobenzene (C6), Bromobenzene (C7), Benzaldehyde (C8), Naphthalene (C9), and Anthracene (C10)) (Figure 5.1). All computations were performed using the Gaussian 09 packages. With Gaussian 09 program allows users to do many computations [218-224]. The ten molecules firs have been optimized. The DFT method is used to precisely determine the electronic characteristics of the structures by taking into consideration the electron density and producing the appropriate data over this electron density. B3LYP is well-liked for a variety of reasons. It was one of the first DFT approaches to outperform Hartree-Fock. B3LYP is often quicker than most Post-Hartree-FockHartree-Fock methods, and the results are usually similar. For a DFT approach, it is also rather robust. It is not as highly specified as other hybrid functionals on a more basic level [225]. Furthermore, the Gaussian 09W software's hybrid function B3LYP, which is compatible with the workstation's capability, and 6-31G (d,p) [226] as the basis set were employed.

The total energy, the energy of the maximum occupied molecular orbital (E_{HOMO}), the energy of the lowest unoccupied molecular orbital (E_{LUMO}), energy difference ΔE, dipole moment (μ), ionization energy, electron affinity, chemical hardness (η), softness (σ), nucleophilicity (ε) index, electrophilicity (ω) index, chemical potential (Pi), and electronegativity (χ) have all been calculated. The transmitted electron fraction (ΔN) between the copper surface and the molecules has been computed.

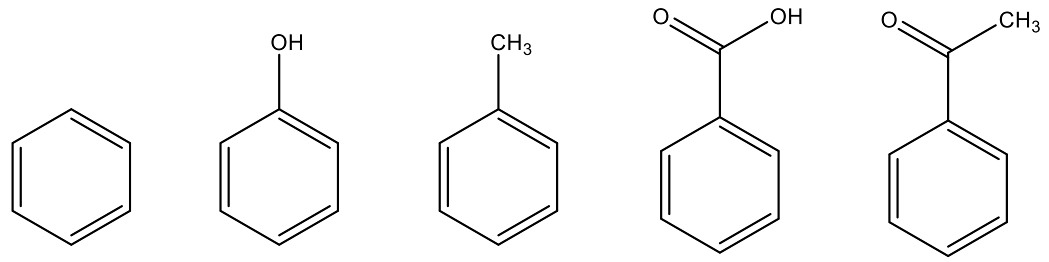

C1 C2 C3 C4 C5

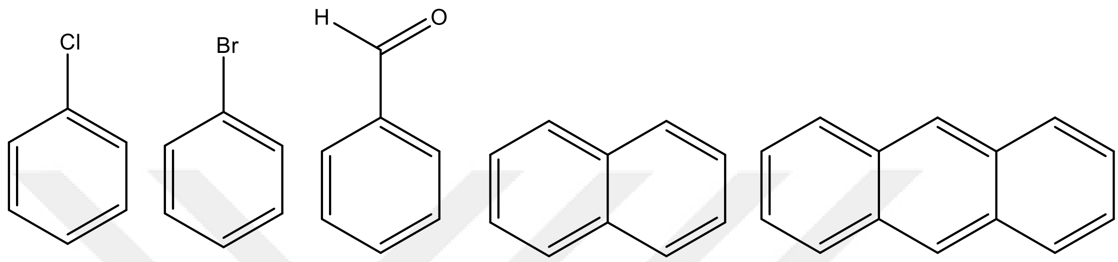

C6 C7 C8 C9 C10

Figure 5.1. The structure of the molecules by Chem. Bio Draw Ultra 14.0

6. RESULTS AND DISCUSSION

6.1 Effects of Yttrium Doping on Erbium-Based Hydroxyapatites

6.1.1 Experimental Results of Er/Y co-doped HAps

Using the aforementioned approaches, the produced samples were comprehensively characterized for the investigation of morphological, structural, thermal stability, and biocompatibility. The following is a description of the measurements, analysis, and discussion of the results.

6.1.1.1 XRD Analysis of Er/Y co-doped HAps

The XRD data of the produced samples are shown in Figure 6.1. The samples' examined data were compared to the standard for pure HAp (JCPDS no: 09-0432). The XRD plots showed that for all of the samples, HAp only behaved as a single phase without the development of any potential secondary phases. Er_2O_3 and/or Y_2O_3-related phases are not found, most likely as a result of the low overall REE (Rare Earth Elements) content (1.17at.%). Additionally, the samples' XRD data following the addition of Y showed minor changes in intensity. Peak intensity varies as a result of ionic doping's effects on the material's structure, as has already been seen and described [227]. The crystallite sizes (D_S) were determined using the Scherrer relation found in Equation (6.1) [228].

$$D_S = \frac{0.9\lambda}{\beta \cos\theta} \tag{6.1}$$

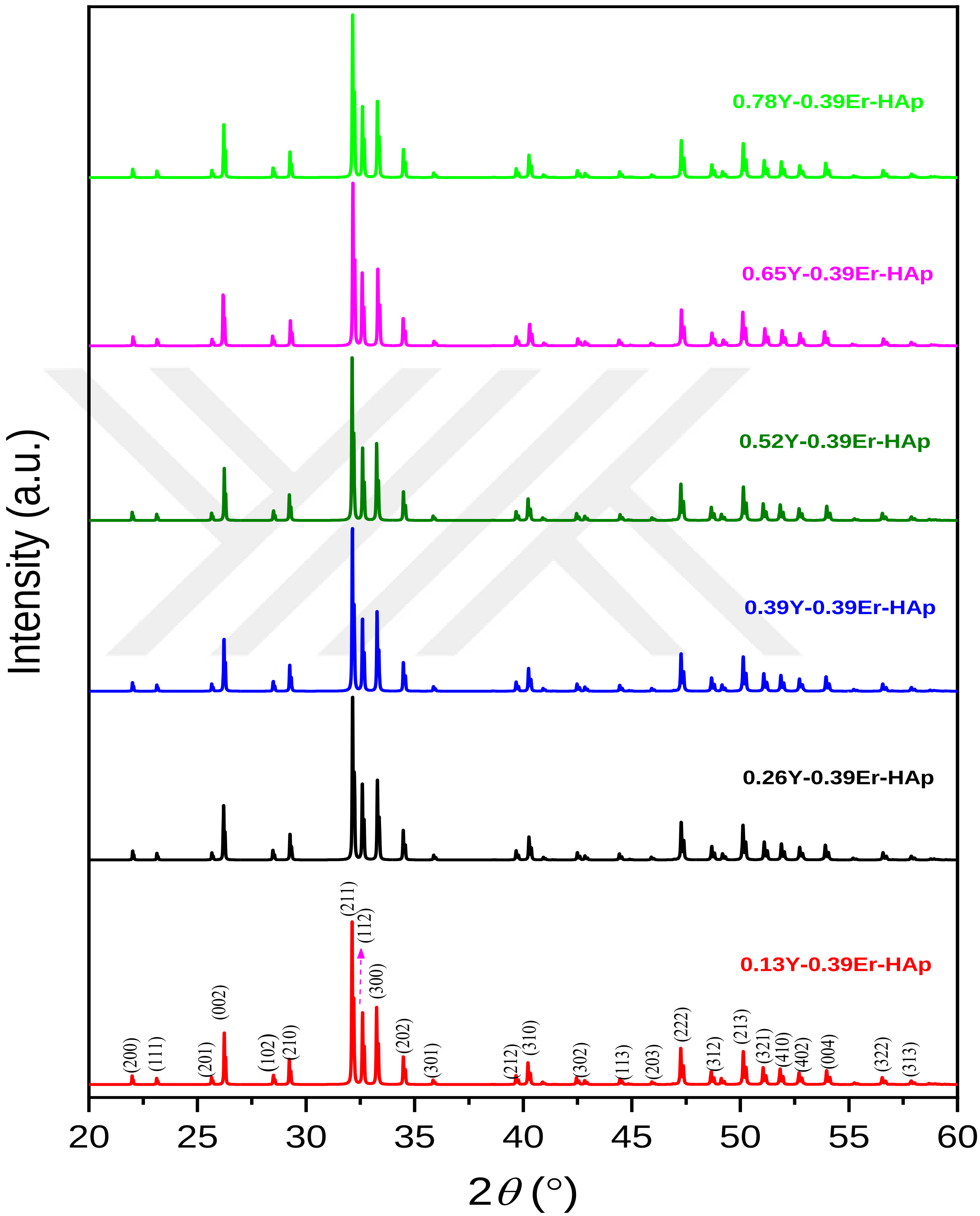

Figure 6.1. XRD patterns of the Er-based HAp samples doped with Y at various amounts

Additionally, the Williamson-Hall (D_{WH}) plot was utilized to assess strain using Equation (6.2) [229].

$$\beta \cos\theta = \frac{0.9\lambda}{D_{WH}} + 4\varepsilon \sin\theta \tag{6.2}$$

where β refers to the full width at half maximum, λ is the incoming X-ray source wavelength, θ is the diffraction angle, and ε is a lattice strain. The comparison values of the βcosθ versus 4sinθ for all synthesized samples are shown in Figure 6.2a. The D_{WH} and ε values can be expressed by using the relationship ε=σ/E, where E and σ denote Young's modulus and stress, respectively [230].

$$\beta \cos\theta = \frac{0.9\lambda}{D_{WH}} + \frac{4\sigma \sin\theta}{E} \tag{6.3}$$

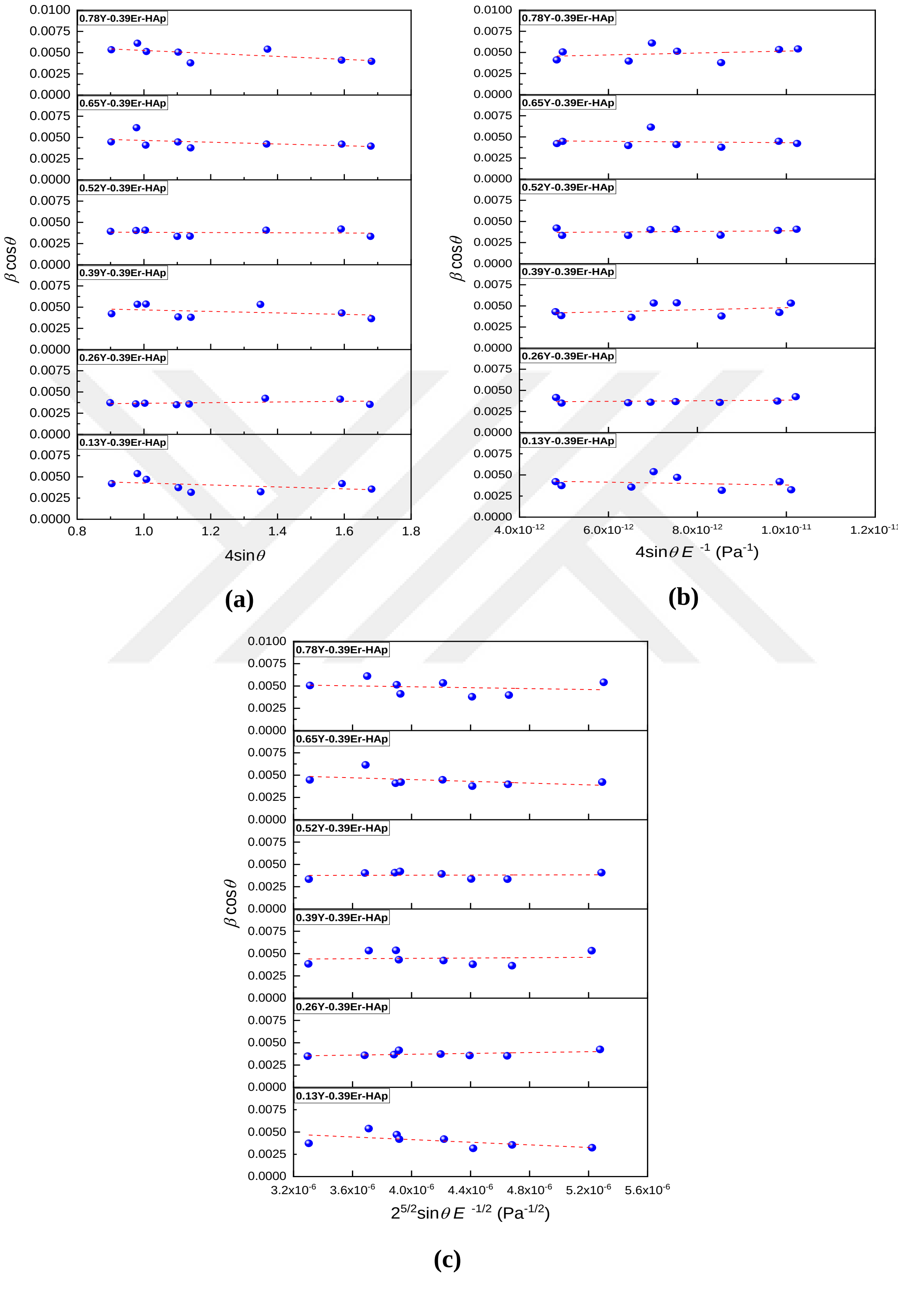
0.78Y-0.39Er-HAp
0.65Y-0.39Er-HAp
0.52Y-0.39Er-HAp
0.39Y-0.39Er-HAp
0.26Y-0.39Er-HAp
0.13Y-0.39Er-HAp
β cosθ
4sinθ
4sinθ E -1 (Pa-1)
25/2sinθ E -1/2 (Pa-1/2)

(a) (b)

(c)

Figure 6.2. (a) The *βcosθ* vs. *4 sinθ*, **(b)** *βcosθ* vs. *4 sinθ* E^{-1}, and **(c)** *βcosθ* vs. $2^{5/2}$ *sinθ* $E^{-1/2}$ plots of the Er-based HAps doped with Y

The slope of the *βcosθ* versus *4sinθ* E^{-1} in Figure 6.2b could be used to get the σ values for all samples. Using the following relation, the E values were calculated [231]. The h,k, and l are miller indices.

$$E = \frac{\left[h^2 + \frac{(h+2k)^2}{3} + \left(\frac{al}{c}\right)^2\right]^2}{7.49\times10^{-12}\left(h^2 + \frac{(h+2k)^2}{3}\right)^2 + 10.9\times10^{-12}\left(\frac{al}{c}\right)^4 - 7.1\times10^{-12}\left(h^2 + \frac{(h+2k)^2}{3}\right)\left(\frac{al}{c}\right)^2} \tag{6.4}$$

Equation (6.2) can be modified by substituting $(2u/E)^{1/2}$ for ε to obtain the anisotropic energy density (*u*),

$$\beta\cos\theta = \frac{0.9\lambda}{D_{WH}} + 4\sin\theta\left(\frac{2u}{E}\right)^{1/2} \tag{6.5}$$

The *u* values can obtain from the slope of the *βcosθ* versus $2^{5/2}$ *sinθ* $E^{-1/2}$ in Figure 6.2c. The *a, c,* and *V* (unit cell volume) values are [232].

$$\frac{1}{d^2} = \frac{4}{3}\left(\frac{h^2 + hk + k^2}{a^2}\right) + \frac{l^2}{c^2} \tag{6.6}$$

$$V = 0.866a^2c \tag{6.7}$$

where *d* is the inter-planar distance. The crystallinity percentage (X_C%) was computed using Equation (6.8) via the intensity of the pit ($V_{112/300}$) between (*112*) and (*300*) reflections and the intensity (I_{300}) of (*300*) reflection [233].

$$X_C\% = \left(1 - \frac{V_{112/300}}{I_{300}}\right)\times100 \tag{6.8}$$

Table 6.1 is a list of the theoretical and experimental parameters for *a*, *c*, and *V*. These findings show that the presence of the Y atom has an impact on these characteristics. Table 6.2 lists the experimentally established values for anisotropic energy density (*u*), crystallite sizes (D_S and D_{WH}), lattice strain (*ε*), stress (*σ*), and percent crystallinity (*Xc%*). Adding Y seems to alter the crystallinity, as evidenced by the samples' values of *Xc%*, which ranged from 87.4 to 83.7%. Given that Y^{3+} has a large ionic radius (0.1011 nm) [234], Ca2+, which has an ionic radius of 0.099 nm [228], is anticipated to be replaced by Er3+, which has a lower ionic radius (0.088 nm) [235], probable that the crystallite size will change. The evolution of lattice strain could be connected to the observed variations in crystallite size [236]. In addition, the distribution of ions Y^{3+}, Er^{3+}, and Ca^{2+} in the lattice exhibits a charge imbalance. The distribution of Ca in the matrix has been changed by the placement of Y and Er atoms to the host sites, which influenced the crystallite size. The doping appeared to change D_S and D_{WH} values which pointed to causing negative and positive lattice strain ε in the samples. The unit cell is under compressive stress for negative lattice strain, whereas it exhibits tensile stress in case of positive lattice strain [237]. The doping caused changes in stress (σ) and anisotropic energy density (u). Due to their proportionality with strain, tensile and compressive stresses give positive and negative values. Except for the 0.39Y-0.39Er-HAp and 0.52Y-0.39Er-HAp samples, whose u values are less than the published value of 12 kJ m^{-3}, the entire samples exhibited higher u values in comparison to this published value [238].

Table 6.1. Lattice parameter and unit cell volume: theoretical and experimental values of the HAps doped with Y

	Theoretical			***Experimental***		
Samples	***a* (nm)**	***c* (nm)**	***V* (nm)^3**	***a* (nm)**	***c* (nm)**	***V* (nm)^3**
0.13Y-0.39Er-HAp	0.93269	0.67899	0.51151	0.94069	0.68215	0.52275
0.26Y-0.39Er-HAp	0.93165	0.67970	0.51091	0.94029	0.68632	0.52549
0.39Y-0.39Er-HAp	0.93208	0.67932	0.51109	0.94131	0.68234	0.52358
0.52Y-0.39Er-HAp	0.93261	0.67893	0.51138	0.93852	0.68569	0.52304
0.65Y-0.39Er-HAp	0.93108	0.68013	0.51060	0.93727	0.68499	0.52111
0.78Y-0.39Er-HAp	0.93166	0.67947	0.51074	0.93663	0.68414	0.51976

Table 6.2. Calculation parameters of the HAps doped with Y.

Samples	**X_C%**	**D_S (nm)**	**D_{WH} (nm)**	**$\varepsilon\times10^{-4}$**	**σ (MPa)**	**u (kJ m^{-3})**
0.13Y-0.39Er-HAp	87.40	35.55	25.58	-11.500	-84.653	542.219
0.26Y-0.39Er-HAp	83.66	37.20	42.40	3.904	35.514	57.124
0.39Ce-0.39Er-HAp	86.40	31.71	24.98	-8.790	120.487	9.391
0.52Y-0.39Er-HAp	87.29	36.67	35.01	-1.370	35.238	1.162
0.65Y-0.39Er-HAp	86.90	32.01	24.32	-10.500	-40.061	247.890
0.78Y-0.39Er-HAp	84.34	29.25	19.78	-17.500	114.546	66.597

6.1.1.2 FTIR and Raman Spectroscopy Results of Er/Y co-doped HAps

Figure 6.3 displays the FTIR spectra of all the samples, which reveal the presence of phosphate and hydroxyl bands. The bands in wavenumber regions of 471 cm^{-1} (symmetric bending, υ_2), 563 cm^{-1} (asymmetric bending, υ_4), 597 cm^{-1} (asymmetric bending, υ_4), 961 cm^{-1} (symmetric stretching, υ_1), and 1020 cm^{-1} (asymmetric stretching, υ_3) were found to have the phosphate group's vibration modes [239, 240]. The bands at 631 cm^{-1} and 3570 cm^{-1} are connected to the hydroxyl group's vibrational mode [241, 242]. All of the bands that were found in the FTIR spectra for each sample supported the existence of the HAp structure [243].

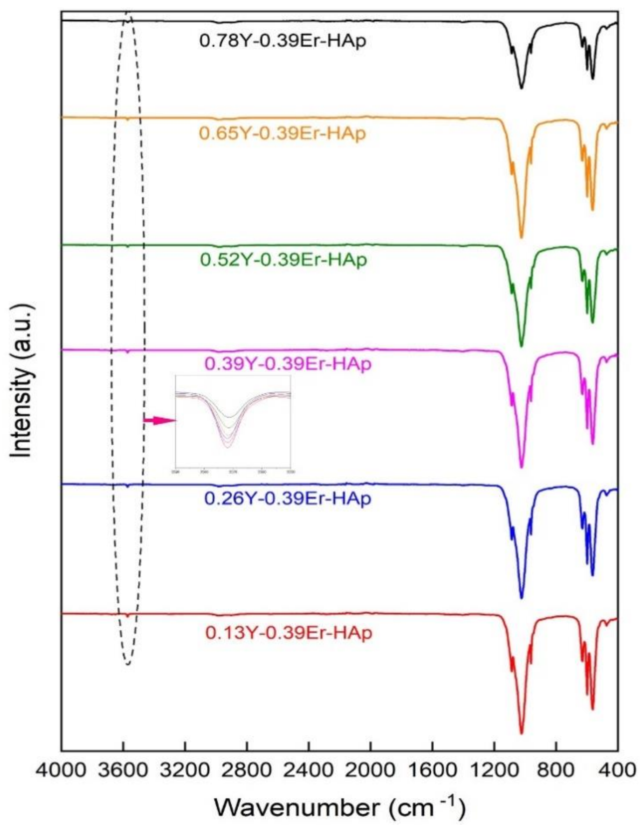

Figure 6.3. FTIR results of the HAps doped with Y

Figure 6.4 displays the Raman spectra of the compounds. At 426 cm^{-1} and 585 cm^{-1}, respectively, the phosphate group's symmetric and asymmetric O-P-O bending modes were observed. At 965 cm^{-1} and 1086 cm^{-1}, respectively, the symmetric and asymmetric P-O stretching modes were found. The band associated with the stretching mode of the hydroxyl group was seen at 3590 cm^{-1}.

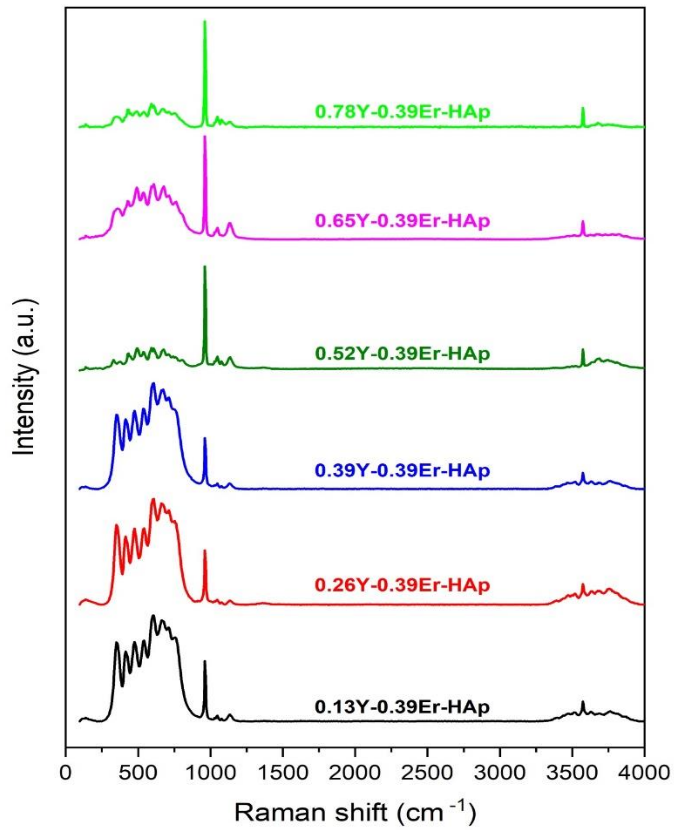

Figure 6.4. Raman spectrum of the HAps doped with Y

6.1.1.3 Morphological Analysis of Er/Y co-doped HAps

Figure 6.5 shows scanning electron microscope (SEM) images and energy-dispersive X-ray (EDX) spectra of as-produced co-doped HAps. The analysis of the morphology of the samples pointed to the presence of sphere-shaped nanoparticles stacked one on top of the other. The findings from the EDX analysis provide evidence in favor of incorporating both co-dopants within the structure of HAp. Additionally, the influence of these co-dopants is limited in the HAp structure, and this may be due to the deposition of these dopants on the sample surface. Table 6.3 gives a detailed comparison between experimental and theoretical values of the stoichiometric ratios of Ca/P and (Ca+Er+Y)/P. Both sets of outcomes closely correspond with each other. The disparities between the theoretical and experimental values for all samples, at both molar ratios, are below 1%.

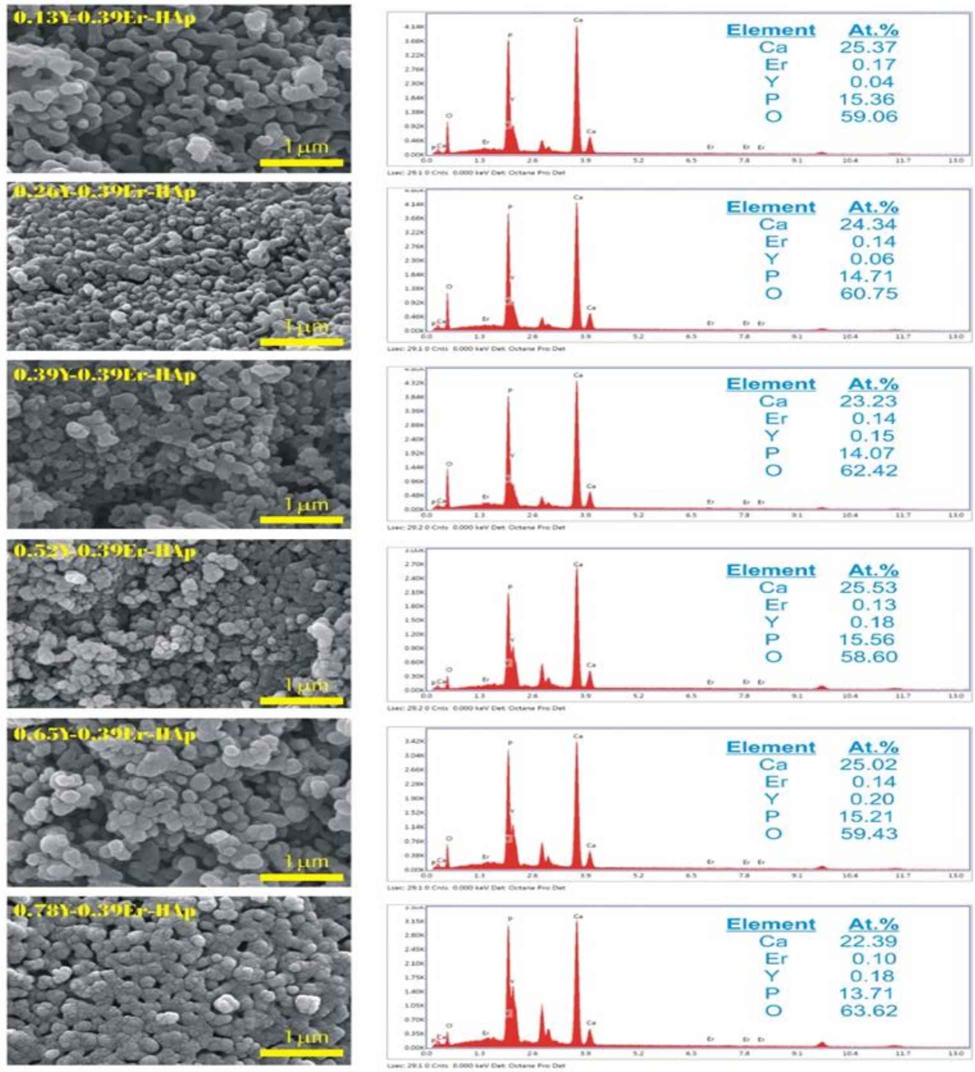

Figure 6.5. SEM images and EDX analysis report of the HAps doped with Y

Table 6.3. Theoretical and experimental values of the Ca/P and (Ca+Er+Y)/P ratios of the HAps doped with Y.

Samples	***Ca/P (Theo.)***	***Ca/P (Exp.)***	**(Ca+Er+Y)/P (Theo.)**	***(Ca+Er+Y)/P (Exp.)***
0.13Y-0.39Er-HAp	1. 6580	1.6517	1. 6667	1. 6654
0.26Y-0.39Er-HAp	1.6558	1.6547	1.6667	1.6682
0.39Y-0.39Er-HAp	1.6537	1. 6510	1.6667	1. 6716
0.52Y-0.39Er-HAp	1.6515	1.6408	1.6667	1.6607
0.65Y-0.39Er-HAp	1.6493	1.6450	1.6667	1.6673
0.78Y-0.39Er-HAp	1. 6472	1.6331	1.6667	1.6535

6.1.1.4 Differential Thermal Analysis (DTA) and Thermogravimetric Analysis (TGA) of Er/Y co-doped HAps

Figures 6.6 and 6.7 display the as-prepared HAp samples coupled with Er and Y in DTA and TGA thermograms. In Figure 6.6's DTA thermograms, there were no peaks connected to the breakdown of the HAp structure. As a consequence, according to findings from Ali et al. [112], all of the samples were determined to be thermally stable between ambient temperature and 900 °C. According to the study, Er-doped HAps' thermal stability could be improved and controlled by Y concentration.

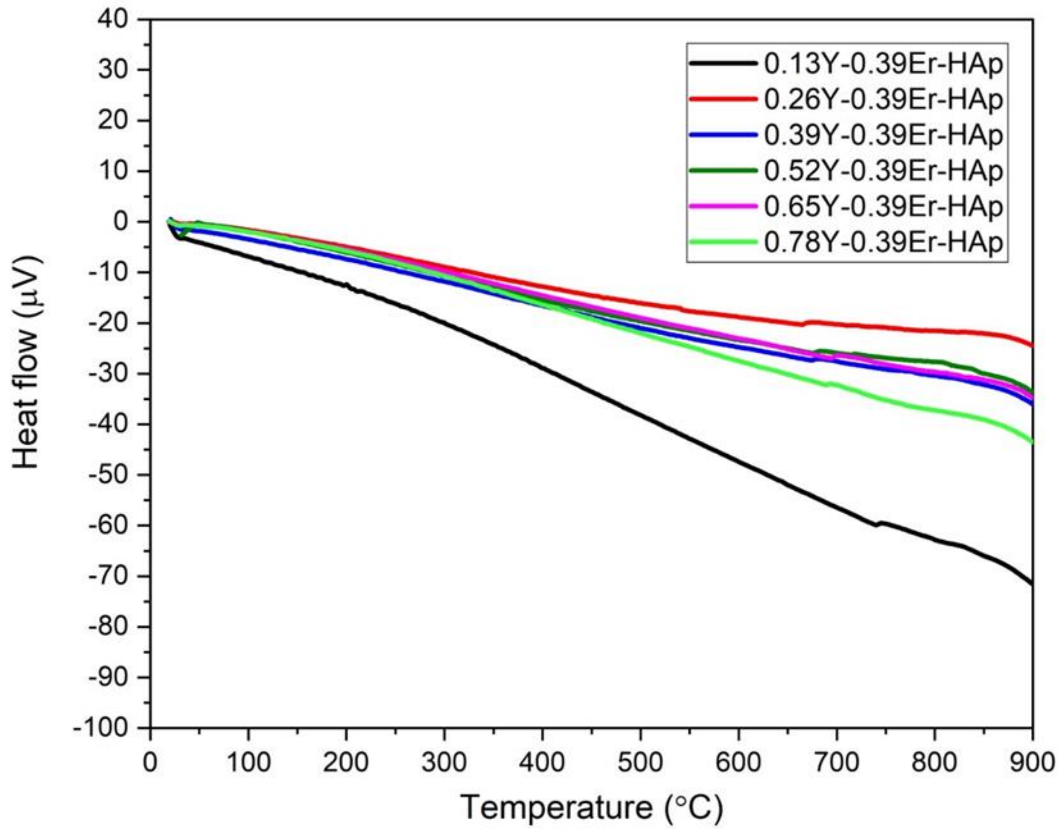

Figure 6.6. DTA thermograms of the HAps doped with Y.

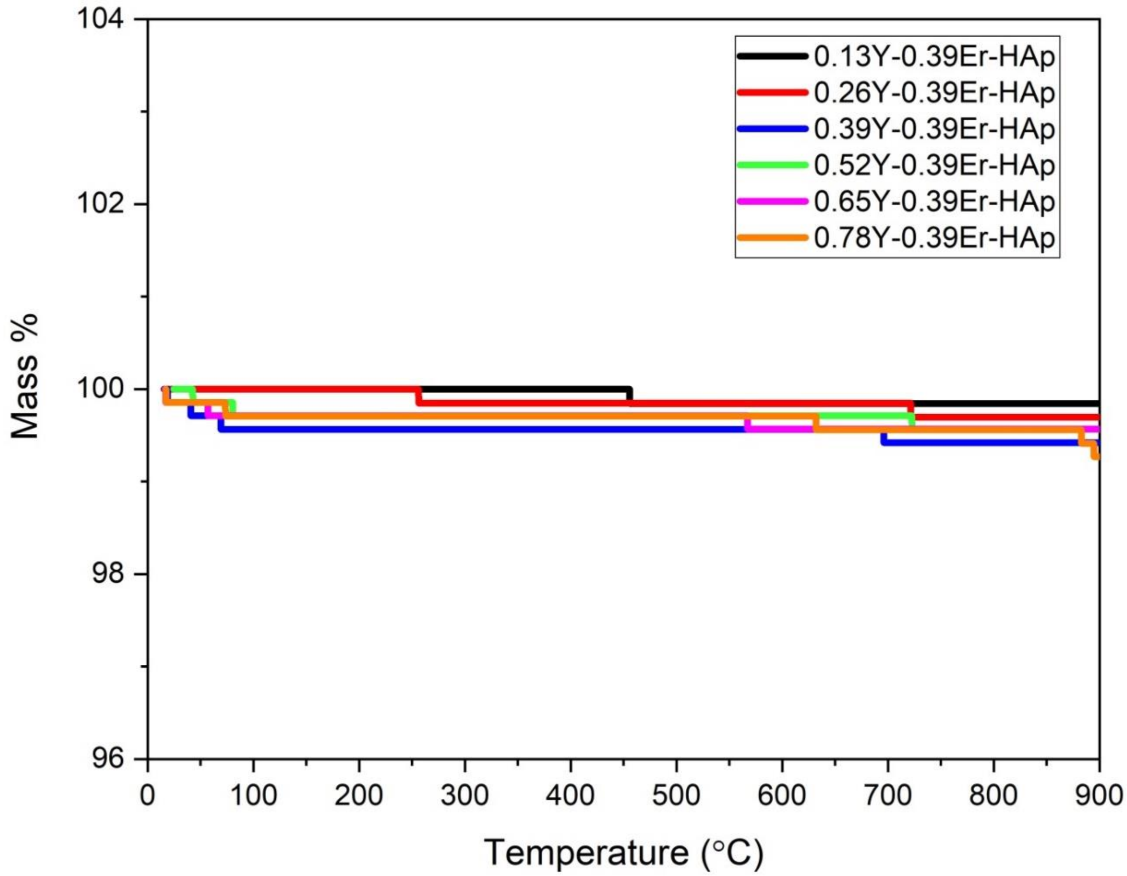

Figure 6.7. TGA thermograms of the HAps doped with Y

The TGA data in Figure 6.7 demonstrate no mass loss in as-prepared samples from room temperature to 900 °C. Additionally, the total mass losses for the following compounds were 0.16, 0.30, 0.58, 0.43, 0.43, and 0.73% for 0.13Y-0.39Er-HAp, 0.26Y-0.39Er-HAp, 0.39Y-0.39Er-HAp, 0.52Y-0.39Er-HAp, and 0.65Y-0.39Er-HAp, respectively. These losses are connected to the loss of lattice water and adsorbed water in the samples, which occur at temperatures between 200 °C and 400 °C, respectively [244, 245]. At temperatures over 400 °C, dehydroxylation of the HAp samples causes the remaining mass losses for all samples [242]. In the conducted study, these mass losses were more clearly discovered at temperatures above 600 °C, and they are consistent with earlier findings [246]. Dehydroxylation is shown by a reduction in the intensity of the band 3570 cm^{-1} in Figure 6.3. As a consequence, the mass losses attributed to the dihydroxylation process in the TGA data are supported by the FTIR results. Figure 6.8 displays the fluctuation in temperature that is based on the specific heat capacity (C_p). One of a substance's most notable thermodynamic properties is its specific heat capacity, whose value is influenced by the Y concentration and rising temperature, as shown in Figure 6.8. Compared to the Er-HAp sample, all of the Y-doped samples show much higher C_p values.

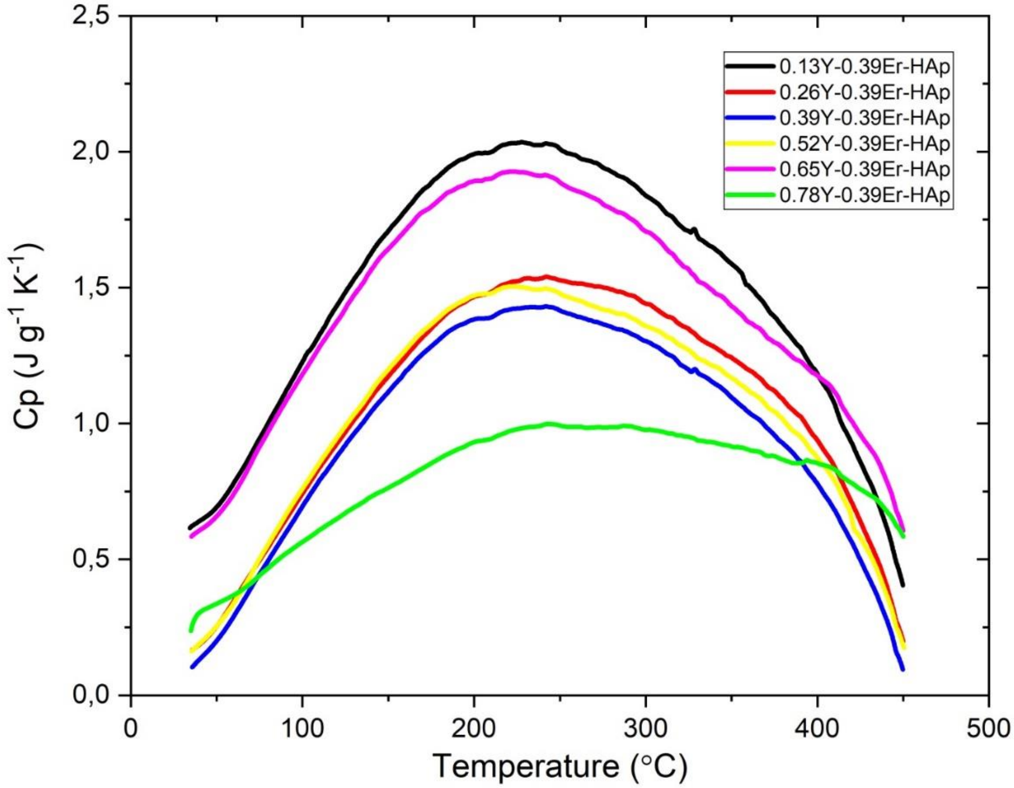

Figure 6.8. Heat capacity as a function of temperature plot of HAps doped with Y.

6.1.1.5 *In Vitro* Biocompatibility Results of Er/Y co-doped HAps

Mus musculus mouse fibroblast cells (L-929) were used to examine the biocompatibility of the indirect method formulations. Thermo Fisher Scientific provided the commercially available L929 Mouse Fibroblast cells utilized in this biocompatibility investigation. The samples exposed to the L-929 cells are depicted in Figure 6.9 and Figure 6.10, respectively, together with the results of the cell viability tests and optical microscope photographs. The standard deviations of the cell viability percentages were determined to be 100.00 ± 6.62, 110.49 ± 3.34, 110.91 ± 2.10, 110.40 ± 5.90, 110.50 ± 2.65, 111.29 ± 5.89, and 110.97 ± 4.50 for the control, 0.13Y-0.39Er/HAp, 0.26Y-0.39Er/HAp, 0.39Y-0.39Er/HAp, 0.52Y-0.39Er/HAp, 0.65Y-0.39Er/HAp, and 0.78Y-0.39Er/HAp, respectively. For *in vitro* biocompatibility data, statistical analysis was done. Between the control and treatment groups, changes were found that were statistically significant (p 0.05). The results showed very high cell viability values in Y/Er-HAp samples, ranging from 110.10 to 111.29%. Cell viability could be seen in more than 80% of the samples, which suggested that they were more biocompatible than the control. Therefore, it could be said that all samples are biocompatible. Figure 6.9 shows how the standard deviation changes depending on the proportion of Y/Er-

HAp samples. The 0.39Y-0.39Er-HAp sample has a greater standard deviation than the other samples, which might be attributed to the doping components' microstructure. At its lowest point for the 0.26Y-0.39Er-HAp, the deviation decreases as the proportion of Y changes.

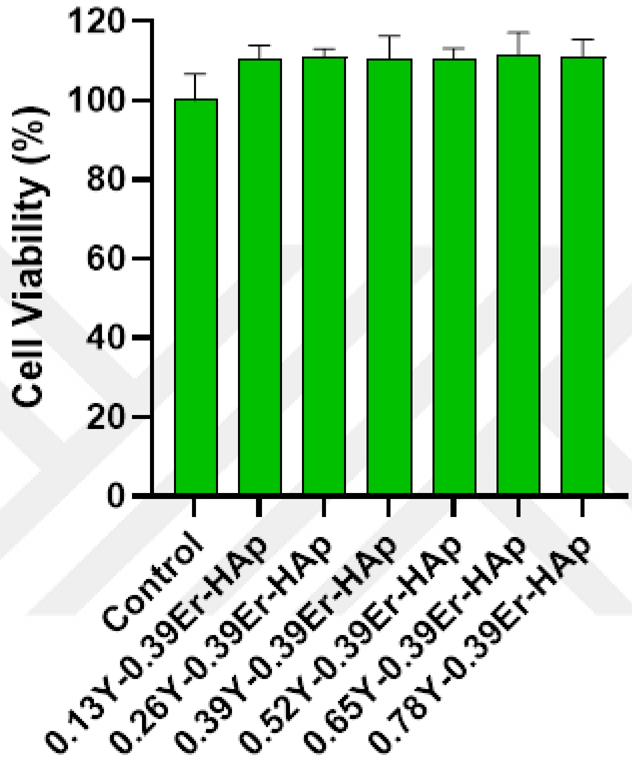

Figure 6.9. Cell viability level of L-929 cell exposed Y/Er-HAp samples. * Statistically significant ($p < 0.05$) in between control and treatment groups.

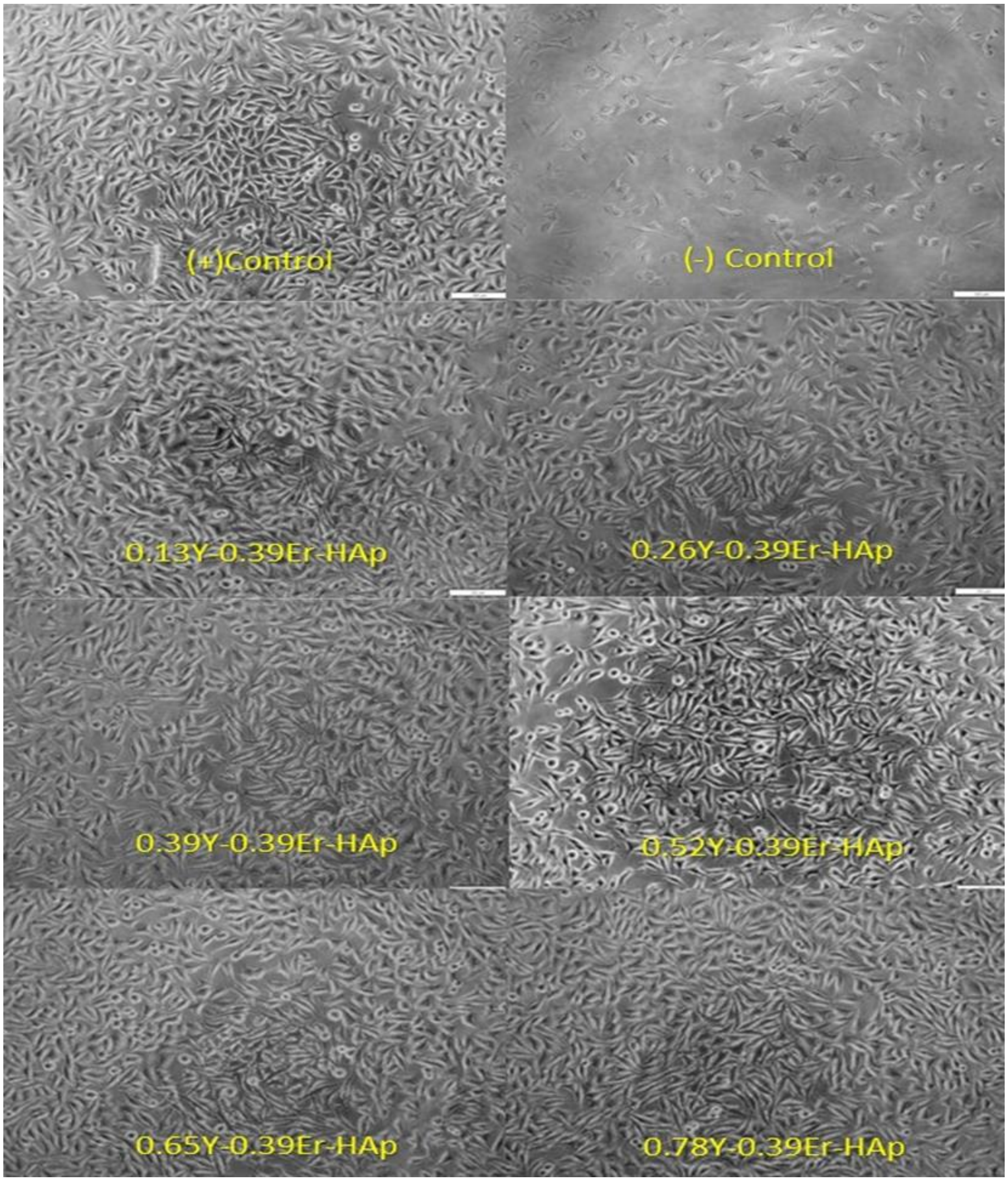

Figure 6.10. Optic microscope images for all the samples exposed to the L-929 cells of the HAps doped with Y

6.1.2 Theoretical Results of Er/Y co-doped HAps

6.1.2.1 Bandgap Structure and Density of States (DOS) Calculations of Er/Y co-doped HAps

Band structure and state density calculations for the materials were published previously [231]. For the interest of detail and organization, this section provides insight into some of the presented information. The equation below could be employed to estimate the electron density [247]:

$$DOS(E) = \sum g(E - \varepsilon_i) \quad (6.8)$$

In this computation, which takes into account each energy state, the number of states is multiplied by the probability that an electron will occupy each state. Here, the values for g, E, and ε_i stand for the Gaussian with a fixed FWHM, the total energy, and the energy of the *ith* molecular orbital, respectively. On the interaction of atoms inside a molecular structure, band structure, and DOS measurements are based. In a solid molecule, the quantity of divisions depends on the distance between two or more atoms at the atomic level. As energy levels divide more widely as a result of spin-orbit interactions and relativistic processes, band structure and DOS in the structure could be changed [232]. In Figure 6.11- Figure 6.12- Figure 6.13- Figure 6.14- Figure 6.15- and Figure 6.16, the calculated DOS and band structure are displayed. The Origin Lab software was used for all computations together with a DFT formalism. All samples' observed bandgaps performed (G-H) interval measurements. The surfaces of the valence and conduction bands appear to be almost flat in Figure 6.11- Figure 6.12- Figure 6.13- Figure 6.14- Figure 6.15- and Figure 6.16. Bandgap energies were determined to be 4.196 eV, 4.174 eV, 4.179 eV, 4.159 eV, 4.159 eV, and 4.156 eV for the following compounds respectively: 0.13Y-0.39Er/HAp, 0.26Y-0.39Er/HAp, 0.39Y-0.39Er/HAp, 0.52Y-0.39Er/HAp, 0.65Y0.39Er/HAp, and 0.78Y-0.39Er. Erbium (Er) has the electronic structure [Xe] $4f^{12}6s^2$, and Yttrium has the configuration [Kr] $4d^15s^2$. The inner shell electrons in the Xenon configuration make up the Er atom's additional electrons besides $4f^{12}6s^2$. Because it is smaller and nearer to restriction, the 4f level divides more than the 6s orbital. While the s orbitals have a minimal role in the electronic structure, the DOS associated by 4f states showed contributions to the bands. Except for 0.39Y-0.39Er/HAp, where the energy bandgap was raised, the molecule's energy bandgap was considerably reduced by the addition of Y atoms at various concentrations, from 4.196 eV to 4.156 eV, as was previously observed. Because doping alters the electronic states along symmetry lines, this may affect the bandgap value. The reduction in bandgap energy may also be connected to these changes [232]. This arrangement reduces the energy gap in the result when combined with yttrium (Y) as well as other elements in the HAp molecule because of its higher energy.

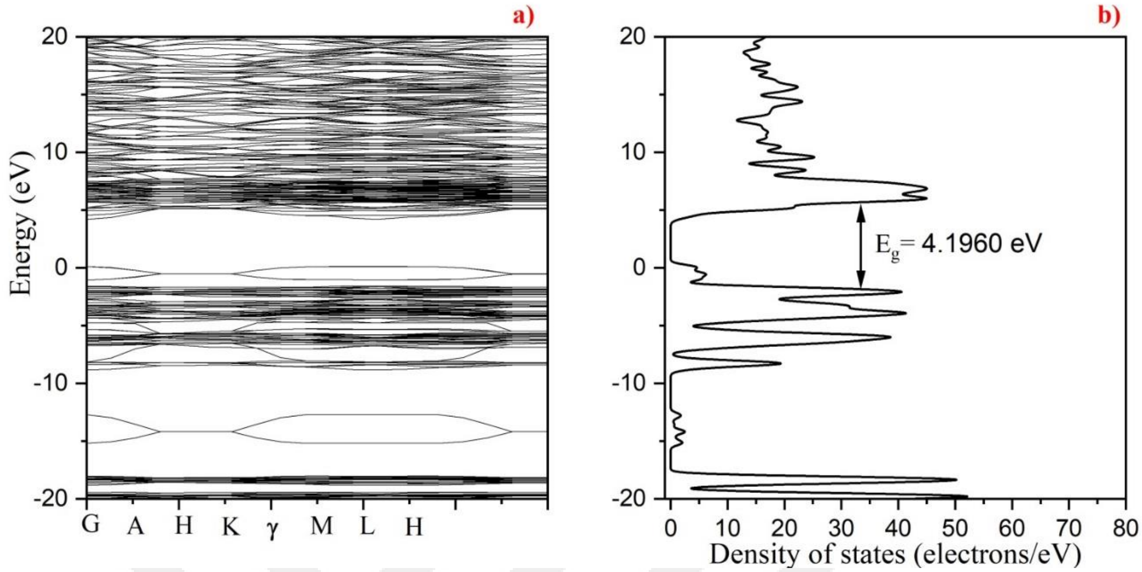

Figure 6.11. a) Band structure and **b)** density of states for 0.13Y0.39Er/HAp.

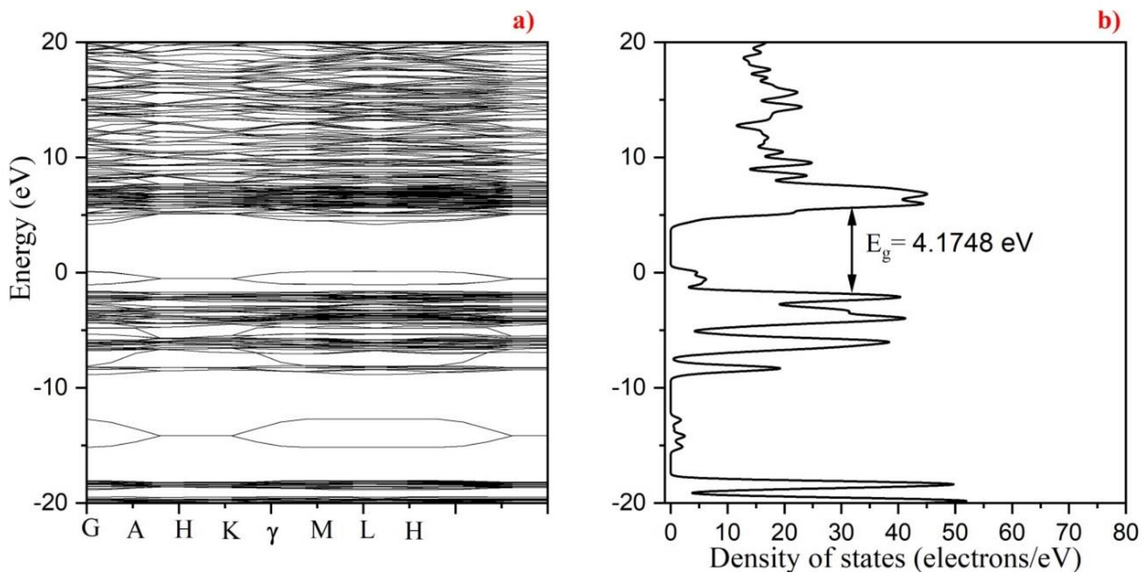

Figure 6.12. a) Band structure and **b)** density of states for 0.26Y0.39Er/HAp.

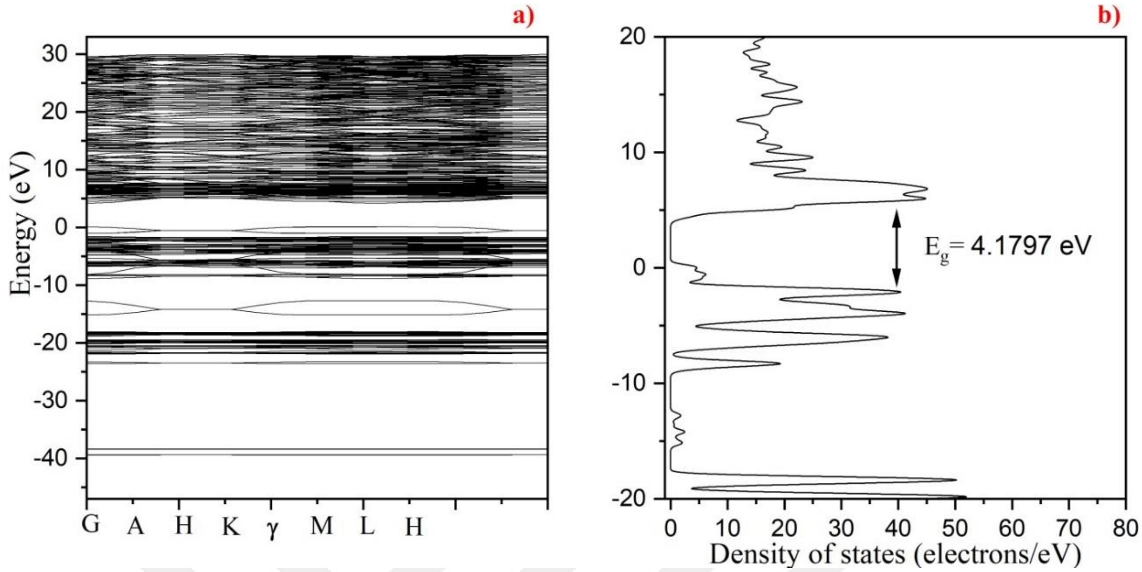

Figure 6.13. a) Band structure and **b)** density of states for 0.39Y0.39Er/HAp.

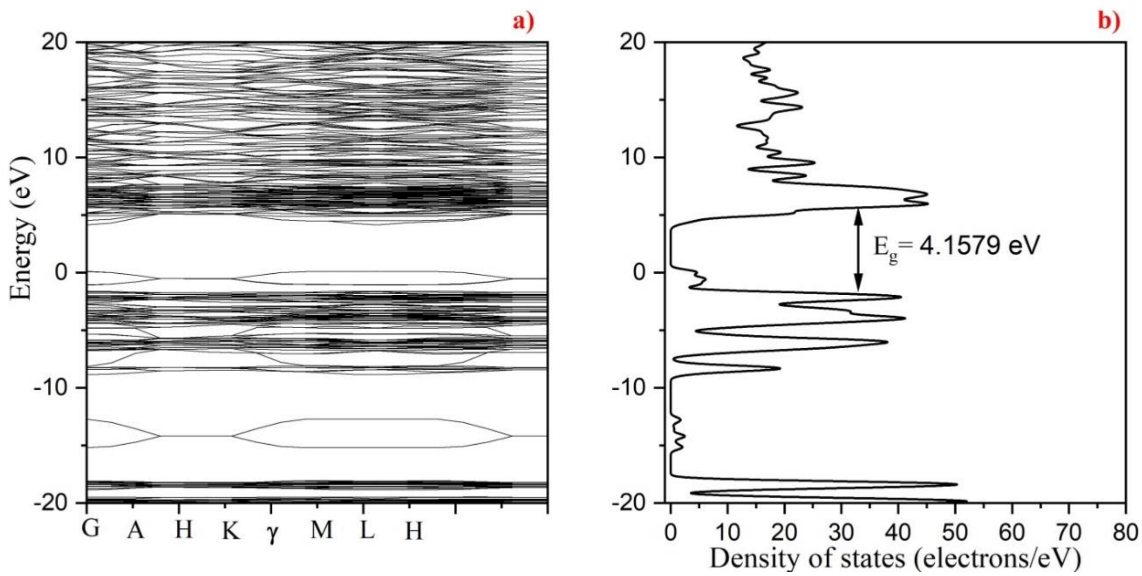

Figure 6.14. a) Band structure and **b)** density of states for 0.52Y0.39Er/HAp.

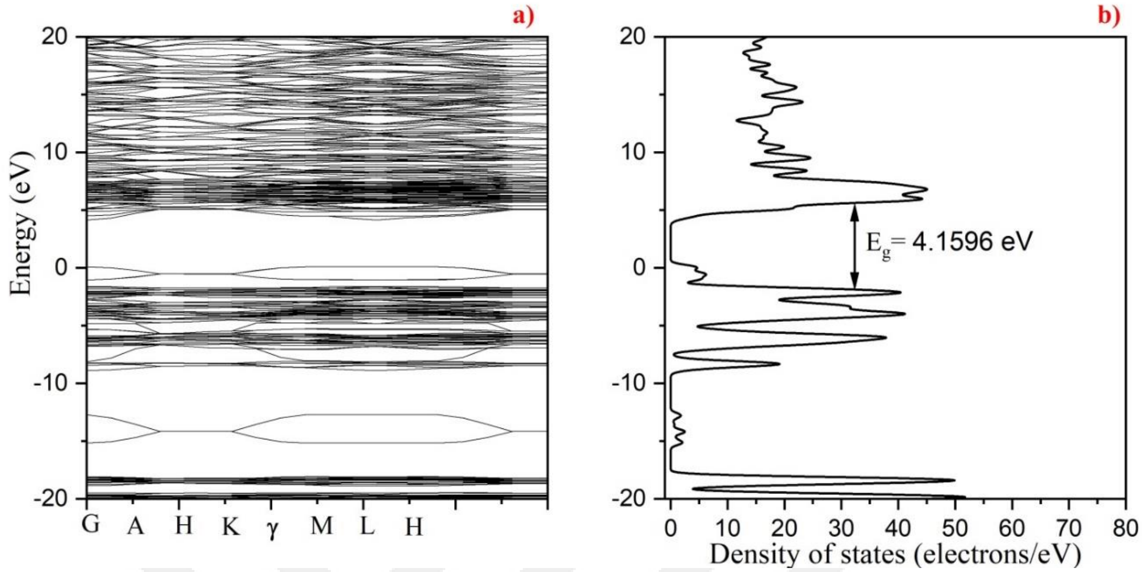

Figure 6.15. a) Band structure and **b)** density of states for 0.65Y0.39Er/HAp.

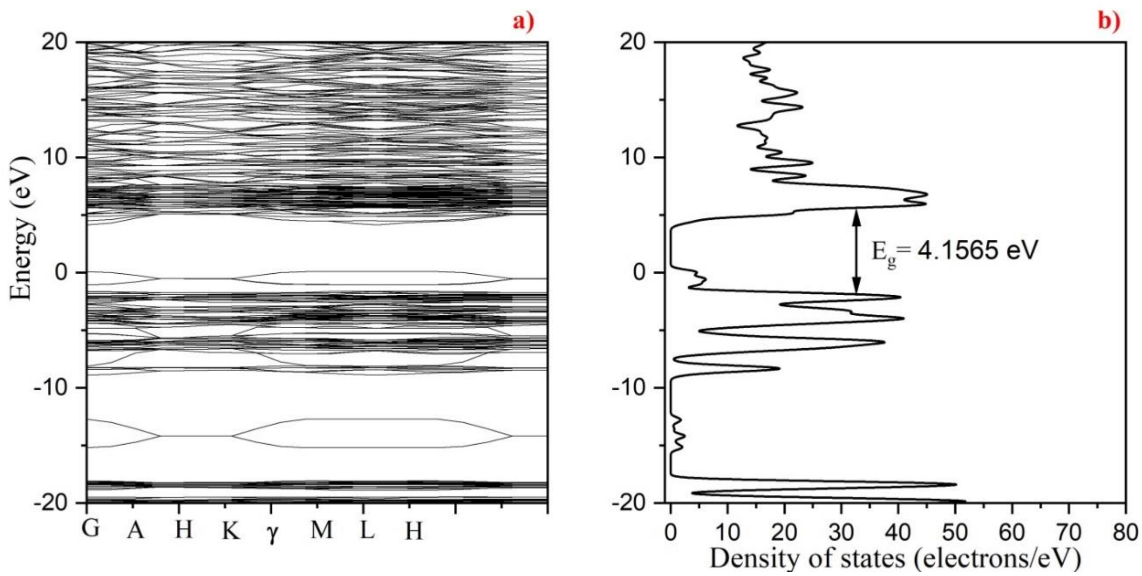

Figure 6.16. a) Band structure and **b)** density of states for 0.78Y0.39Er/HAp.

6.1.2.2 Density and Linear Absorption Coefficient Calculations of Er/Y co-doped HAps

The densities were found to be 3.1724, 3.1744, 3.1764, 3.1786, 3.1804, and 3.1824 g cm^{-3} for 0.13Y-0.39Er-HAp, 0.26Y-0.39Er-HAp, 0.39Y-0.39Er-HAp, 0.52Y-0.39Er-HAp, and 0.65Y-0.39Er-HAp, respectively. Ca (1.55 g cm^{-3}) has a lower density than Y (4.47 g cm^{-3}) and Er (9.07 g cm^{-3}) [248]. The inclusion of Y raised the density of the HAp system since the concentration of Er was kept constant. As a result, the density increases with increasing Y concentration. The linear absorption coefficient (LAC) is depicted as a function of photon energy in Figure 6.17. All structures experience a decline with increasing photon energy. In addition, the LAC value rises as the amount of Y contained increases. All materials are excellent candidates for radiation shielding and medical applications due to their electromagnetic radiation attenuation characteristics, and the obtained results are highly consistent with the literature [131, 232, 247, 249].

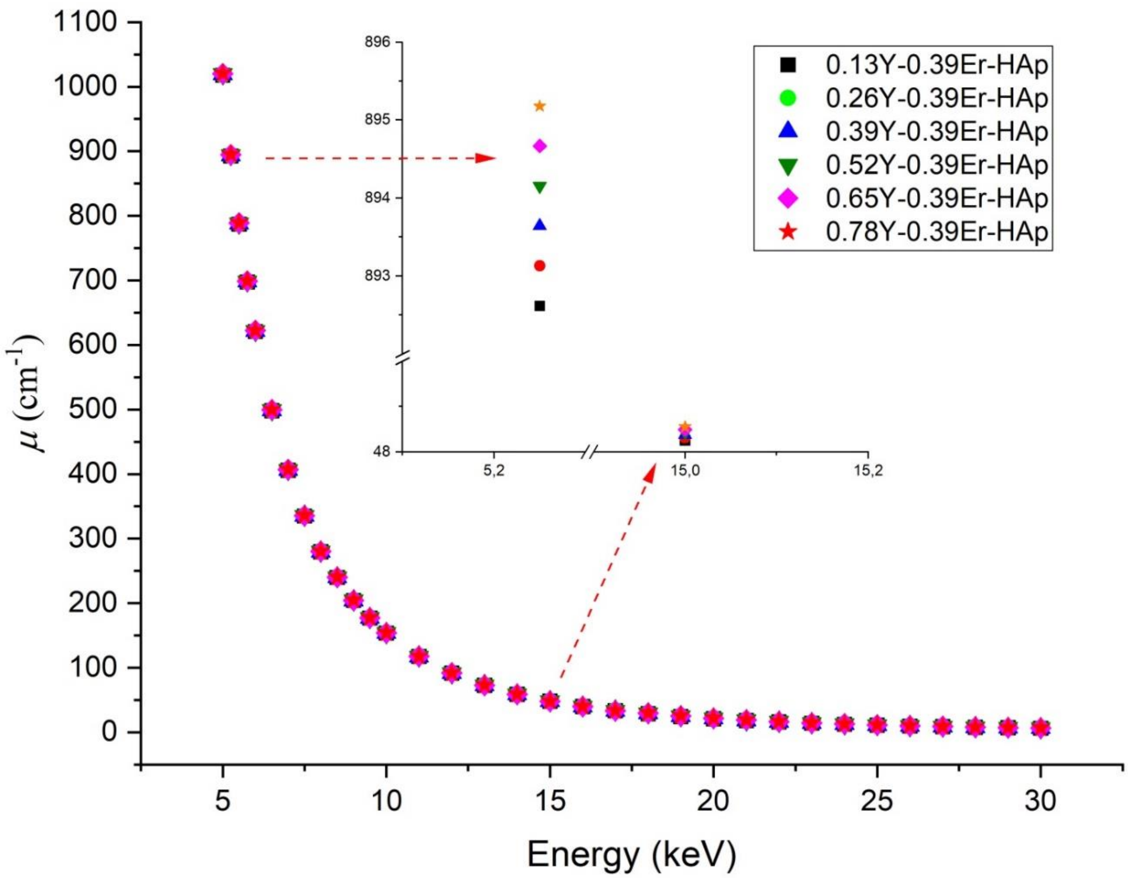

Figure 6.17. Energy-dependency of the linear absorption coefficient for HAp doped with Y.

6.2 Effects of Cerium Doping on Erbium-Based Hydroxyapatites

6.2.1 Experimental Results of Er/Ce co-doped HAps

6.2.1.1 XRD Analysis of Er/Ce co-doped HAps

The XRD results of the as-synthesized specimens are shown in Figure 6.18 All the as-detected XRD peaks were matched with the HAp phase (JCPDS no: 09-0432). Within the sensitivity limitations of the XRD method, the as-analyzed XRD patterns indicated that HAp was the single phase for all of the samples, with no secondary phase found. There is a little increase in intensity with the addition of Ce, as can be seen in the result in Figure 6.18. As previously stated, the effect of ionic doping on electron density causes some peaks to become less intense and/or more intense [227].

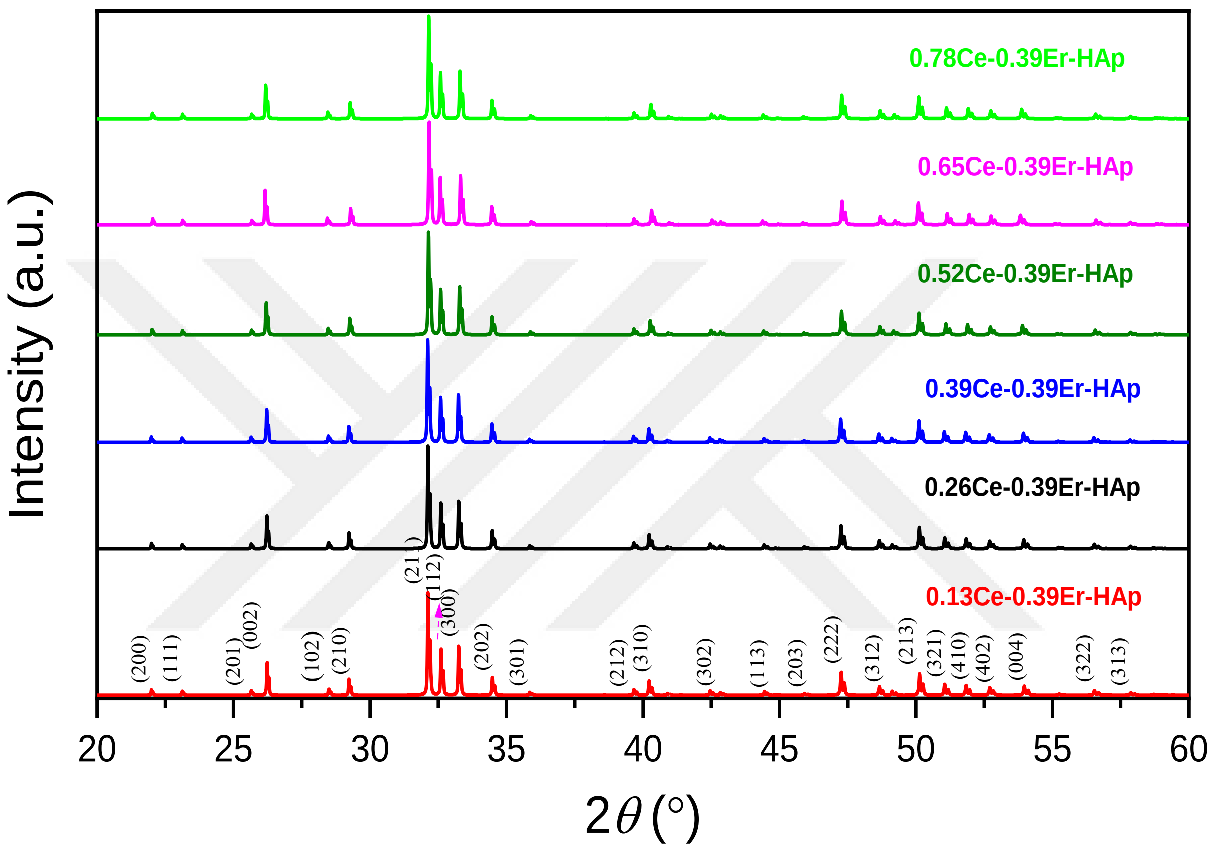

Figure 6.18. The XRD patterns of Er-based HAp samples doped with Ce in different quantities

The graph plotted $\beta\cos\theta$ vs. $4\sin\theta$ for all synthesized samples is shown in Figure 6.19a. The slope of the $\beta\cos\theta$ *vs*. $4\sin\theta E^{-1}$ presented in Figure 6.19b can be used to calculate the stress value for each sample. The slope in Figure 6.19c can be used to compute the *u* values.

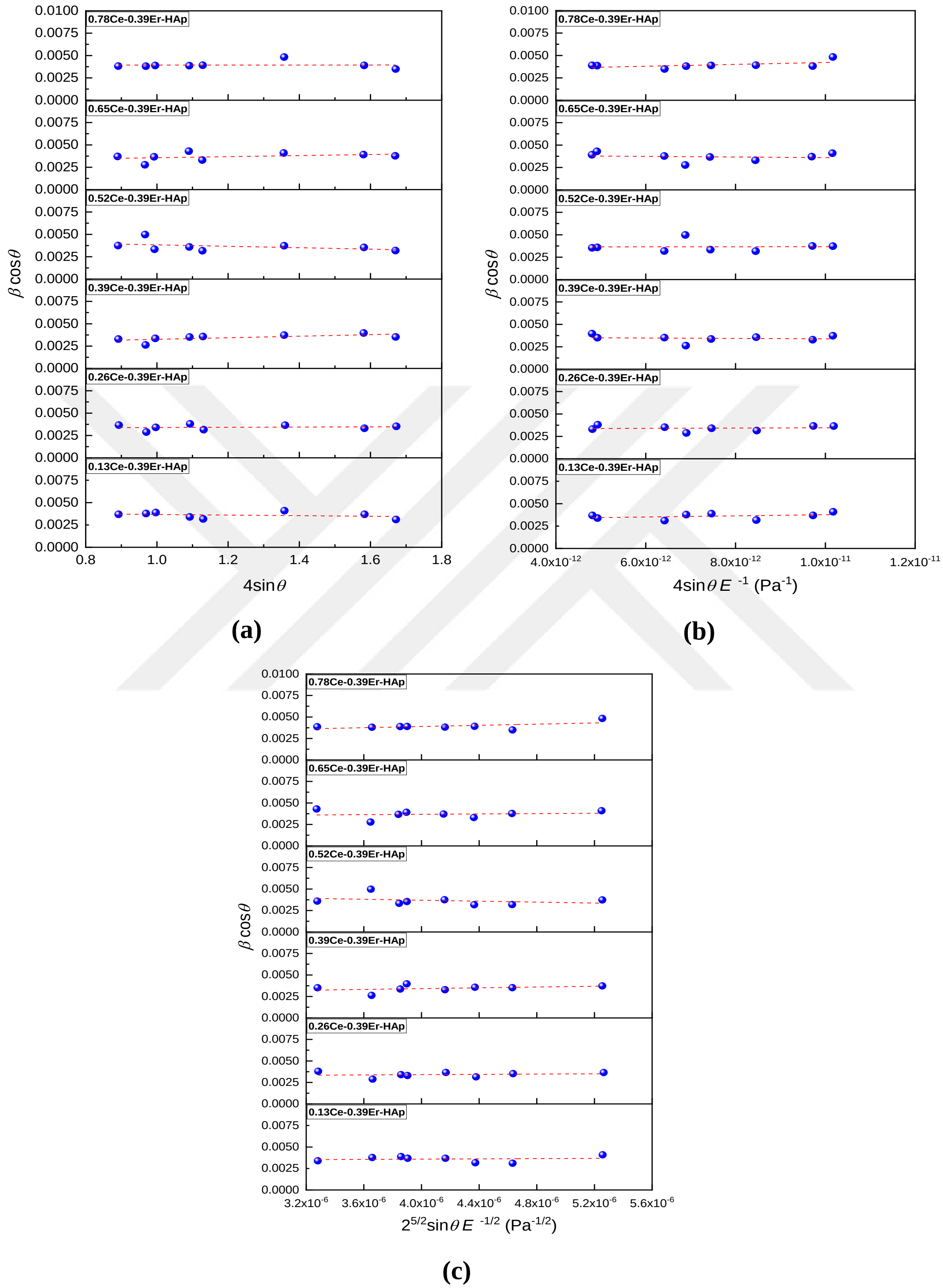

Figure 6.19. (a) The *βcosθ* vs. *4 sinθ*, **(b)** *βcosθ* vs. *4 sinθ* E^{-1}, and **(c)** *βcosθ* vs. $2^{5/2}$ *sinθ* $E^{-1/2}$ plots of the Er-based HAps doped with Ce

Table 6.4 presents the outcomes derived from theoretical and experimental computations for the parameters *a*, *c*, and *V*. In this table, theoretical *a* and *c* lattice parameters, and the *V* unit cell volume, do not decrease gradually. Furthermore, the experimental one indicates that the lattice parameters and unit cell volume vary non-gradually. All three of these parameters are significantly affected by the adding of Ce to the Er-HAp structure. Table 6.5 displays the computed crystallinity percent (*Xc%*) values, crystallite size values (D_S and D_{WH} computed from Scherrer and Williamson-Hall equations), lattice strain, stress, and anisotropic energy density for each sample. According to the table, the addition of Ce to the Er-HAp causes differences in the crystallinity, varying from 88.7 % to 83.1 %. Some changes in the crystallite size value have been seen due to the replacement of Ce^{3+} with a high ionic radius (0.101 nm) and Er^{3+} with a low ionic radius (0.088 nm) to Ca^{2+} with an ionic radius of 0.099 nm [228, 250]. These variations in crystallite size could be related to the progress of lattice strain, which can lead to HAp structure crystal lattice deformation [236]. In addition, Ce^{3+}, Er^{3+}, and Ca^{2+} ions have a charge imbalance. The attachment of each Ce and Er to each Ca ion may change the distributions of these ions. The quantity of Ce, influences crystallite size. The D_S and D_{WH} values also revealed non-gradual changes. The lattice strain ε values are both negative and positive. The resulting negative lattice strain implies that the unit cell is under compressive stress, whereas the positive one suggests that it is under tensile stress [237]. Furthermore, as demonstrated in Table 6.5, the stress (σ) values and anisotropic energy density (u) of all samples varied with Ce doping. Tensile and compressive stresses produce positive and negative values because of their proportionality with strain [247]. The u values have been calculated using the $\beta cos\theta$ vs. $2^{5/2}\sin\theta\, E^{-1/2}$ plot shown in Figure 6.19c. Except for the sample doped with 0.65Ce-0.39Er-HAp, in which the anisotropic energy density value is less than 12 kJ m^{-3}, all point u values in Table 6.5 are more than the reported value of 12 kJ m^{-3} for the un-doped HAp [238].

Table 6.4. Lattice parameters and unit cell volume for theoretical and experimental results HAp samples doped with Ce.

	Theoretical			***Experimental***		
Samples	***a* (nm)**	***c* (nm)**	***V* (nm)^3**	***a* (nm)**	***c* (nm)**	***V* (nm)^3**
0.13Ce-0.39Er-HAp	0.93257	0.67905	0.51143	0.94402	0.68946	0.53210
0.26Ce-0.39Er-HAp	0.93254	0.67927	0.51156	0.94342	0.68914	0.53117
0.39Ce-0.39Er-HAp	0.93282	0.67941	0.51197	0.94484	0.69004	0.53347
0.52Ce-0.39Er-HAp	0.93166	0.67985	0.51103	0.94531	0.69036	0.53425
0.65Ce-0.39Er-HAp	0.93068	0.68072	0.51061	0.94619	0.69082	0.53560
0.78Ce-0.39Er-HAp	0.93122	0.68019	0.51080	0.94492	0.68979	0.53337

Table 6.5. Characteristic of samples (where $X_C\%$: crystallinity percent, D_S and D_{WH}: crystallite size, σ: lattice strain, ε: stress, and u : anisotropic energy density) HAp samples doped with Ce.

Samples	$X_C\%$	D_S (nm)	D_{WH} (nm)	$\varepsilon\times10^{-4}$	σ (MPa)	u (kJ m^{-3})
0.13Ce-0.39Er-HAp	87.21	38.85	34.66	-3.274	64.027	5.460
0.26Ce-0.39Er-HAp	88.66	40.86	42.40	1.213	15.344	6.562
0.39Ce-0.39Er-HAp	85.92	40.78	48.14	8.634	-22.078	54.054
0.52Ce-0.39Er-HAp	85.55	38.59	30.01	-7.970	3.422	75.581
0.65Ce-0.39Er-HAp	83.12	38.18	46.68	5.984	-34.330	10.300
0.78Ce-0.39Er-HAp	86.16	35.47	35.19	0.014	104.361	118.370

6.2.1.2 FTIR and Raman spectroscopy of Er/Ce co-doped HAps

Figure 6.20 displays FTIR plots for samples of HAp. It was found that phosphate and hydroxyl bands were present. The phosphate group's vibration modes are related to the bands at wavenumber locations 468, 562, 597, 961, and 1019 cm^{-1} [239, 240]. The hydroxyl group's vibration mode is associated with the bands at 633 cm^{-1} and 3566 cm^{-1} [241, 242]. The FTIR spectra of each sample show all the bands that were seen, which supports the existence of the HAp structure [36].

Figure 6.21 represents the Raman spectra of the samples, which ranged from 100 to 4000 cm^{-1}. The phosphate group was found at 428 cm^{-1} a symmetric O-P-O bending mode, an antisymmetric O-P-O bending mode was found at 587 cm^{-1}, at 962 cm^{-1} a symmetric P-O stretching mode was fond, at 995 cm^{-1} an asymmetric P-O stretching mode, and 1080 cm^{-1} an asymmetric P-O stretching mode was found. At 3574 cm^{-1}, the band associated with the Stretching of the hydroxyl group was seen.

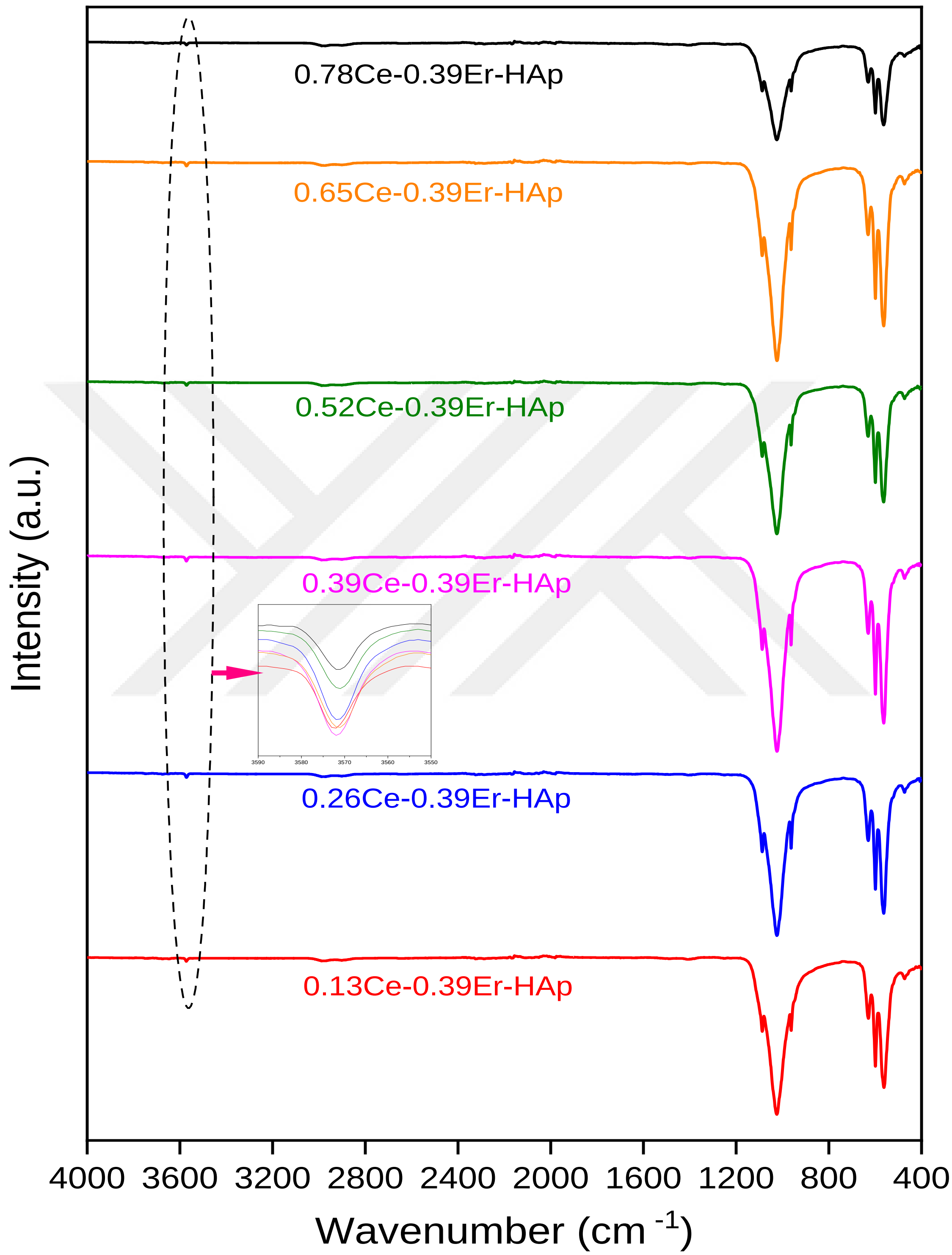

Figure 6.20. The FTIR findings of the HAp samples doped with Ce

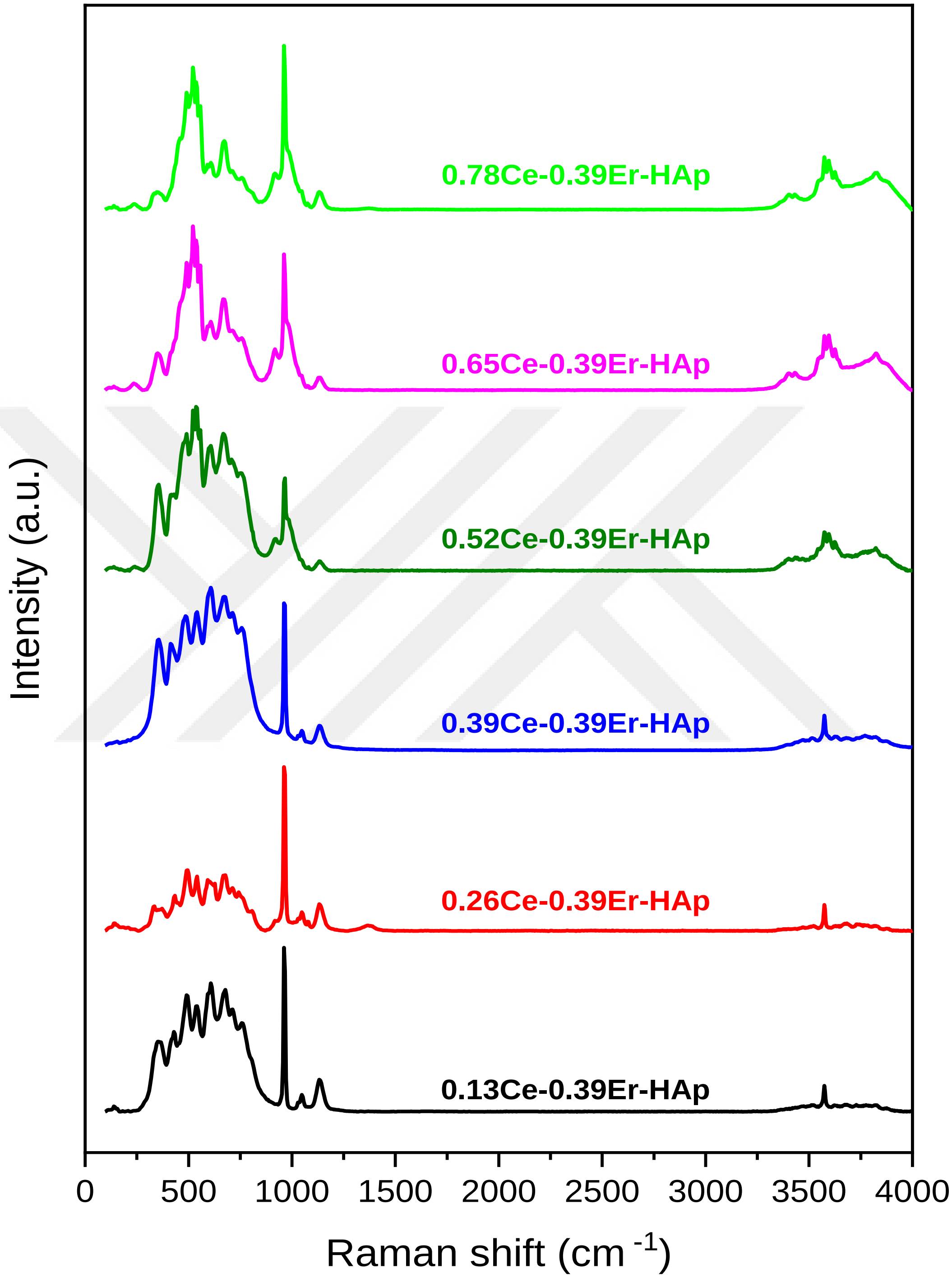

Figure 6.21. The Raman spectra of the HAp samples doped with Ce

6.2.1.3 Morphological analysis of Er/Ce co-doped HAps

Figure 6.22 shows SEM pictures and EDX data of as-produced co-doped HAps. The samples are all made up of sphere-shaped stacked nanoparticles. The EDX data confirm that Er and Ce have been added to the HAp structure. Although Ce adding into the apatitic structure is limited, the as-detected Ce content rises with Ce addition, as expected. In a conclusion, large amounts of the Ce dopant can be attributable to its deposition on the HAp surface. Ca/P and (Ca+Er+Ce)/P's experimental and theoretical values are thoroughly compared in Table 6.6. The theoretical and experimental results are very close to each other. For both molar ratios, there are less than 1% differences between theoretical and experimental values for all samples.

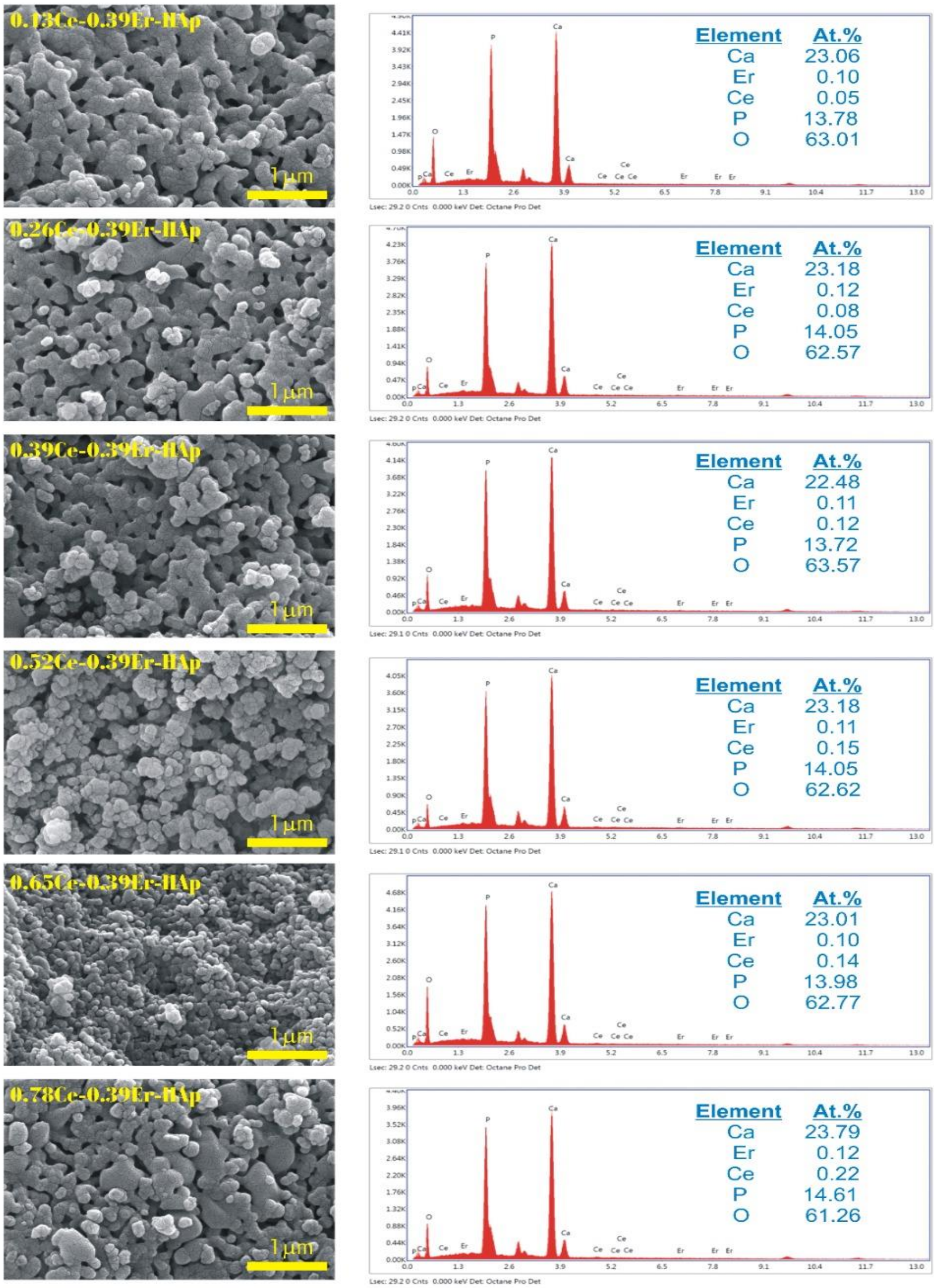

Figure 6.22. SEM images and EDX analysis report of the HAp samples doped with Ce

Table 6.6. Theoretical and experimental values of the Ca/P and (Ca+Er+Ce)/P ratios of the HAp samples doped with Ce.

Samples	*Ca/P (Theo.)*	*Ca/P (Exp.)*	(Ca+Er+Ce)/P (Theo.)	*(Ca+Er+Ce)/P (Exp.)*
0.13Ce-0.39Er-HAp	1. 6580	1.6734	1. 6667	1. 6843
0.26Ce-0.39Er-HAp	1.6558	1.6498	1. 6667	1.6641
0.39Ce-0.39Er-HAp	1.6537	1. 6385	1. 6667	1.6552
0.52Ce-0.39Er-HAp	1.6515	1.6463	1. 6667	1.6683
0.65Ce-0.39Er-HAp	1.6493	1.6459	1. 6667	1.6631
0.78Ce-0.39Er-HAp	1. 6472	1.6283	1. 6667	1.6516

6.2.1.4 Differential Thermal Analysis (DTA) and Thermogravimetric Analysis (TGA) of Er/Ce co-doped HAps

DTA and TGA thermograms of as-prepared HAp samples co-doped with Er and Ce can be seen in Figure 6.23 and Figure 6.24. Because the DTA thermograms in Figure 6.23 showed no peak related to the decomposition of the HAp phase, all of the samples are thermally stable from room temperature to 900 °C, and these results are similar to those stated by *Ali et al*. [112]. The sample with the highest concentration of Ce is the most stable of the bunch. According to the research, Ce concentration can improve and manage the thermal stability of Er-doped HAps.

The TGA data in Figure 6.24 demonstrate that there are mass losses in the as-prepared samples from room temperature to 900 °C. Total mass losses for 0.13Ce-0.39Er-HAp, 0.26Ce-0.39Er-HAp, 0.39Ce-0.39Er-HAp, 0.52Ce-0.39Er-HAp, 0.65Ce-0.39Er-HAp, and 0.78Ce-0.39Er-HAp are 0.46, 0.30, 0.44, 0.30, 0.32, and 0.79%, respectively. The removal of adsorbed and lattice water from the samples can be linked to these losses [244, 245]. Dehydroxylation of the HAp samples is in charge of the residual mass losses for all samples at temperatures higher than 400 °C [242]. These mass losses were more clearly identified beyond 600 °C in the current work, and they are consistent with the literature [246]. The FTIR graphs in Figure 6.20 show a drop in the intensity of the band 3571 cm^{-1}, indicating dehydroxylation.

Figure 6.25 displays the temperature-dependent graphs of the particular C_p for each sample. The specific heat capacity of a material is one of its most noticeable thermodynamic properties. As shown in Fig. 6.25, rising temperature and Ce quantity alter this parameter. Compared to the HAp sample that was simply doped with Er, all of the Ce-doped samples have much higher C_p values.

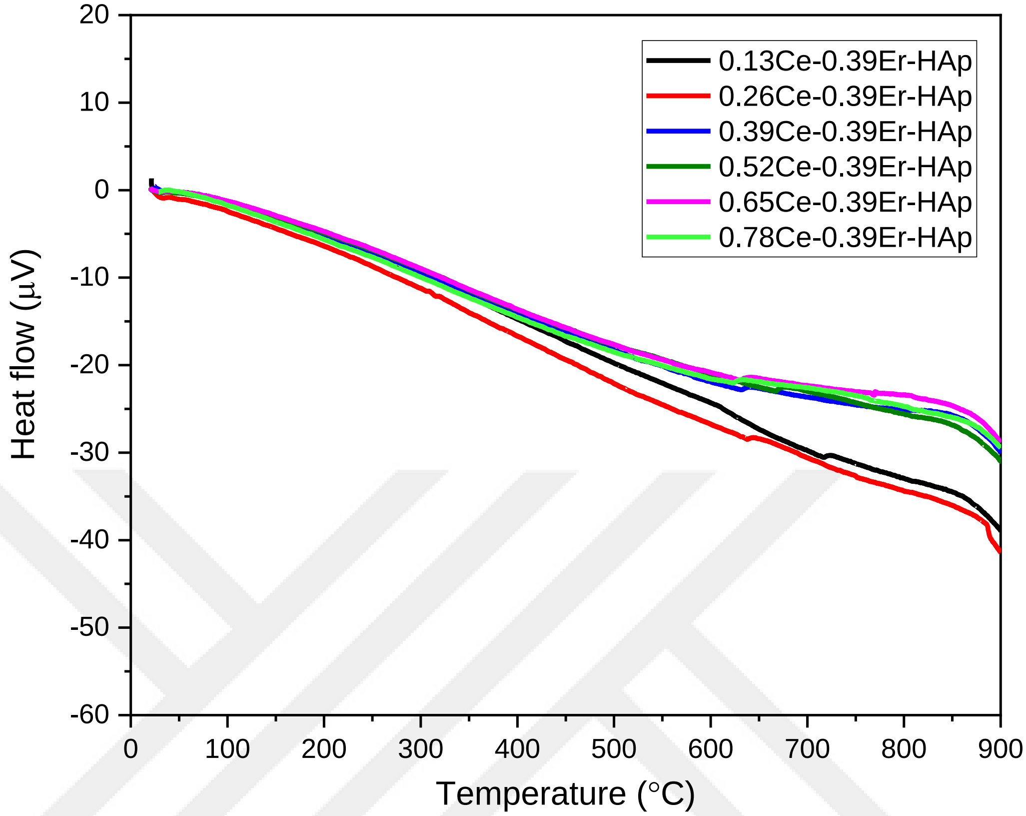

Figure 6.23. Thermograms of the HAp doped with Ce samples produced with DTA.

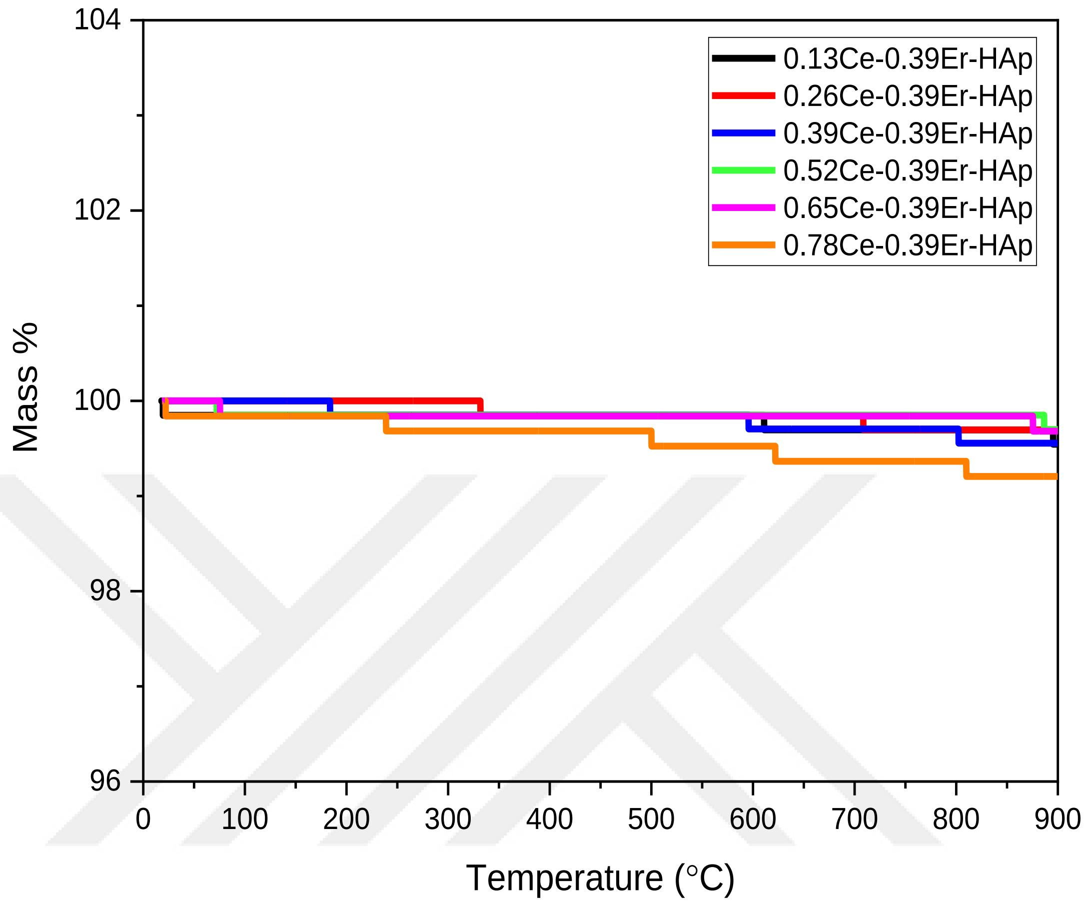

Figure 6.24. TGA thermograms for the HAp doped with Ce samples

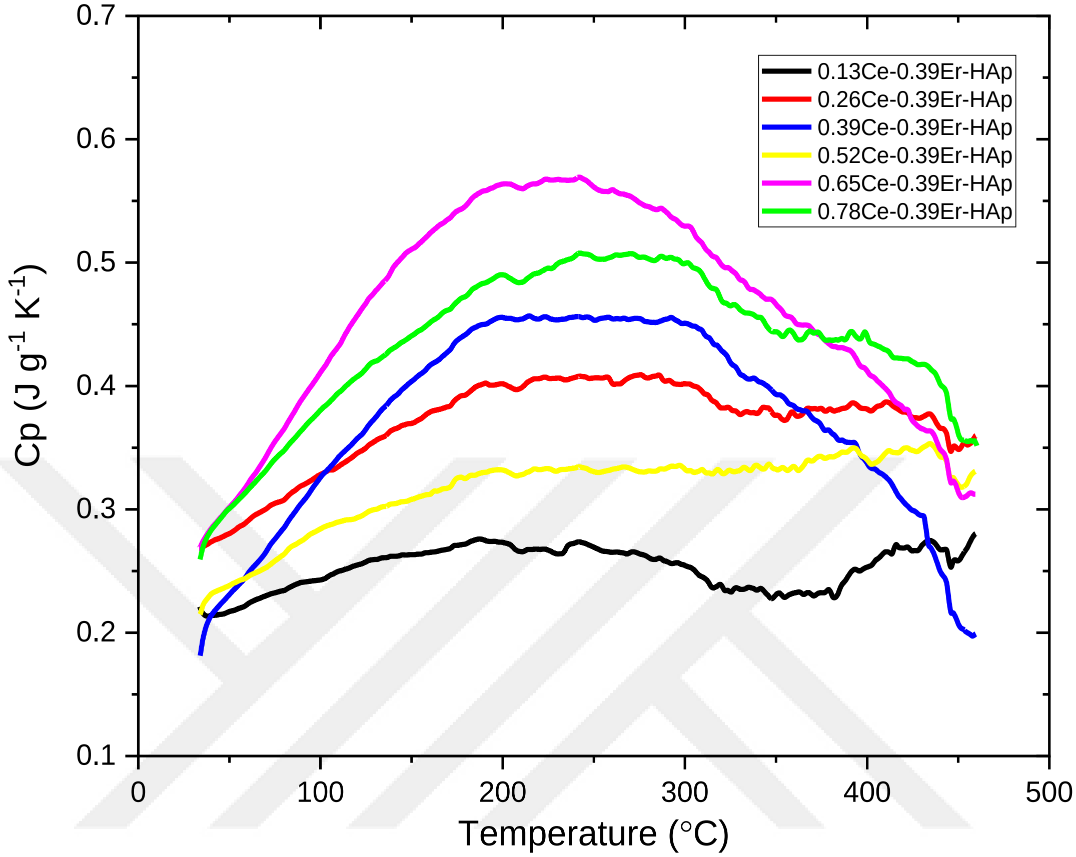

Figure 6.25. Specific heat capacity vs. temperature plots of the HAp samples doped with Ce

6.2.1.5 *In Vitro* Biocompatibility Results of Er/Ce co-doped HAps

The biocompatibility assessment of the formulations for the indirect approach involved the utilization of L-929 mouse fibroblast cells, specifically belonging to the Mus musculus species. Table 6.7 and Figure 6.26 show the cell viability results and Figure 6.27 demonstrated the optical microscope photographs. According to the results, all the Ce/Er co-doped HAp samples exhibited very high cell viability levels in the range of 105.92% and 113.15%. As known, the samples with cell viability higher than 80% can be accepted as biocompatible. Therefore, we can say that all the samples analyzed in this study can be used in biological and medical applications as appropriate implant material in the future.

Table 6.7. L-929 cell viability after exposure to Ce/Er-HAp samples doped with Ce

Sample	Cell Viability (%)	Std. Dev.
Control	100.00	3.67

0.13Ce-0.39Er-HAp	109.90	8.44
0.26Ce-0.39Er-HAp	112.92	7.37
0.39Ce-0.39Er-HAp	108.34	5.48
0.52Ce-0.39Er-HAp	113.15	6.32
0.65Ce-0.39Er-HAp	112.17	3.07
0.78Ce-0.39Er-HAp	105.92	7.69

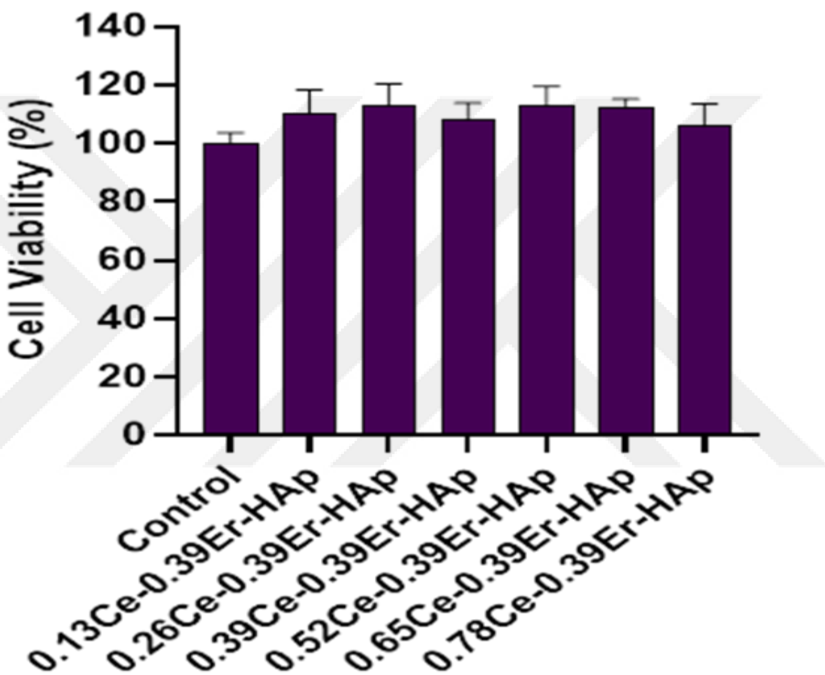

Figure 6.26. Cell viability of Ce/Er-HAp samples subjected to L-929 cells of the HAp samples doped with Ce

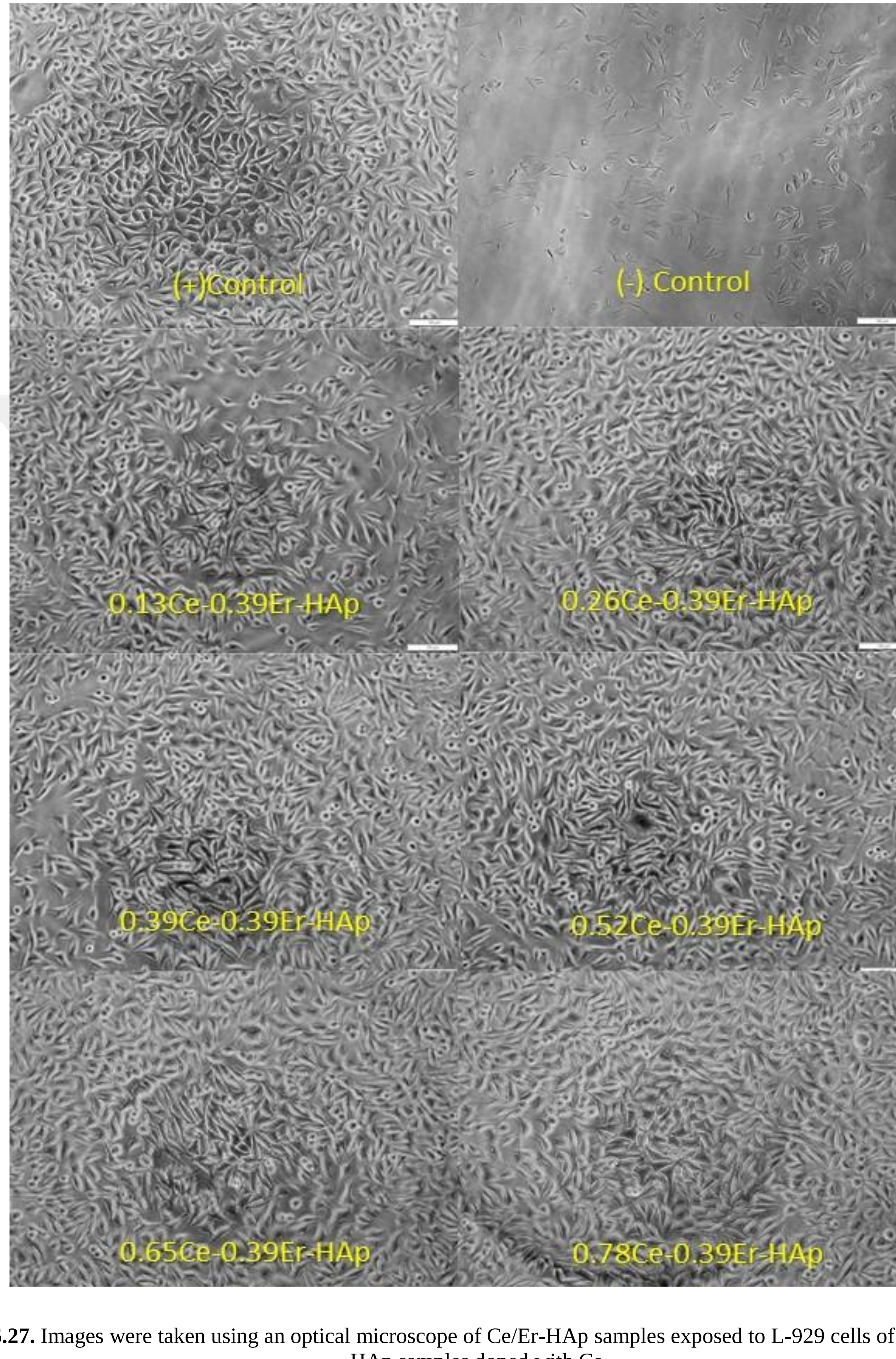

Figure 6.27. Images were taken using an optical microscope of Ce/Er-HAp samples exposed to L-929 cells of the HAp samples doped with Ce.

6.2.2 Theoretical Results of Er/Ce co-doped HAps

6.2.2.1 Calculations of the Bandgap and Density of States of Er/Ce co-doped HAps

Figure 6.13- Figure 6.14- Figure 6.15- Figure 6.16- Figure 6.17- and Figure 6.18 depict the calculated density of state and band structure for all studied samples. The DFT method and Origin Lab have been used for the theoretical calculations. To calculate the energy of the bandgap between the High Occupied Molecular Orbital (HOMO) and the Lower Unoccupied Molecular Orbital (LUMO), a DFT method was used. The obtained band gap was measured at (G-H) points. The valence and conduction band surfaces nearly look to be flat in Figures 6.28- Figure 6.29- Figure 6.30- Figure 6.31- Figure 6.32- and Figure 6.33. For 0.13Ce-0.39Er-HAp, 0.26Ce-0.39Er-HAp, 0.39Ce-0.39Er-HAp, 0.52Ce-0.39Er-HAp, 0.65Ce-0.39Er-HAp, and 0.78Ce-0.39Er-HAp, the bandgap energy values indicated 4.1591, 4.1688, 4.1335, 4.1352, 4.1137, and 4.1053 eV, respectively. Erbium (Er) has the electron configuration [Xe] $4f^{12}6s^2$. Whereas cerium (Ce) has the electron configuration [Xe] $4f^1 5d^1 6s^2$. The Er atom's surplus electrons are strongly bound by the closed-shell atomic layers featuring Xenon configuration. Because the 6s orbital is smaller and closer to limitation, the 4f level splits more than the 6s orbital. The f orbital contribution to the bands has the highest density of states in the figures. It's also fair to expect s orbitals to play a minor role in the DOS structure. The molecule's energy gap was gradually reduced from 4.1591 eV to 4.1053 eV by adding Ce atoms in various amounts, as indicated above, except for 0.26Ce-0.39Er-HAp and 0.52Ce-0.39Er-HAp, where the energy bandgap was raised. Changes in electronic states along symmetry lines could be related to the decrease in bandgap energy and may have an impact on the bandgap value due to doping [232]. When coupled with cerium (Ce) and other atoms in the HAp molecule, this arrangement decreases the energy gap in the product. When energy levels rise, greater splitting occurs in general.

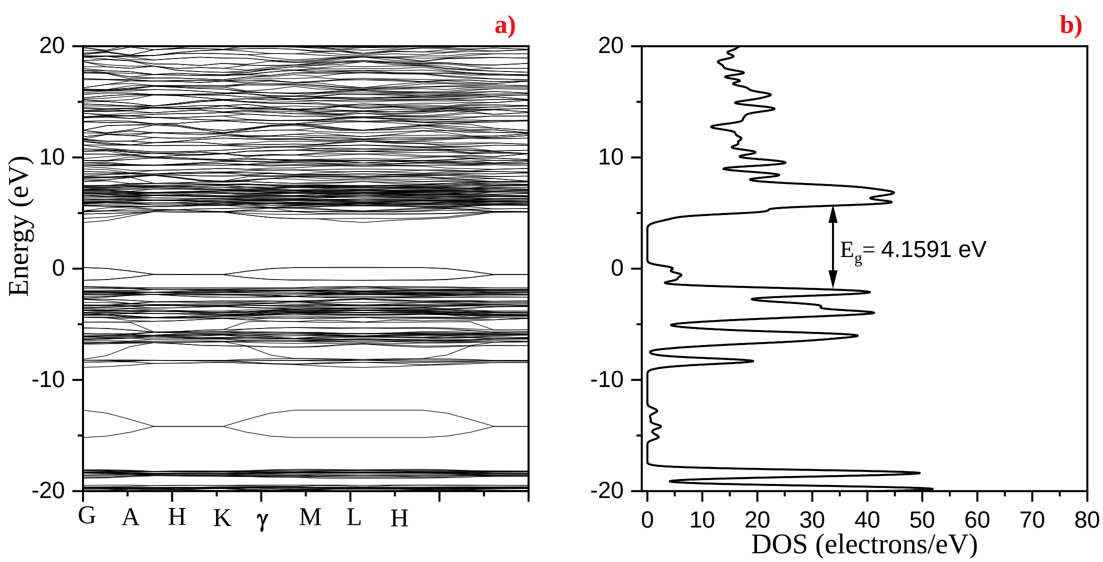

Figure 6.28. a) Band structure and **b)** density of states for 0.13Ce-0.39Er-HAp.

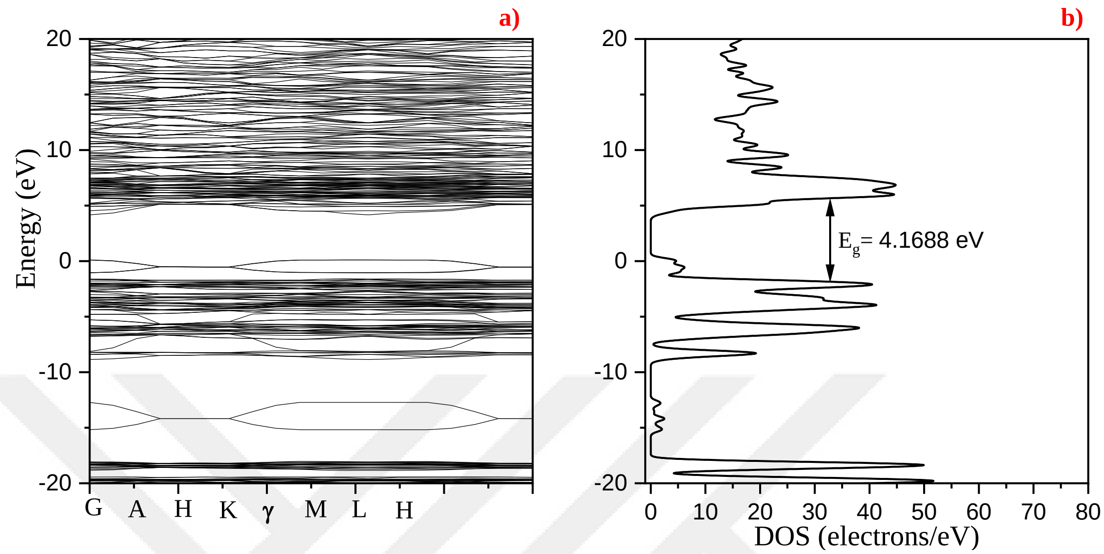

Figure 6.29. a) Band structure and **b)** density of states for 0.26Ce-0.39Er-HAp.

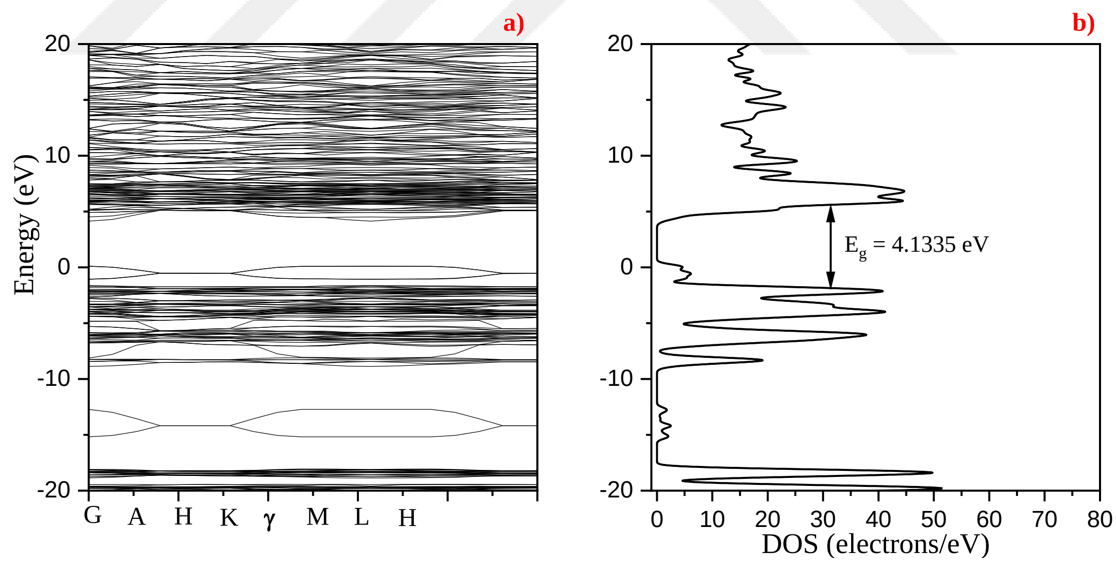

Figure 6.30. a) Band structure and **b)** density of states for 0.39Ce-0.39Er-HAp.

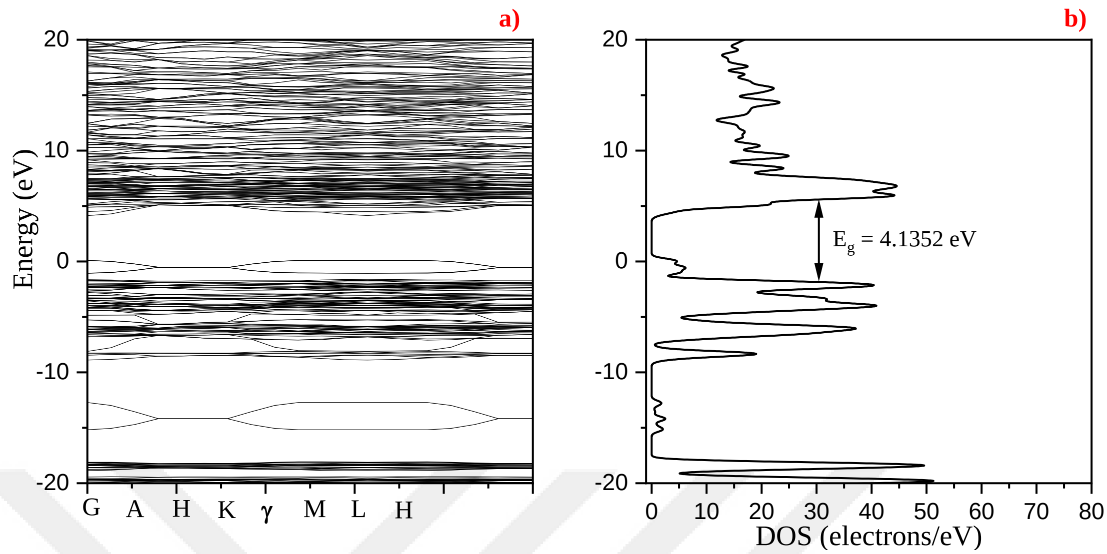

Figure 6.31. a) Band structure and **b)** density of states for 0.52Ce-0.39Er-HAp.

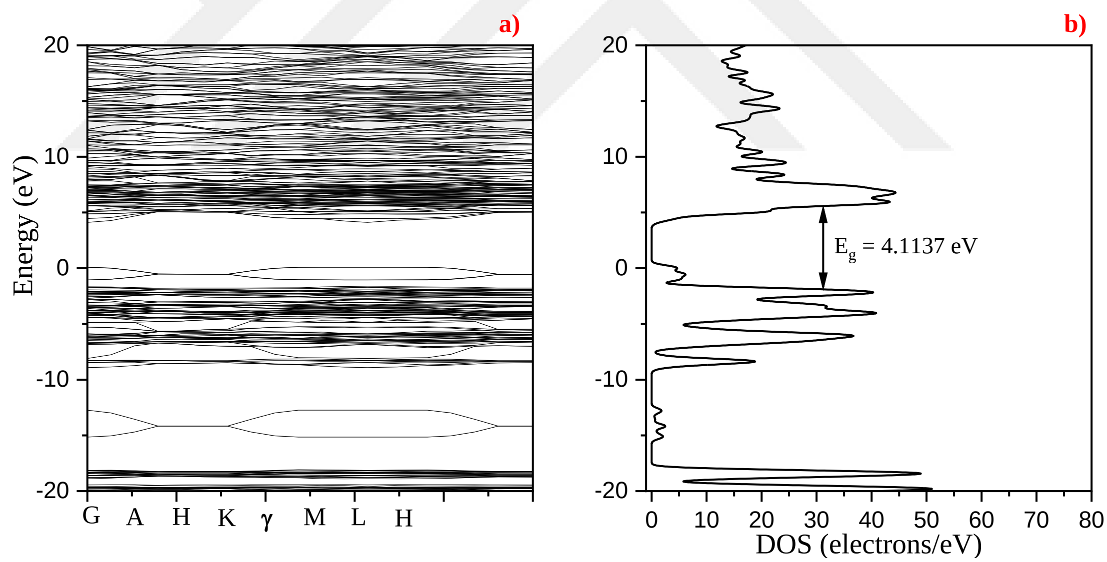

Figure 6.32. a) Band structure and **b)** density of states for 0.65Ce-0.39Er-HAp.

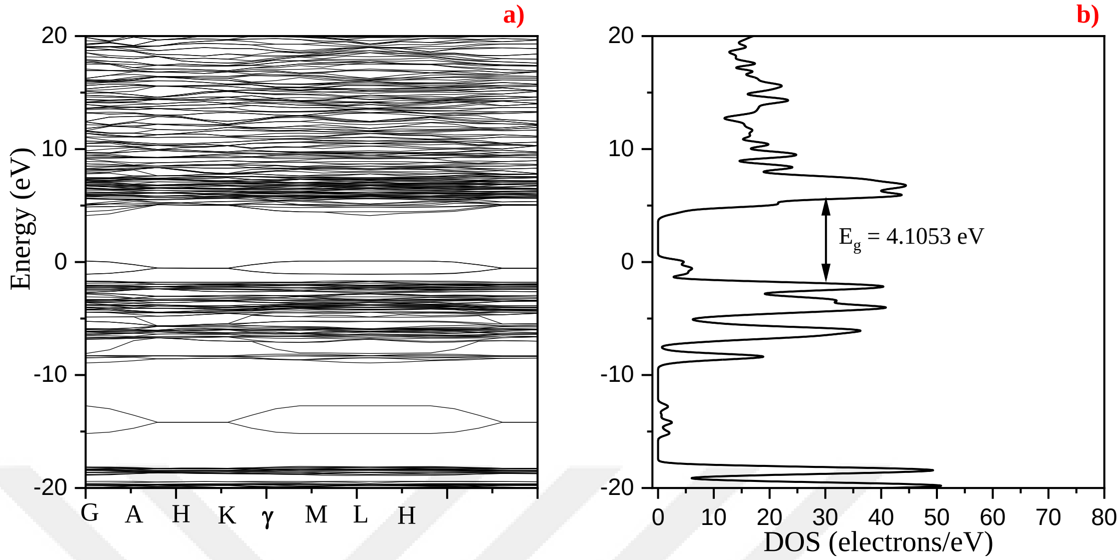

Figure 6.33. a) Band structure and **b)** density of states for 0.78Ce-0.39Er-HAp.

6.2.2.2 Density and Linear Absorption Coefficient of Er/Ce co-doped HAps

The density values were calculated to be 3.1745, 3.1786, 3.1827, 3.1868, 3.1909, and 3.1950 g cm^{-3} for 0.13Ce-0.39Er-HAp, 0.26Ce-0.39Er-HAp, 0.39Ce-0.39Er-HAp, 0.52Ce-0.39Er-HAp, 0.65Ce-0.39Er-HAp, and 0.78Ce-0.39Er-HAp, respectively. Ce (6.77 g cm^{-3}) and Er (9.07 g cm^{-3}) have densities that are higher than that of Ca (1.55 g cm^{-3}) [251]. The addition of Ce raised the density of the HAp system since the amount of Er was kept constant. In brief, the higher the Ce content results the higher the density.

For each sample, Figure 6.34 displays the LAC as a function of photon energy. All structures cause a decline as photon energy increases. Furthermore, the LAC value rises in lockstep with the amount of Ce present. The prepared samples here in this work were found to be suitable candidates for radiation shielding and medical applications because of their weakening properties for electromagnetic radiation, and the obtained results are in line with the literature [131, 232, 247, 249].

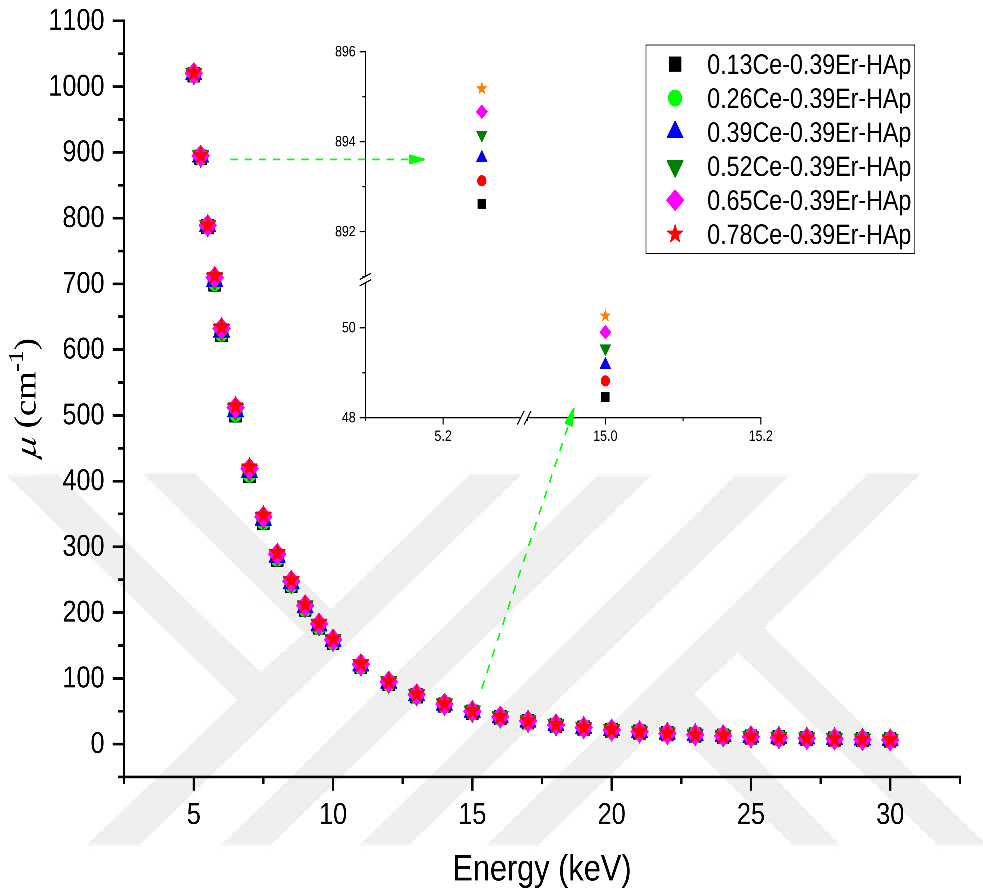

Figure 6.34. Linear absorption coefficient dependent on the energy of the HAp doped with Ce samples.

6.3 Effects of Praseodymium Doping on Erbium-Based Hydroxyapatites

6.3.1 Experimental Results of Er/Pr co-doped HAps

6.3.1.1 XRD Results of Er/Pr co-doped HAps

The XRD results of Er/Pr co-doped HAp samples are shown in Figure 6.35. According to the as-analyzed XRD patterns, HAp (JCPDS no: 09-0432) was the single phase for all the samples within the sensitivity limits of the XRD technique, and no secondary phase was found. Pr-content was shown to have a considerable impact on the amount of the mentioned phase.

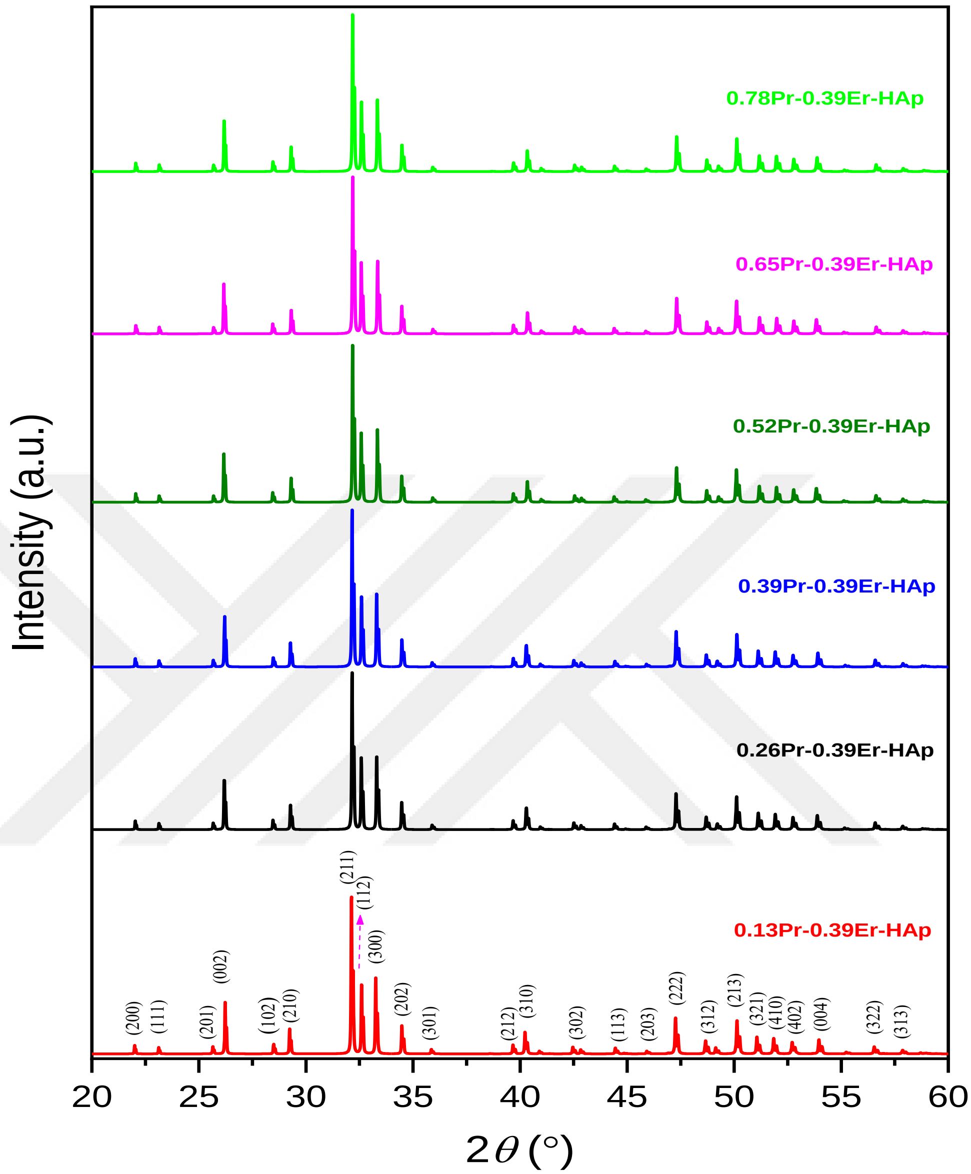

Figure 6.35. XRD patterns of the Er/Pr co-doped HAps

Table 6.8 presents findings from theoretical and experimental calculations of various parameters. According to the theoretical results, there is no gradual decrease in the values of lattice parameters *a* and *c*, but a gradual change is observed in the value of *V*. In contrast, the experimental data reveals non-gradual changes in all three parameters, *a*, *c*, and *V*. The inclusion of Pr in the Er-HAp structure causes a noteworthy impact on all three parameters.

Table 6.8. Theoretical and experimental values of the *a*, *c*, and *V* of the Er/Pr co-doped HAps

	Theoretical			Experimental		
Samples	***a* (nm)**	***c* (nm)**	***V* (nm)^3**	***a* (nm)**	***c* (nm)**	***V* (nm)^3**
0.13Pr-0.39Er-HAp	0.93800	0.68525	0.52212	0.93245	0.67919	0.51140
0.26Pr-0.39Er-HAp	0.93529	0.68563	0.51940	0.93116	0.68011	0.51068
0.39Pr-0.39Er-HAp	0.93456	0.68522	0.51828	0.93122	0.67977	0.51049
0.52Pr-0.39Er-HAp	0.93317	0.68436	0.51609	0.93019	0.68061	0.50999
0.65Pr-0.39Er-HAp	0.93970	0.68654	0.52500	0.93001	0.68059	0.50978
0.78Pr-0.39Er-HAp	0.93556	0.68636	0.52025	0.93022	0.68024	0.50974

Table 6.9 shows the calculated crystallinity percent values for all of the samples. The addition of Pr to the Er-HAp generates variations in crystallinity, with X_C % values ranging from 89.5 % to 84.1 % for all samples.

The D_{WH} for the samples could be measured from the $\beta\cos\theta$ vs. $4\sin\theta$ as in Figure 6.36a. The ε parameter was also determined. As can be observed from the data in Table 6.9, the amount of Pr affects crystallite size. The D_S value and the D_{WH} values both showed non-gradual changes. The ε values are both negative and positive, according to the results. The compressive strain is represented by the negative values [252].

The Young's modulus plots indicated in Figure 6.36b, the σ has been calculated. Tensile and compressive stresses cause positive and negative values [253].

The u values have been determined from the $\beta cos\theta$ vs. $2^{5/2}\sin\theta\, E^{-1/2}$ plot that is represented in Figure 6.36c. Except for the 0.13Pr-0.39Er-HAp, which is less than 12 kJ m^{-3}, all of the as-estimated u values in Table 6.9 are greater than the reported value of 12 kJ m^{-3} for the un-doped HAp [238].

Table 6.9. The computed values of the crystallinity percent, crystallite size, lattice strain, stress, and anisotropic energy density of the Er/Pr co-doped HAps

Samples	X_C%	D_S (nm)	D_{WH} (nm)	$\varepsilon\times10^{-4}$	σ (MPa)	u (kJ m^{-3})
0.13Pr-0.39Er-HAp	89.50	35.90	32.47	-3.189	68.240	8.537
0.26Pr-0.39Er-HAp	87.47	33.20	26.82	-7.453	46.073	26.277
0.39Pr-0.39Er-HAp	87.07	38.81	41.64	2.183	-52.544	20.356
0.52Pr-0.39Er-HAp	86.18	37.42	37.37	0.543	52.396	24.743

0.65Pr-0.39Er-HAp	84.86	36.81	42.02	4.212	20.867	39.531
0.78Pr-0.39Er-HAp	84.09	33.22	22.77	-14.400	49.985	147.474

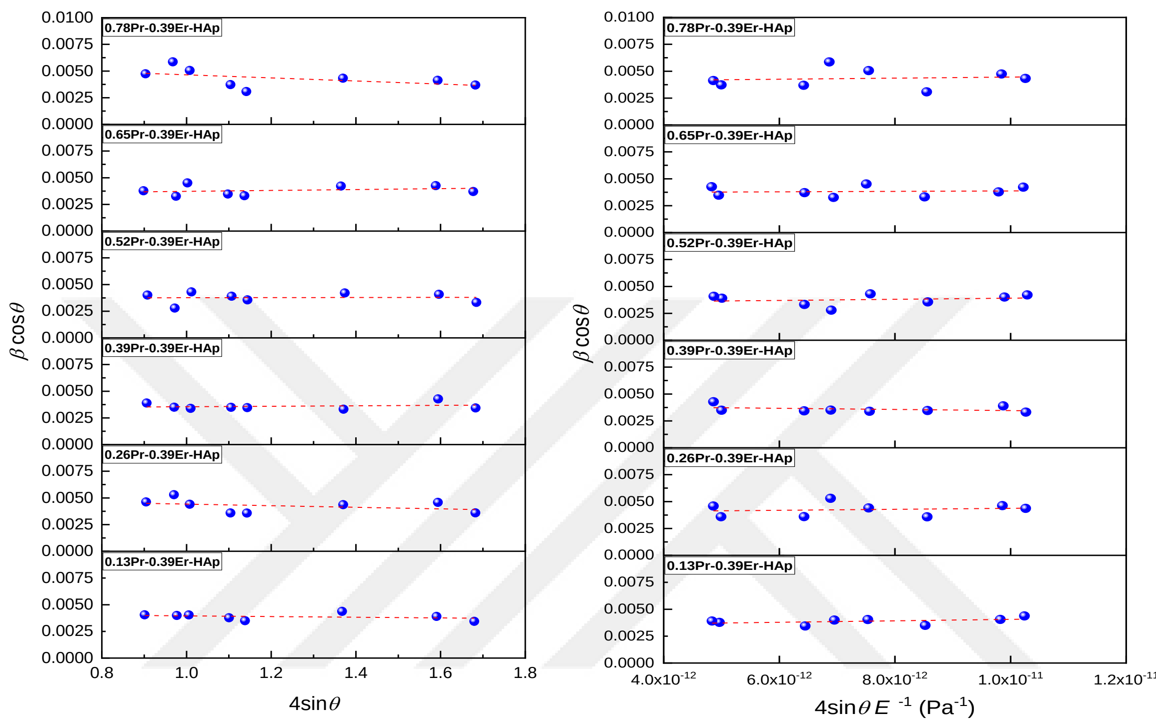

(a) (b)

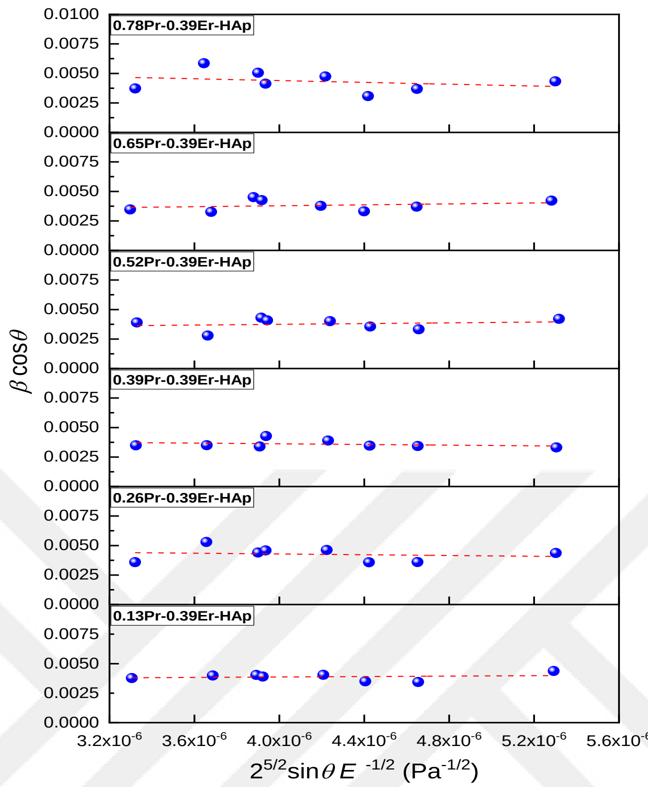

(c)

Figure 6.36. (a) The *βcosθ* vs. *4 sinθ*, **(b)** *βcosθ* vs. *4 sinθ* E^{-1}, and **(c)** *βcosθ* vs. $2^{5/2}$ *sinθ* $E^{-1/2}$ plots of the Er-based HAps doped with Pr

6.3.1.2 FTIR and Raman Spectroscopy of Er/Pr co-doped HAps

Figure 6.37 displays FTIR plots of HAp compounds. Both phosphate and hydroxyl bands were found. The vibration modes of the phosphate group are associated with the bands at wavenumber positions 466, 561, 594, 957, and 1018 cm^{-1} [239, 240]. The vibration mode of the hydroxyl group is correlated to the bands found at 636 and 3569 cm^{-1} [241, 242]. For each sample, all of the as-detected bands verify the formation of the HAp structure [243].

The Raman spectra of the samples were obtained in the range of 100 to 4000 cm^{-1}, as shown in Figure 6.38. Phosphate group-related bands were found at 438 (symmetric O-P-O bending mode), 596 (antisymmetric O-P-O bending mode), 977 (symmetric P-O stretching mode), 1024 (asymmetric P-O stretching mode), and 1092 cm^{-1} (asymmetric P-O stretching mode). The band associated with the hydroxyl group's stretching mode was seen at 3642 cm^{-1}.

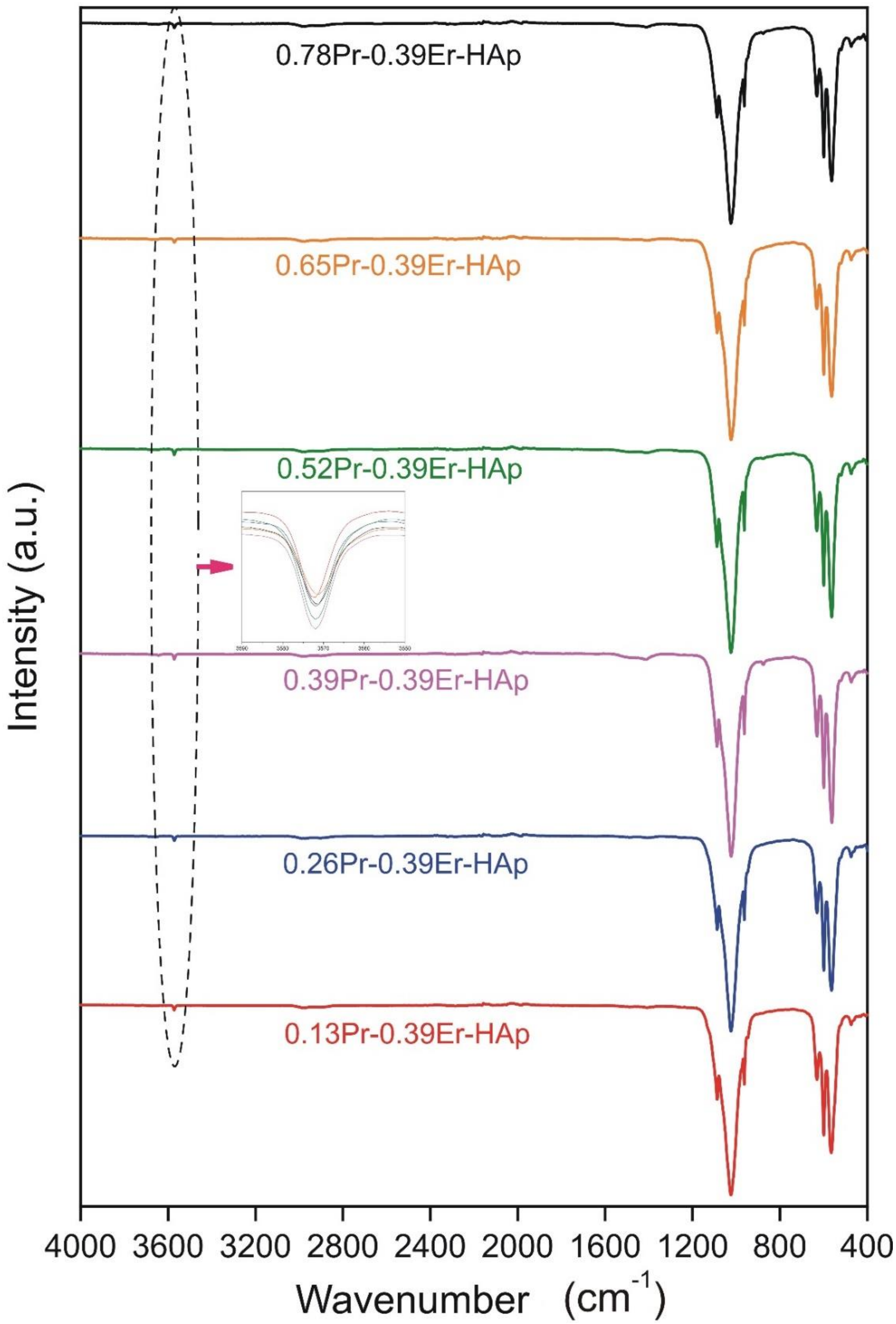

Figure 6.37. FTIR results of the Er/Pr co-doped HAps

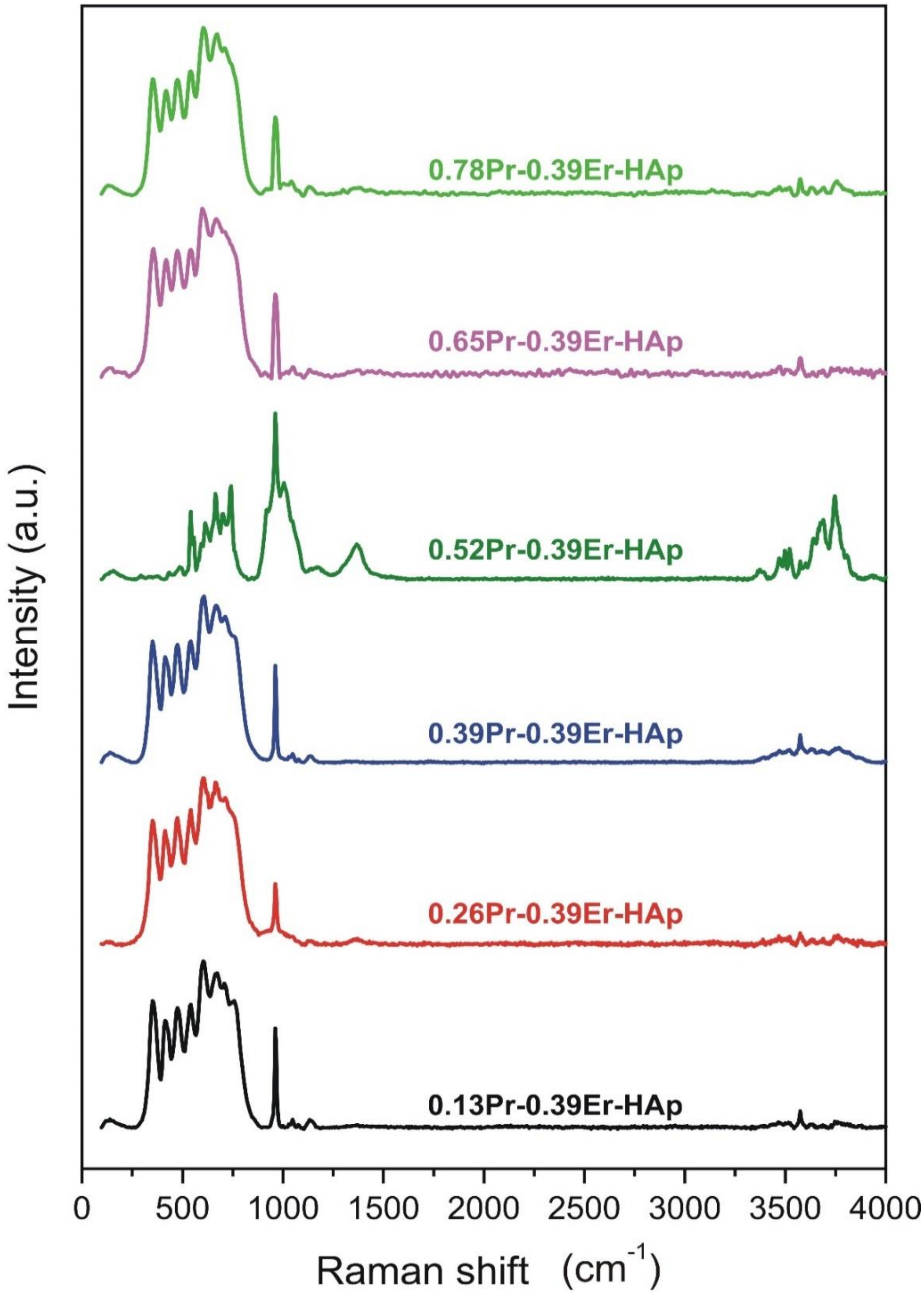

Figure 6.38. Raman spectra results of the Er/Pr co-doped HAps

6.3.1.3 Morphological Investigations of Er/Pr co-doped HAps

SEM images and EDX findings of the co-doped HAps in their original state are displayed in Figure 6.39. All of the samples are composed of sphere-shaped stacked nanoparticles. The EDX figures confirm the addition of Er and Pr to the HAp structure. The as-detected Pr content increases with the addition of Pr, as predicted, although Pr introduction into the apatitic structure is restricted. As a result, the greater levels of the Pr dopant could be attributed to its deposition on the HAp surface. The values of the stoichiometric ratios Ca/P and (Ca+Er+Pr)/P are compared between experimental and theoretical data in Table 6.10. These data are quite compatible.

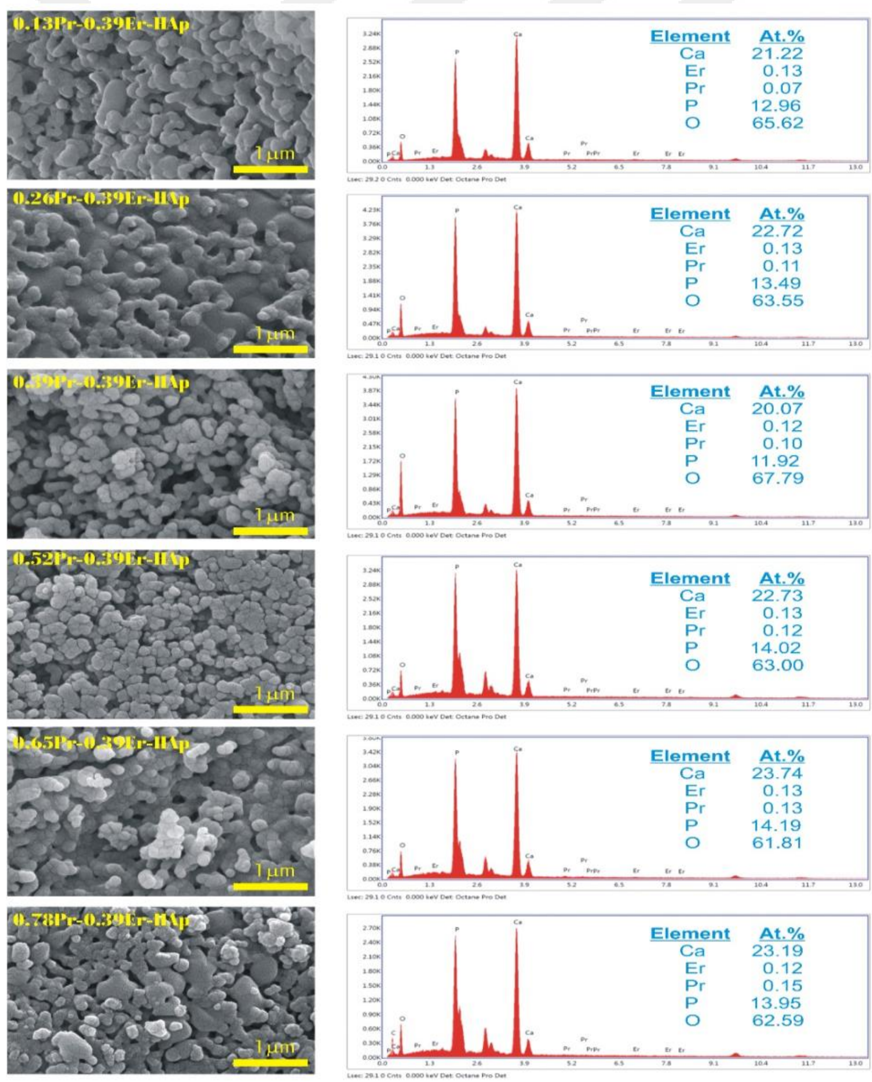

Figure 6.39. SEM pictures and EDX results of the Er/Pr co-doped HAps

Table 6.10. Theoretical and experimental values of the Ca/P and (Ca+Er+Y)/P ratios of the Er/Pr co-doped HAps.

Samples	Ca/P (Theo.)	Ca/P (Exp.)	(Ca+Er+Pr)/P (Theo.)	(Ca+Er+Pr)/P (Exp.)
0.13Pr-0.39Er-HAp	1. 6580	1.6373	1. 6667	1. 6528
0.26Pr-0.39Er-HAp	1.6558	1.6842	1.6667	1.7020
0.39Pr-0.39Er-HAp	1.6537	1. 6837	1.6667	1. 7022
0.52Pr-0.39Er-HAp	1.6515	1.6189	1.6667	1.6391
0.65Pr-0.39Er-HAp	1.6493	1.6730	1.6667	1.6913
0.78Pr-0.39Er-HAp	1. 6472	1.6624	1.6667	1.6817

6.3.1.4 Thermal Analysis Results of Er/Pr co-doped HAps

DTA and TGA thermograms of HAp samples that are co-doped with Er and Pr are shown in Figures 6.40 and 6.41 respectively. The DTA thermograms in Figure 6.40 shows that samples are thermally stable between room temperature and 900 °C since there is no peak corresponding to the disintegration of the HAp structure, and these results are remarkably comparable to those described by *Ali et al. [112]*. Among all the samples, the one with the highest Pr-content is the most stable. The thermal stability of Er-doped HAps can be improved and controlled by Pr content, according to the results.

There are no mass losses in the samples from room temperature to 900 °C, as shown by the TGA results in Figure 6.41. In this temperature range, total mass losses for 0.13Pr-0.39Er-HAp, 0.26Pr-0.39Er-HAp, 0.39Pr-0.39Er-HAp, 0.52Pr-0.39Er-HAp, 0.65Pr-0.39Er-HAp, and 0.78Pr-0.39Er-HAp were 0.29, 0.44, 1.70, 0.78, 0.45, and 0.46%, respectively. The loss of adsorbed (from room temperature to 200 °C) and lattice water (between 200 °C and 400 °C) water in the samples can be related to these losses [244, 245]. The dehydroxylation of the HAp samples is responsible for the remaining mass losses for all samples at temperatures above 400 °C [242]. These mass losses could be seen more clearly after 600 °C in the current work, and they are in good agreement with the literature [246]. Dehydroxylation is supported by a reduction in the intensity of the band 3571 cm^{-1} in the FTIR plots presented in Figure 6.37.

Figure 6.42 shows the plots of specific heat capacity (Cp) vs. temperature for all of the samples. The specific heat capacity of a substance is one of the most essential thermodynamic properties. As shown in Fig. 42, rising temperature and Pr quantity alter this parameter.

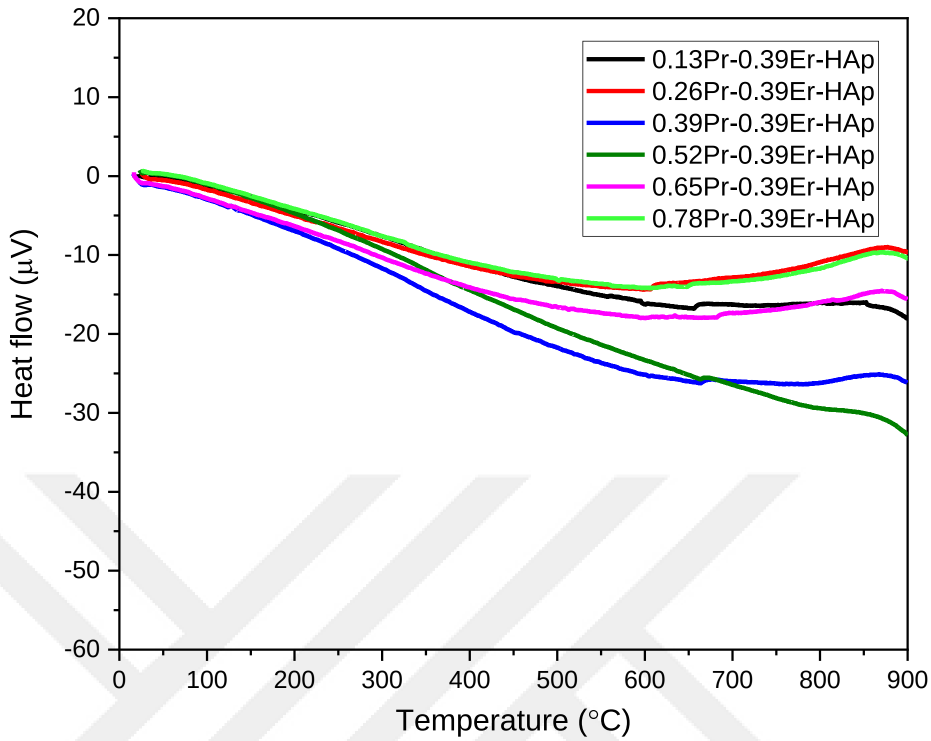

Figure 6.40. DTA curves of all the samples of the Er/Pr co-doped HAps

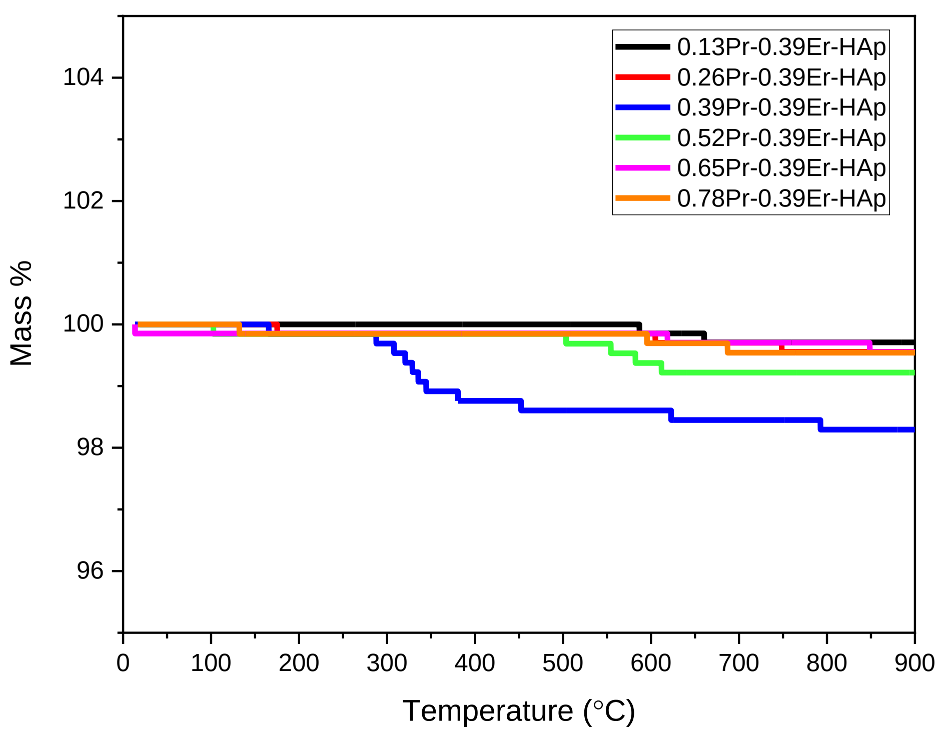

Figure 6.41. TGA thermograms of the Er/Pr co-doped HAps

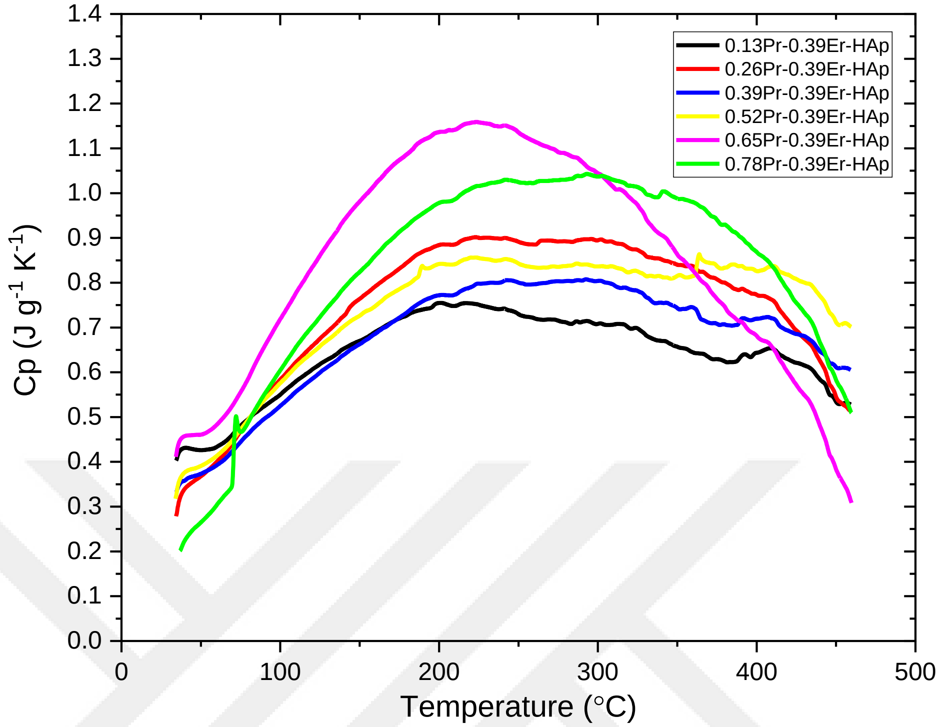

Figure 6.42. The C_p vs. temperature plots of the Er/Pr co-doped HAps.

6.3.1.5 *In Vitro* Biocompatibility Results of Er/Pr co-doped HAps

Cell viability result has been given in Table 6.11 and Figure 6.43. The optic microscope images are also illustrated in Figure 6.44. The results indicated Pr/Er-HAp samples exhibited high cell viability levels in the range of 83.31% to 91.26%. The biocompatibility of the samples decreases for all Pr/Er-HAp samples, but their cell viabilities remain over 80%, which is indicated that all the Pr/Er co-doped samples have acceptable biocompatibility.

Table 6.11. Cell viability level of L-929 cell exposed Pr/Er-HAp samples

Sample	Cell Viability (%)	Std. Dev.
Control	100.00	3.42
0.13Pr-0.39Er-HAp	87.86	9.85
0.26Pr -0.39Er-HAp	83.31	7.79
0.39Pr -0.39Er-HAp	84.88	7.89
0.52Pr -0.39Er-HAp	86.99	9.59
0.65Pr -0.39Er-HAp	89.09	7.89

0.78Pr -0.39Er-HAp	91.26	5.89

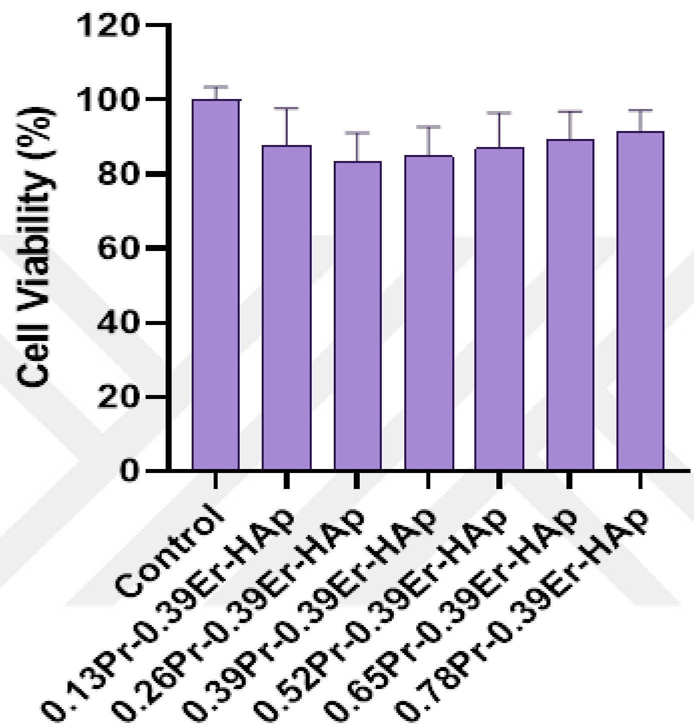

Figure 6.43. Cell viability level of L-929 cell exposed Pr/Er-HAp samples

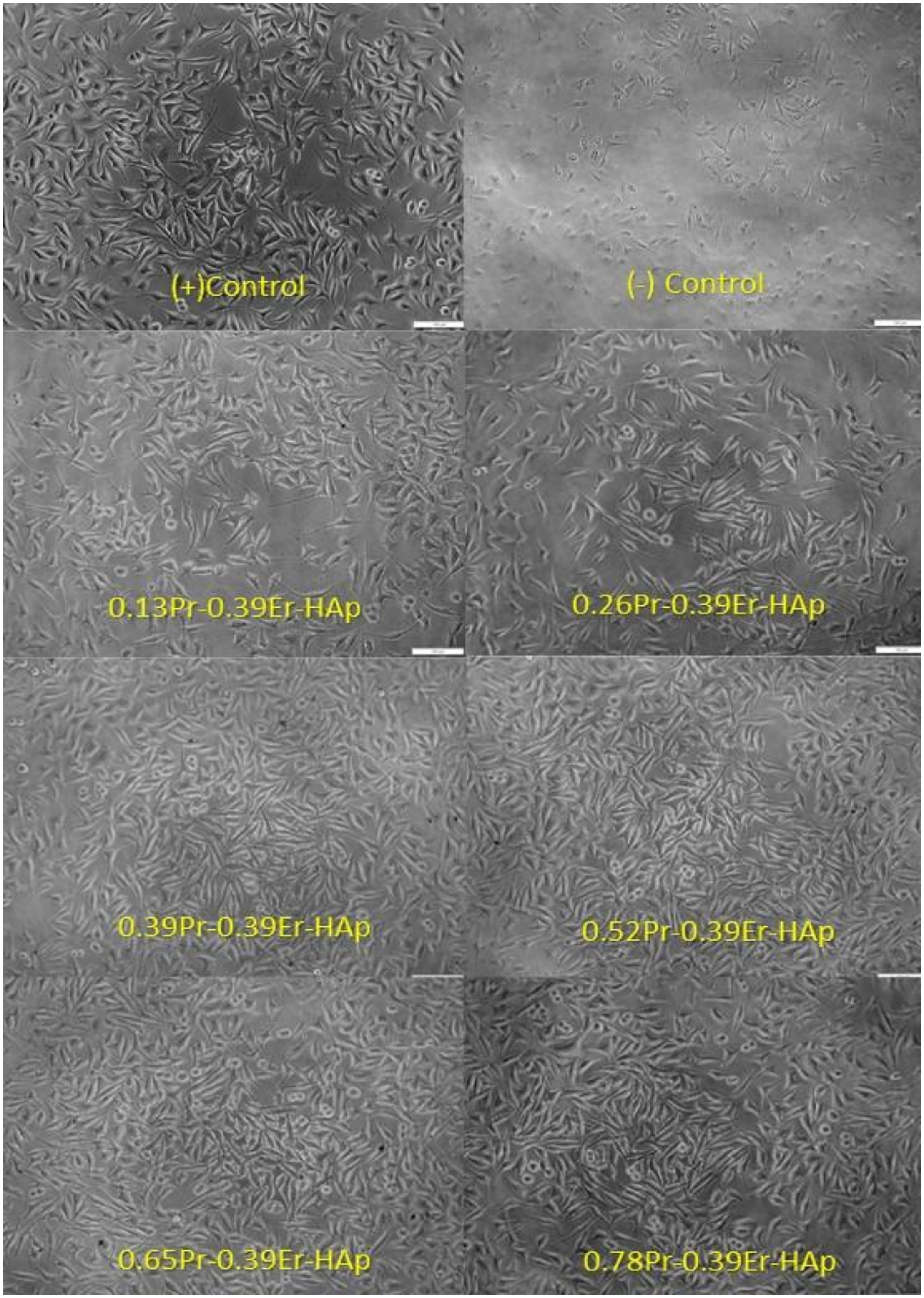

Figure 6.44. Optic microscope photos of the L-929 cell exposed Pr/Er-HAp samples

6.3.2 Theoretical Results of Er/Pr co-doped HAps

6.3.2.1 Bandgap and Density of States Calculations of Er/Pr co-doped HAps

Origin Lab was utilized in combination with a density functional theory (DFT) tool for carrying out band structure and density of state computations [254]. Figure 6.45a-f depicts the computed density of states (DOS) and band structures (BS) of multiple synthesized Erbium (Er)-based HAp samples, wherein Praseodymium (Pr) is doped at different atomic percentages, including 0.13Pr-0.39Er-HAp, 0.26Pr-0.39Er-HAp, 0.39Pr-0.39Er-HAp, 0.52Pr-0.39Er-HAp, 0.65Pr-0.39Er-HAp, and 0.78Pr-0.39Er-HAp.

In all figures, the band gaps have been calculated in the range of (G-H). The electron configuration of Erbium (Er) is [Xe] $4f^{12}6s^{2}$. The remaining electrons of the Er atom form highly cohesive bands due to the closed-shell atomic levels present in the Xenon configuration. Because the 6s orbital is relatively smaller and close to constraint, the 4f level splits more than the 6s level. The region of the image with the highest DOS corresponds to the contribution of the f orbital to the bands, which is more dominant at positive energies and even at negative energies. It's also reasonable to expect s orbitals to have a minor role in the DOS structure. By adding Pr atoms in varied proportions, the molecule's energy gap was decreased to 4.0618 eV from 4.1739 eV. The electron configuration of Praseodymium (Pr) is [Xe] $4f^{3}6s^{2}$.

By combining with Praseodymium and other atoms in the HAp molecule, the device's energy gap decreases as a result of the higher energy level. When energy levels increase, greater splitting typically occurs. Figure 6.45a-f illustrates that incorporating the Pr atom into the doped HAp molecule leads to a higher energy contribution to the energy gap. The energy bandgap values decrease as Pr is added to the Er-based HAp structure, as demonstrated in the figures.

In previous work in literature, it was also found that increasing amounts of the as-used dopants of Er^{3+} [247], Pr^{3+} [22], Sm^{3+} [255], Tb^{3+} [256], and Ti^{4+} [257] have a similar propensity to lower bandgap levels. In this regard, the current research agrees with earlier research in a very significant way. With the addition of Pr to the Er-based HAp structure, the bandgap values gradually drop. The decrease in bandgap energy can be connected to electronic states within symmetry lines, which may change due to doping and impact the bandgap value.

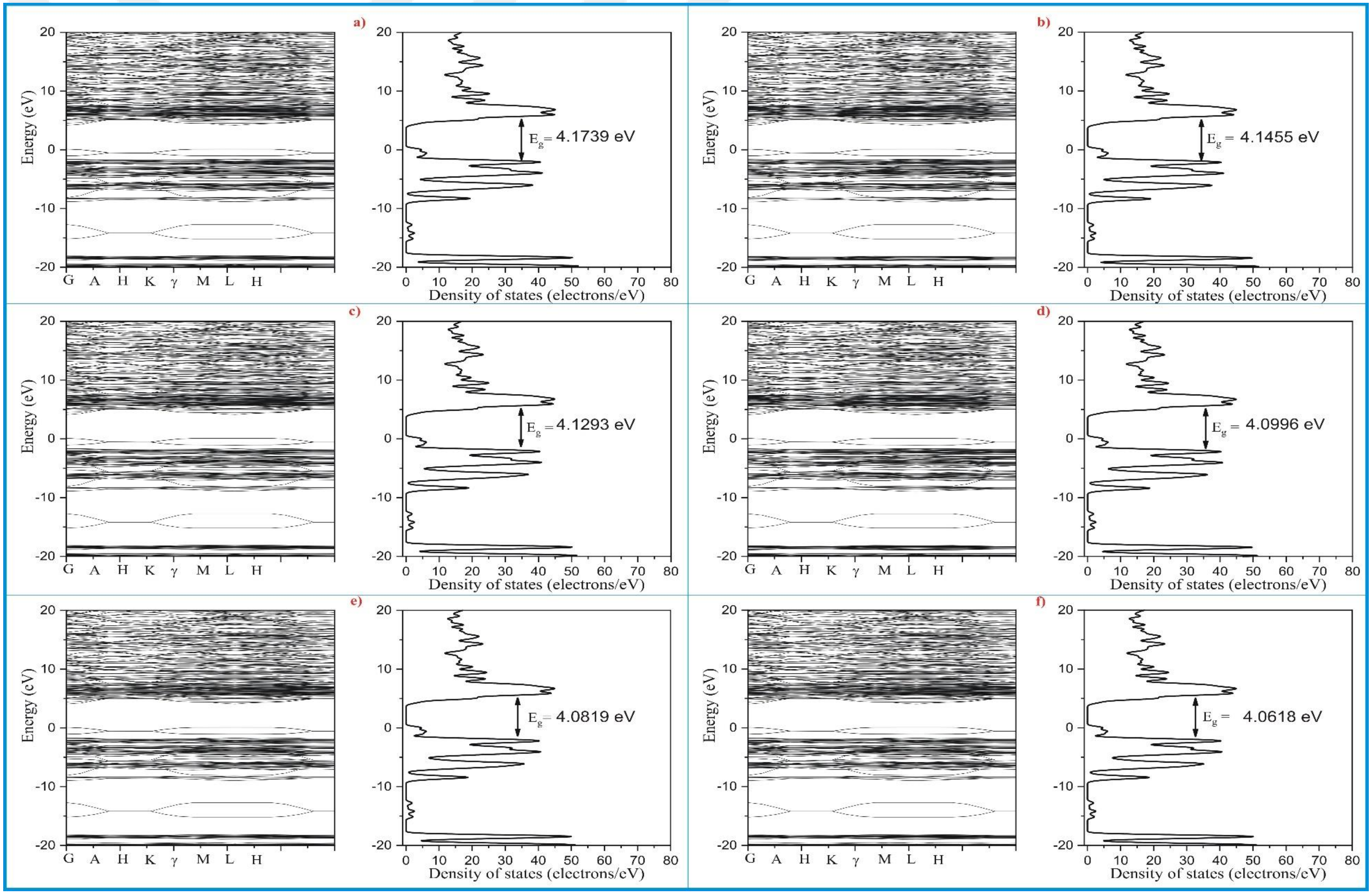

Figure 6.45. The BS and DOS of the **a)** 0.13Pr0.39Er/HAp, **b)** 0.26Pr-0.39Er-HAp, **c)** 0.39Pr-0.39Er-HAp, **d)** 0.52Pr-0.39Er-HAp, **e)** 65Pr-0.39Er-HAp and **f)** 0.78Pr-0.39Er-HAp structures.

6.3.2.2 Density and Linear Absorption Coefficient of Er/Pr co-doped HAps

For 0.13Pr-0.39Er-HAp, 0.26Pr-0.39Er-HAp, 0.39Pr-0.39Er-HAp, 0.52Pr-0.39Er-HAp, 0.65Pr-0.39Er-HAp, and 0.78Pr-0.39Er-HAp, the density values were calculated to be 3.154, 3.161, 3.168, 3.173, and 3.179 g cm^{-3}, respectively. The densities of Pr (6.77 g cm^{-3}) and Er (9.07 g cm^{-3}) are greater than that of Ca (1.54 g cm^{-3}) [258]. The density of the HAp system was improved by the addition of Pr because the amount of Er was kept constant.

The graph depicted in Figure 6.46 illustrates how the linear absorption coefficient (LAC) changes depending on the photon energy for each of the doped structures. In all structures, a decline in LAC occurs as the photon energy increases. Additionally, as the quantity of Pr increases, the LAC value increases gradually. This reduction in the ability to absorb electromagnetic radiation implies that all the samples have potential as effective options for radiation shielding and medical applications [131, 247, 249].

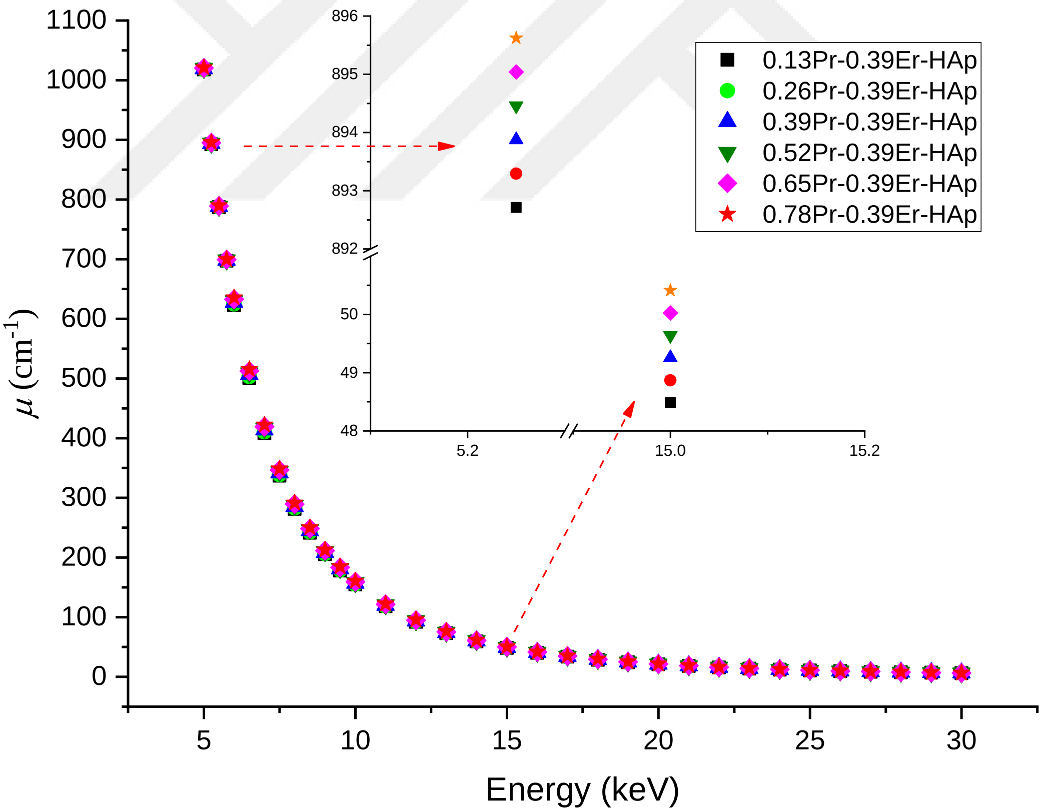

Figure 6.46. The LACdependence on the energy and composition of the Er/Pr co-doped HAps

6.4 Quantum Chemical Study of Some Basic Organic Compounds as the Corrosion Inhibitors

6.4.1 Structure Optimization

The gas-phase geometry optimizations of all the structures (M1-10) were investigated by B3LYP (Fig. 6.47). Using 6-31G(d,p) basis set.

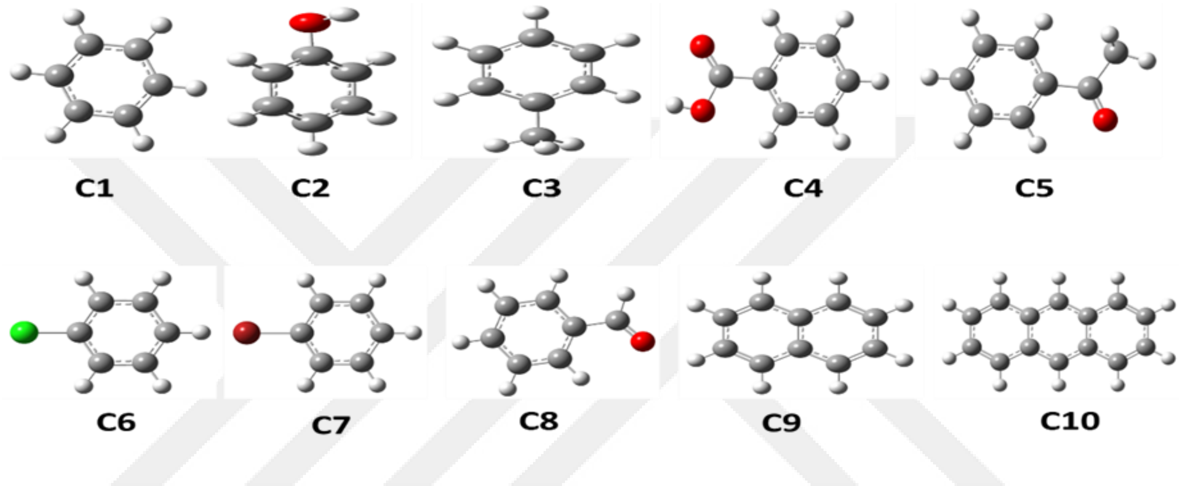

Figure 6.47. Geometrical optimization for basic organic compounds by Gaussian program.

6.4.2 Inhibitor Parameters

From the molecule's electronic structure, electronic structure identifiers were developed and connected to the electronic structure [259]. The consistent electronic structural parameters, which contain E_{HOMO}, E_{LUMO}, ΔE gap, σ, χ, Pi, σ, χ, ε, μ. The HOMO, LUMO, and μ data were resulting from the Gaussian outturn of the molecular profile. Other parameters can be calculated using the equations that are already present in the literature. E_{HOMO} and E_{LUMO} are the highest occupied and lowest unoccupied energy levels, respectively, and their values determine a material's reactivity or passivity. The ionization energy and electron affinity values of any chemical type are connected to its E_{HOMO} and E_{LUMO} values, according to Koopman's theorem. [260, 261]. The parameters ΔE [262], η, σ [263], χ, and Pi [264] are calculated according to the following equations:

$I = -E_{HOMO}$, $A = -E_{LUMO}$, $\Delta E = (E_{LUMO} - E_{HOMO})$, $\eta = (I - A) / 2$, $\sigma = I/\eta$, $\chi = (I + A) / 2$, $Pi = -\chi$, $\omega = Pi^2/2\eta$ and $\varepsilon = Pi * \eta$

The energy loss caused by the overall electron flow between the transmitter and the receiver is measured by the electrophilicity index (ω. The nucleophilicity index (ε) is a new chemical structure identifier. The following equation is used to determine how many electrons were transported between the inhibitor and the metal surface [205].

$$\Delta N = \frac{\chi metal - \chi inhibitor}{2.(\eta metal - \eta inhibitor)}$$

The value of χ and η for the compound are calculated theoretically using DFT/B3LYP level with a 6-311G(d, p) basis set, while experimentally values for χ metal and η metal were found from the literature [265] which was calculated by Pearson. According to Pearson, an individual metal's electron affinity (A) and ionization potential (I) are considered to be equal (I = A), and η for a single metal value is assumed to be zero. Table 6.12 shows the electronic structural characteristics and total energy for the mentioned molecules. From Table 6.12 the HOMO and LUMO energies appear that they have a general tendency among them. HOMO is important for corrosion studies because it is related to electron-donating capacity. As HOMO values rise, the inhibitory effect of inhibitor molecules also rises [266]. It, therefore, has an impact on the way charges are transferred over the metal surface, causing adsorption. The E_{HOMO} ordered as follows:

C10>C9>C3>C2>C7>C6>C1>C5>C8>C4

According to the high EHOMO value, compound C10 has the highest inhibitory activity, and compound C4 has the lowest inhibitory activity (Fig. 6.48). LUMO refers to the ability to accept electrons. Low E_{LUMO} values suggest that the inhibitor can apply a negative charge to the metal surface. The E_{LUMO} ordered as shown below:

C2>C1>C3>C6>C7>C9>C4>C5>C10>C8

According to the E_{LUMO} sequence, the LUMO energy of C10 has the lowest energy and the LUMO energy of C2 has the highest energy. According to the results, the C10 inhibitor reacted by working as a donor, and its inhibitor activity was therefore high. The C4 inhibitor has the lowest E_{LUMO} and lowest E_{HOMO} values. While low E_{HOMO} inhibitors reduce metal reactivity, the metal inhibitor acts as a donor to the inhibitor. As a result, the inhibitor's activity decreases while the metal's reactivity increases. According to HOMO-LUMO energies, the C10 molecule provides the best corrosion inhibition (Figure 6.48).

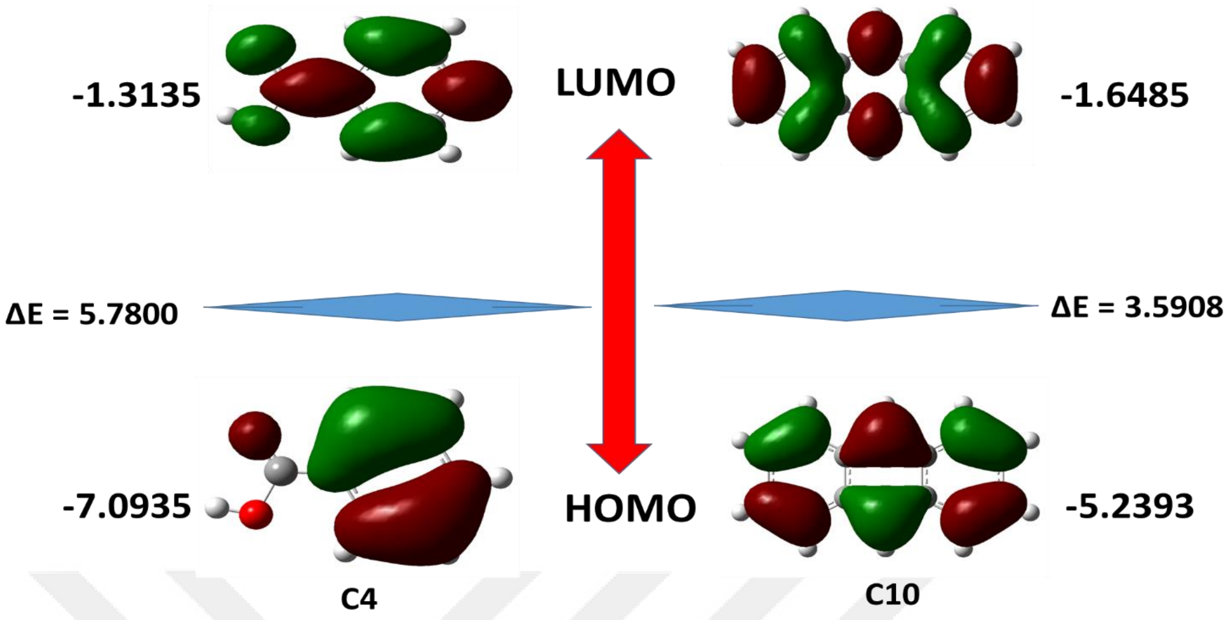

Figure 6.48. HOMO & LUMO energy levels for both Benzoic acid (C4), and Anthracene (C10).

The energy difference between E_{HOMO} and E_{LUMO} has a considerable impact on theoretical inhibition efficiency and also static molecular reactivity. The sequence of the inhibitors was shown as follows based on the energy gap value:

C10>C9>C8>C5>C4>C7>C3>C6>C2>C1

The energy bandgap indicates the molecule's activity. For inhibitor studies, it is critical to compare ΔE. The lower value of the energy bandgap results in better inhibition efficiency. The lower ΔE value in corrosion inhibitors is determined by the E_{HOMO} rather than the E_{LUMO}. Anti-corrosion agents can be made from inhibitor derivatives with high HOMO energy and low ΔE [266]. C10 will provide good inhibitory activity based on the maximum HOMO energy value given the above E_{HOMO} and E sequence.

Table 6.12. The electron structure identifiers were calculated using the 6–31(d,p) basis of molecules in the gas phase at the DFT/B3LYP theory level.

Parameters	Equations	Benzene	Phenol	Toluene	Benzoic Acid	Aceto phenone	Chloro benzene	Bromo benzene	Benzaldehyde	Naphthalene	Anthracene
Total Energy (a.u)		-232.2582	-307.4722	-271.5788	-420.8354	-384.9082	-691.8529	-2803.3617	-345.5827	-425.0630	-617.8310
μ (D)		0.0000	1.5635	0.3423	1.9154	2.9830	1.9180	1.8099	3.2818	0.0000	0.0015
E_{LUMO} (eV)		-0.0729	-0.0188	-0.1222	-1.3135	-1.4809	-0.3646	-0.3655	-1.7260	-0.9793	-1.6485
E_{HOMO} (eV)		-6.7194	-6.4794	-6.4121	-7.0935	-6.7259	-6.7139	-6.5901	-6.9447	-5.8026	-5.2393
ΔE (eV)		6.6464	6.4606	6.2900	5.7800	5.2450	6.3493	6.2247	5.2186	4.8233	3.5908
I (eV)	**$I = -E_{HOMO}$**	6.7194	6.4794	6.4121	7.0935	6.7259	6.7139	6.5901	6.9447	5.8026	5.2393
A (eV)	**$A = -E_{LUMO}$**	0.0729	0.0188	0.1222	1.3135	1.4809	0.3646	0.3655	1.7260	0.9793	1.6485
χ (eV)	**$\chi = (I + A) / 2$**	3.3961	3.2491	3.2672	4.2035	4.1034	3.5393	3.4778	4.3354	3.3910	3.4439
η (eV)	**$\eta = (I – A) / 2$**	3.3232	3.2303	3.1450	2.8900	2.6225	3.1746	3.1123	2.6093	2.4116	1.7954
σ (eV)	**$\sigma = 1/\eta$**	0.3009	0.3096	0.3180	0.3460	0.3813	0.3150	0.3213	0.3832	0.4147	0.5570
Pi (eV)	**$Pi = -\chi$**	-3.3961	-3.2491	-3.2672	-4.2035	-4.1034	-3.5393	-3.4778	-4.3354	-3.3910	-3.4439
ω (eV)	**ω = Pi2/2η**	1.7353	1.6340	1.6970	3.0570	3.2102	1.9729	1.9431	3.6016	2.3840	3.3030
ε (eV)	**ε = Pi. η**	-11.2861	-10.4954	-10.2752	-12.1482	-10.7612	-11.2359	-10.8240	-11.3123	-8.1778	-6.1833
ΔN	**ΔN = (χmetal - χinhibitor) / 2. (ηmetal - ηinhibitor)**	0.5422	0.5806	0.5935	0.4838	0.5523	0.5451	0.5659	0.5106	0.7483	0.9903

Table 6.13 shows the atomic charge distributions on the inhibitor's molecular structure. Mulliken population analysis is a prominent approach for estimating inhibitor molecule adsorption regions (Table 6.13). Many researchers agreed that the presence of negatively charged heteroatoms enhances the capacity of the donor-acceptor mechanism to adsorb on the metal surface [267]. As the result, the negatively charged in the center of the aromatic ring, C10 has an effective inhibitory effect. As observed in Figure 6.49 MEP map, the aromatic ring exhibits a denser red color. This can be regarded as the C10 inhibitor being attached to the metal surface coordinately from these regions.

Table 6.13. Charge distribution on the atoms for the molecules.

Benzene	Phenol	Toluene	Benzoic Acid	Aceto phenone	Chloro benzene	Bromo benzene	Benzaldehyde	Naphthalene	Anthracene
1 C -0.083921	1 C -0.083078	1 C -0.087315	1 C -0.072757	1 C -0.074040	1 C -0.076274	1 C -0.084742	1 C -0.073778	1 C -0.092621	1 C -0.097884
2 C -0.083817	2 C -0.091047	2 C -0.084628	2 C -0.090006	2 C -0.091860	2 C -0.086499	2 C -0.078863	2 C -0.088063	2 C -0.128589	2 C -0.120643
3 C -0.083900	3 C -0.093222	3 C -0.113161	3 C -0.103092	3 C -0.117941	3 C -0.076274	3 C -0.091510	3 C -0.113867	3 C 0.101945	3 C 0.110050
4 C -0.083921	4 C 0.285433	4 C 0.102704	4 C 0.049768	4 C 0.051136	4 C -0.074744	4 C 0.055669	4 C 0.036810	4 C 0.102287	4 C 0.110043
5 C -0.083817	5 C -0.093222	5 C -0.113161	5 C -0.097000	5 C -0.095878	5 C -0.089429	5 C -0.091510	5 C -0.093975	5 C -0.128295	5 C -0.120666
6 C -0.083900	6 C -0.091047	6 C -0.084628	6 C -0.089414	6 C -0.087567	6 C -0.074744	6 C -0.078863	6 C -0.085367	6 C -0.092980	6 C -0.097881
	12 O -0.595143	12 C -0.374314	12 C 0.546772	12 C 0.375292	12 Cl -0.020699	12 Br -0.127018	12 C 0.257623	10 C -0.128213	7 C -0.209498
			13 O -0.531308	13 O -0.468547			14 O -0.425203	11 C -0.128707	8 C -0.209489
			15 O -0.466598	14 C -0.385007				14 C -0.092621	9 C 0.110006
								15 C -0.092937	10 C 0.110076
									11 C -0.120682
									13 C -0.097872
									14 C -0.097903
									15 C -0.120635

C: is Carbon number.

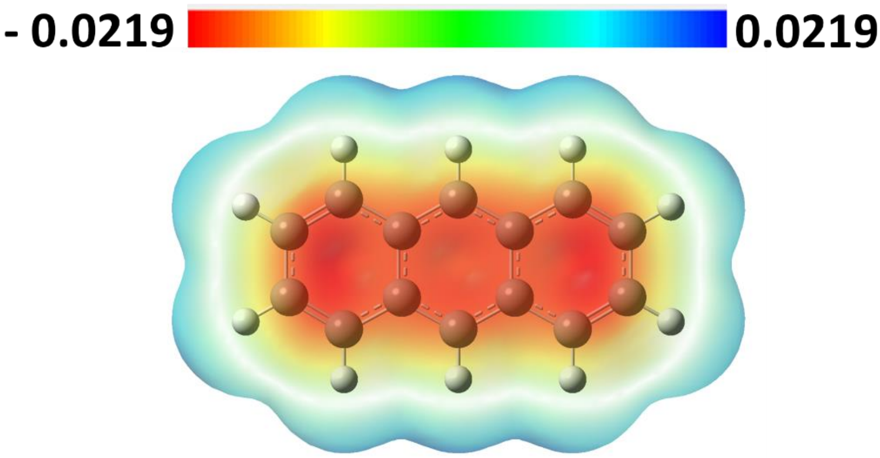

Figure 6.49. MEP map for Anthracene (C10)

The η and σ parameters are two more significant factors that offer information on the stability, reactivity, and inhibitor activity of an inhibitor. The letters η and σ of inhibitors are arranged as follows:

η C1>C2>C6>C3>C7>C4>C5>C8>C9>C10

σ C10>C9>C8>C5>C4>C7>C3>C6>C2>C1

Soft inhibitors are better at inhibiting corrosion because they are more reactive than hard inhibitors as well as the organic selected as an inhibitor serves as a Lewis base [268]. The C10 inhibitor in this situation showed high EHOMO and low E values as well as high softness and low hardness ratings. The values η and σ indicate that the C10 inhibitor has the most potent inhibitory effect.

Electronegativity (χ) and chemical potential (Pi) are two additional parameters used to calculate inhibitor activity. The coordinated covalent connection between the inhibitor and the metal is established according to the estimated inhibitor values χ [266]. The χ sequenced as follows:

C8>C4>C5>C6>C7>C10>C1>C9>C3>C2

In this research, the corrosion inhibition efficacy of molecules intended as inhibitors of iron metal were examined. Table 6.14 computed χ values for the inhibitors were determined to be less than the iron metal's experimental χ value. As a result, the iron metal will form bonds by absorbing electrons from the inhibitor compound. As can be observed in the χ sequence, the C10 and C9 inhibitors with the lowest χ value compared with another molecule will be the most effective corrosion inhibitor. The inverse of electronegativity is Pi. The molecules with high chemical potential will have high activity against other molecules, whereas the molecules with low potential will provide low activity [269]. The two most active inhibitors are C10 and C9, as seen in Table 6.12.

The important factors affecting the action of corrosion inhibitors are ω and ε indices. The ω index denotes an inhibitor molecule's ability to accept electrons. The capacity of the inhibitors to donate electrons is shown by the ε index. The inhibition activity increases as the ω or ε values decrease. The theoretical inhibition efficiency sequence in this study, according to ω and ε, is as follows:

ω C8>C9>C10>C5>C4>C6>C7>C1>C3>C2

ε C10>C9>C3>C2>C5>C7>C6>C1>C8>C4

The calculated ω value of the C10 inhibitor decreased, and the ε value increased, as shown in the sequence. Concerning the other parameters, the C10 inhibitor exhibits the greatest inhibitory effects with values for ω and ε.

Comparing the ΔN [205] values of iron and metal inhibitors, it can be shown that the C10 molecule donates higher electrons to the iron metal, providing a more potent inhibitor (Table 6.12).

The dipole moment is another parameter found in Table 6.12. However, no clear link between μ and inhibition activity has been reported in the literature. According to certain studies, the activity of molecules with higher μ values leads to better inhibition, whereas other studies claim that the inhibition effect increases with decreasing μ value. The C10 inhibitor has a low dipole moment, which is consistent with the other parameters. This can be interpreted as better metal surface coverage at low μ values.

7. CONCLUSION

- **Er-based HAps doped with Y**

Wet chemical synthesis was used to produce Er-based HAps doped with Y in a range of concentrations (0.13, 0.26, 0.39, 0.52, 0.65, and 0.78 at.%). The lattice parameters were discovered to be influenced by the Y dopant. We found significant variations in the size of the crystallites and the crystallinity %. Stress and strain were created in the lattice when the Y element has been added to an Er-based HAp. All of the examined samples had the HAp structure, according to Raman and FTIR spectroscopy. The Y concentration significantly affects how the Er-Based HAp behaves thermally. The theoretical results show that the bandgap energy of the samples reduced considerably with increasing Y concentration from 4.196 eV to 4.156 eV. None of the samples exhibited any negative impacts. Except for the sample 0.39Y-0.39Er/HAp, cell viability was lower than in the control group. As the Y concentrations rise, the linear absorption coefficient decreases. All of the samples in the series proved to be biocompatible and usable in biological applications.

- **Er-based HAps doped with Ce**

Six samples of Er-based hydroxyapatite (HAps) doped with various concentrations of Ce (0.13, 0.26, 0.39, 0.52, 0.65, and 0.78 at.%) were synthesized using the wet chemical method. The presence of the Ce dopant affected the lattice properties, leading to significant variations in crystallite size and crystallinity percentage. The addition of Ce to Er-based HAp resulted in the formation of lattice strain and stress. The confirmation of the HAp structure was achieved by analyzing Raman and FTIR spectra for each sample. All samples exhibited a nanoscale morphology. The thermal behavior of Er-based HAp was notably influenced by the concentration of Ce. Theoretical calculations revealed a reduction in the bandgap energy of the samples from 4.1591 eV to 4.1053 eV as the Ce concentration increased. The cytotoxicity tests indicated that all samples demonstrated biocompatibility and could be used in biomedical applications. Furthermore, an increase in Ce concentration led to a decrease in the linear absorption coefficient.

- **Er-based HAps doped with Pr**

HAp samples doped with both Pr and Er were successfully produced and thoroughly examined using theoretical and experimental methods. The introduction of Pr into an Er-based HAp structure was found to result in a gradual increase in density, accompanied by continuous reductions in the bandgap and linear absorption coefficient. The lattice parameters of the HAp were influenced by the presence of Pr as a dopant, leading to noticeable disparities in crystallite size and crystallinity percentage. Moreover, the inclusion of Pr in Er-based HAp induced the formation of lattice strain and stress. Raman and FTIR spectra verified the formation of the HAp structure for each sample, all of which exhibited a nano-sized morphology. The thermal behavior of Er-based HAp was significantly affected by the concentration of Pr. In terms of biocompatibility, all the prepared samples demonstrated high suitability for medical applications, as confirmed by in vitro cell viability tests, where values exceeding 80% were obtained.

- **DFT study of some basic organic compounds**

The C10 inhibitor was shown to have a strong inhibitor activity because it was reactive by acting as a donor. Anti-corrosion compounds can be made from inhibitor derivatives with high E_{HOMO} and low E. Based on the greatest value of E_{HOMO} and the E sequence, compound C10 will have strong inhibitory action. When the C10 inhibitor's Mulliken atomic charges are considered, it can be concluded that the electronegative atoms significantly influence the inhibitory activity. The HOMO centers on the negatively charged atoms allowing the inhibitor to be attached to the metal surface from these centers. The area surrounding the ring is the most active area on the MEP map. The C10 inhibitor has the most active corrosion inhibition effect, according to the computed η, σ, χ, Pi, ω, and ε parameters. With a greater ΔN value, the inhibitor will be more adsorbed to the metal surface, increasing its ability to block corrosion. Conversely, with a lower χ value for the inhibitor, the iron metal will establish bonds by absorbing electrons from the inhibitor molecule. Although a precise result about the dipole moment is not available in the literature, it may be inferred that the C10 inhibitor, which is part of the study, is better at coating the metal surface at low dipole moment levels. The computed quantum chemical parameters of the process are shown to closely correlate with the activity of organic-based corrosion inhibitors with good corrosion inhibitor performance. The researched structure may be altered using calculations, which is one of its biggest benefits. It is believed that the C10 complex will be even more efficient in inhibiting corrosion if the number of rings in other molecules is enhanced.

RECOMMENDATIONS

The following notion could be suggested for future research:

- The co-dopant concentrations can be modified.
- The samples can be synthesized using another process (for example, sol-gel, combustion, spray pyrolysis, and so on).
- Additional characterization methods include Raman spectroscopy, dielectric measurements, inductively coupled plasma (ICP) technology, and transmission electron microscopy (TEM).
- It is possible to modify the synthesis conditions.

REFERENCES

[1] Steele, B.C. (2001). Material science and engineering: The enabling technology for the commercialisation of fuel cell systems, *Journal of Materials Science*, C Vol. 36 (5), pp: 1053-1068.

[2] LeGeros, R. (1993). An introduction to bioceramics, *Advanced Series in Ceramics-Vol. 1*, C Vol. 181.

[3] Park, J.B., (2012). *Biomaterials science and engineering*, Springer Science & Business Media,

[4] Huebsch, N. and Mooney, D.J. (2009). Inspiration and application in the evolution of biomaterials, *Nature*, C Vol. 462 (7272), pp: 426-432.

[5] Ratner, B.D., Hoffman, A.S., Schoen, F.J., and Lemons, J.E., (2004). *Biomaterials science: an introduction to materials in medicine*, Elsevier,

[6] Hench, L.L. (1998). Biomaterials: a forecast for the future, *Biomaterials*, C Vol. 19 (16), pp: 1419-1423.

[7] Matassi, F., Nistri, L., Paez, D.C., and Innocenti, M. (2011). New biomaterials for bone regeneration, *Clinical cases in mineral and bone metabolism*, C Vol. 8 (1), pp: 21.

[8] Lam, M.T. and Wu, J.C. (2012). Biomaterial applications in cardiovascular tissue repair and regeneration, *Expert review of cardiovascular therapy*, C Vol. 10 (8), pp: 1039-1049.

[9] Parida, P., Behera, A., and Mishra, S.C. (2012). Classification of Biomaterials used in Medicine, Vol.

[10] Vallet-Regí, M. (2001). Ceramics for medical applications, *Journal of the Chemical Society, Dalton Transactions*, C Vol. (2), pp: 97-108.

[11] Williams, D. (1976). Biomaterials and biocompatibility, *Medical progress through technology*, C Vol. 4 (1-2), pp: 31-42.

[12] Kaygili, O., Dorozhkin, S.V., and Keser, S. (2014). Synthesis and characterization of Ce-substituted hydroxyapatite by sol–gel method, *Materials Science and Engineering: C*, C Vol. 42 78-82.

[13] Agrawal, K., Singh, G., Puri, D., and Prakash, S. (2011). Synthesis and characterization of hydroxyapatite powder by sol-gel method for biomedical application, *Journal of Minerals & Materials Characterization & Engineering*, C Vol. 10 (8), pp: 727-734.

[14] Kaygili, O., Keser, S., Kom, M., Eroksuz, Y., Dorozhkin, S.V., Ates, T., Ozercan, I.H., Tatar, C., and Yakuphanoglu, F. (2015). Strontium substituted hydroxyapatites: synthesis and determination of their structural properties, in vitro and in vivo performance, *Materials Science and Engineering: C*, C Vol. 55 538-546.

[15] Liu, Y., Hou, D., and Wang, G. (2004). A simple wet chemical synthesis and characterization of hydroxyapatite nanorods, *Materials chemistry and physics*, C Vol. 86 (1), pp: 69-73.

[16] Tite, T., Popa, A.-C., Balescu, L.M., Bogdan, I.M., Pasuk, I., Ferreira, J.M., and Stan, G.E. (2018). Cationic substitutions in hydroxyapatite: Current status of the derived biofunctional effects and their in vitro interrogation methods, *Materials*, C Vol. 11 (11), pp: 2081.

[17] Pham, V.-H., Van, H.N., Tam, P.D., and Ha, H.N.T. (2016). A novel 1540 nm light emission from erbium doped hydroxyapatite/β-tricalcium phosphate through co-precipitation method, *Materials Letters*, C Vol. 167 145-147.

[18] Ratner, B.D. and Bryant, S.J. (2004). Biomaterials: where we have been and where we are going, *Annu. Rev. Biomed. Eng.*, C Vol. 6 41-75.

[19] Buntz, B. (2011). Biomaterials and the Future of Medical Devices, *MDDI On-Line.*, *http://www. mddionline. com/blog/devicetalk/biomaterials-and-future-medical-devices*, C Vol.

[20] Rezaie, H.R., Bakhtiari, L., and Öchsner, A., (2015). *Biomaterials and their applications*, Springer,

[21] Sherin, S., Sheeja, S., Devi, R.S., Balachandran, S., Soumya, R.S., and Abraham, A. (2017). In vitro and in vivo pharmacokinetics and toxicity evaluation of curcumin incorporated titanium dioxide nanoparticles for biomedical applications, *Chemico-biological interactions*, C Vol. 275 35-46.

[22] Agid, R.S., Kaygili, O., Bulut, N., Dorozhkin, S.V., Ates, T., Koytepe, S., Ates, B., Ercan, I., İnce, T., and Mahmood, B.K. (2020). Investigation of the effects of Pr doping on the structural properties of hydroxyapatite: an experimental and theoretical study, *Journal of the Australian Ceramic Society*, C Vol. 56 (4), pp: 1501-1513.

[23] Matsushita, T., *14 - Orthopaedic applications of metallic biomaterials*, in *Metals for Biomedical Devices*, M. Niinomi, Editor 2010, Woodhead Publishing. p. 329-354.

[24] Eliaz, N. (2019). Corrosion of metallic biomaterials: a review, *Materials*, C Vol. 12 (3), pp: 407.

[25] Kulinets, I., *Biomaterials and their applications in medicine*, in *Regulatory affairs for biomaterials and medical devices*2015, Elsevier. p. 1-10.

[26] Davis, J., *Materials for Medical Devices*, 2003, ASM Handbook Series.: ASM International.

[27] Pietrzak, W.S., Sarver, D., and Verstynen, M. (1996). Bioresorbable implants—practical considerations, *Bone*, C Vol. 19 (1), pp: S109-S119.

[28] Kalirajan, C., Dukle, A., Nathanael, A.J., Oh, T.-H., and Manivasagam, G. (2021). A Critical Review on Polymeric Biomaterials for Biomedical Applications, *Polymers*, C Vol. 13 (17), pp: 3015.
[29] Hench, L.L., (1993). *An introduction to bioceramics*, World scientific,
[30] Hench, L.L. (1999). Bioactive glasses and glass-ceramics. in *Materials science forum*. Trans Tech Publ.
[31] Hench, L.L. (1991). Bioceramics: from concept to clinic, *Journal of the american ceramic society*, C Vol. 74 (7), pp: 1487-1510.
[32] Amato, S.F. and Ezzell Jr, R.M., (2014). *Regulatory affairs for biomaterials and medical devices*, Elsevier,
[33] Kaygili, O., Dorozhkin, S.V., Keser, S., and Yakuphanoglu, F. (2015). Investigation of the crystal structure, dielectrical, electrical and microstructural properties of cobalt-containing calcium orthophosphates, *Materials Science*, C Vol. 21 (2), pp: 282-287.
[34] Dorozhkin, S.V. (2010). Calcium orthophosphates as bioceramics: state of the art, *Journal of functional biomaterials*, C Vol. 1 (1), pp: 22-107.
[35] Hench, L.L. and Polak, J.M. (2002). Third-generation biomedical materials, *Science*, C Vol. 295 (5557), pp: 1014-1017.
[36] Deville, S., Chevalier, J., Fantozzi, G., Bartolomé, J.F., Requena, J.n., Moya, J.S., Torrecillas, R., and Díaz, L.A. (2003). Low-temperature ageing of zirconia-toughened alumina ceramics and its implication in biomedical implants, *Journal of the European Ceramic Society*, C Vol. 23 (15), pp: 2975-2982.
[37] Hench, L.L. (1988). Bioactive ceramics, *Annals of the New York academy of sciences*, C Vol. 523 (1), pp: 54-71.
[38] Daculsi, G., LeGeros, R., Heughebaert, M., and Barbieux, I. (1990). Formation of carbonate-apatite crystals after implantation of calcium phosphate ceramics, *Calcified tissue international*, C Vol. 46 (1), pp: 20-27.
[39] Salinas, A.J. and Vallet-Regí, M. (2013). Bioactive ceramics: from bone grafts to tissue engineering, *RSC advances*, C Vol. 3 (28), pp: 11116-11131.
[40] Kim, H.-M. (2001). Bioactive Ceramics Challenges and Perspectives, *Journal of the ceramic society of Japan*, C Vol. 109 (1268), pp: S49-S57.
[41] Buchanan, F. and Leonard, D., *Influence of processing, sterilisation and storage on bioresorbability*, in *Degradation Rate of Bioresorbable Materials*2008, Elsevier. p. 209-233.
[42] Kaygili, O., Keser, S., Ates, T., and Yakuphanoglu, F. (2013). Synthesis and characterization of lithium calcium phosphate ceramics, *Ceramics International*, C Vol. 39 (7), pp: 7779-7785.
[43] Dorozhkin, S.V. (2010). Bioceramics of calcium orthophosphates, *Biomaterials*, C Vol. 31 (7), pp: 1465-1485.
[44] de Groot, K. (1993). Clinical applications of calcium phosphate biomaterials: a review, *Ceramics International*, C Vol. 19 (5), pp: 363-366.
[45] de Groot, K., (2018). *Bioceramics Calcium Phosphate*, CRC press,
[46] Dorozhkin, S.V. and Epple, M. (2002). Biological and medical significance of calcium phosphates, *Angewandte Chemie International Edition*, C Vol. 41 (17), pp: 3130-3146.
[47] Barbero, E.J., (2010). *Introduction to composite materials design*, CRC press,
[48] Miracle, D.B. and Donaldson, S.L. (2001). Introduction to composites, *ASM handbook*, C Vol. 21 3-17.
[49] Paital, S.R. and Dahotre, N.B. (2009). Calcium phosphate coatings for bio-implant applications: Materials, performance factors, and methodologies, *Materials Science and Engineering: R: Reports*, C Vol. 66 (1-3), pp: 1-70.
[50] Rogero, S.O., Malmonge, S.M., Lugão, A.B., Ikeda, T.I., Miyamaru, L., and Cruz, Á.S. (2003). Biocompatibility study of polymeric biomaterials, *Artificial organs*, C Vol. 27 (5), pp: 424-427.
[51] Huang, L.L., Sung, H.W., Tsai, C.C., and Huang, D.M. (1998). Biocompatibility study of a biological tissue fixed with a naturally occurring crosslinking reagent, *Journal of Biomedical Materials Research: An Official Journal of The Society for Biomaterials, The Japanese Society for Biomaterials, and the Australian Society for Biomaterials*, C Vol. 42 (4), pp: 568-576.
[52] Shabalovskaya, S.A. (2002). Surface, corrosion and biocompatibility aspects of Nitinol as an implant material, *Bio-medical materials and engineering*, C Vol. 12 (1), pp: 69-109.
[53] Sathishkumar, S., Karthika, A., Surendiran, M., Kavitha, L., and Gopi, D. (2015). Electrodeposition of cerium substituted hydroxyapatite coating on passivated surgical grade stainless steel for biomedical application, *Int. J. ChemTech. Res*, C Vol. 7 533-538.
[54] Boutrand, J.-P., (2019). *Biocompatibility and performance of medical devices*, Woodhead Publishing,

[55] Ramsden, J.J., Allen, D.M., Stephenson, D.J., Alcock, J.R., Peggs, G., Fuller, G., and Goch, G. (2007). The design and manufacture of biomedical surfaces, *CIRP annals*, C Vol. 56 (2), pp: 687-711.
[56] Atala, A., Lanza, R., Mikos, T., and Nerem, R.M., (2018). *Principles of regenerative medicine*, Academic press,
[57] Lowenstam, H.A. and Weiner, S., (1989). *On biomineralization*, Oxford University Press on Demand,
[58] Weiner, S. and Wagner, H.D. (1998). The material bone: structure-mechanical function relations, *Annual review of materials science*, C Vol. 28 (1), pp: 271-298.
[59] Dorozhkin, S.V. (2007). Calcium orthophosphates, *Journal of Materials Science*, C Vol. 42 (4), pp: 1061-1095.
[60] Dorozhkin, S.V. (2009). Calcium Orthophosphates in Nature, Biology and Medicine, *Materials*, C Vol. 2 (2), pp: 399-498.
[61] Ong, J.L. and Chan, D.C. (2000). Hydroxyapatite and their use as coatings in dental implants: a review, *Critical Reviews™ in Biomedical Engineering*, C Vol. 28 (5&6), pp.
[62] Davies, J. (1996). In vitro modeling of the bone/implant interface, *The Anatomical Record: An Official Publication of the American Association of Anatomists*, C Vol. 245 (2), pp: 426-445.
[63] Anselme, K. (2000). Osteoblast adhesion on biomaterials, *Biomaterials*, C Vol. 21 (7), pp: 667-681.
[64] Cao, W. and Hench, L.L. (1996). Bioactive materials, *Ceramics International*, C Vol. 22 (6), pp: 493-507.
[65] Suchanek, W. and Yoshimura, M. (1998). Processing and properties of hydroxyapatite-based biomaterials for use as hard tissue replacement implants, *Journal of Materials Research*, C Vol. 13 (1), pp: 94-117.
[66] Gauthier, O., Bouler, J.M., Weiss, P., Bosco, J., Daculsi, G., and Aguado, E. (1999). Kinetic study of bone ingrowth and ceramic resorption associated with the implantation of different injectable calcium-phosphate bone substitutes, *Journal of Biomedical Materials Research: An Official Journal of The Society for Biomaterials, The Japanese Society for Biomaterials, and The Australian Society for Biomaterials and the Korean Society for Biomaterials*, C Vol. 47 (1), pp: 28-35.
[67] Hing, K., Best, S., and Bonfield, W. (1999). Characterization of porous hydroxyapatite, *Journal of Materials Science: Materials in Medicine*, C Vol. 10 (3), pp: 135-145.
[68] Carotenuto, G., Spagnuolo, G., Ambrosio, L., and Nicolais, L. (1999). Macroporous hydroxyapatite as alloplastic material for dental applications, *Journal of Materials Science: Materials in Medicine*, C Vol. 10 (10), pp: 671-676.
[69] Ezhaveni, S., Yuvakkumar, R., Rajkumar, M., Sundaram, N.M., and Rajendran, V. (2013). Preparation and characterization of nano-hydroxyapatite nanomaterials for liver cancer cell treatment, *Journal of nanoscience and nanotechnology*, C Vol. 13 (3), pp: 1631-1638.
[70] Bhatt, R.A. and Rozental, T.D. (2012). Bone Graft Substitutes, *Hand Clinics*, C Vol. 28 (4), pp: 457-468. doi: https://doi.org/10.1016/j.hcl.2012.08.001.
[71] Roberts, T.T. and Rosenbaum, A.J. (2012). Bone grafts, bone substitutes and orthobiologics, *Organogenesis*, C Vol. 8 (4), pp: 114-124. doi: 10.4161/org.23306.
[72] Wang, W. and Yeung, K.W.K. (2017). Bone grafts and biomaterials substitutes for bone defect repair: A review, *Bioactive Materials*, C Vol. 2 (4), pp: 224-247. doi: https://doi.org/10.1016/j.bioactmat.2017.05.007.
[73] Leventouri, T. (2006). Synthetic and biological hydroxyapatites: crystal structure questions, *Biomaterials*, C Vol. 27 (18), pp: 3339-3342.
[74] Rivera-Muñoz, E.M. (2011). Hydroxyapatite-based materials: synthesis and characterization, *Biomedical Engineering-Frontiers and Challenges*, C Vol. 75-98.
[75] Sønju Clasen, A. and Ruyter, I. (1997). Quantitative determination of type A and type B carbonate in human deciduous and permanent enamel by means of Fourier transform infrared spectrometry, *Advances in Dental Research*, C Vol. 11 (4), pp: 523-527.
[76] Moroni, A., Caja, V.L., Egger, E.L., Trinchese, L., and Chao, E.Y.S. (1994). Histomorphometry of hydroxyapatite coated and uncoated porous titanium bone implants, *Biomaterials*, C Vol. 15 (11), pp: 926-930. doi: https://doi.org/10.1016/0142-9612(94)90119-8.
[77] Maxian, S.H., Zawadsky, J.P., and Dunn, M.G. (1994). Effect of Ca/P coating resorption and surgical fit on the bone/implant interface, *Journal of biomedical materials research*, C Vol. 28 (11), pp: 1311-1319.
[78] Cahyanto, A., Kosasih, E., Aripin, D., and Hasratiningsih, Z. (2017). Fabrication of hydroxyapatite from fish bones waste using reflux method. in *IOP Conference Series: Materials Science and Engineering*. IOP Publishing.

[79] Afshar, A., Ghorbani, M., Ehsani, N., Saeri, M.R., and Sorrell, C.C. (2003). Some important factors in the wet precipitation process of hydroxyapatite, *Materials & Design*, C Vol. 24 (3), pp: 197-202. doi: https://doi.org/10.1016/S0261-3069(03)00003-7.
[80] Song, L., Sun, L., Jiang, N., and Gan, Z. (2016). Structural control and hemostatic properties of porous microspheres fabricated by hydroxyapatite-graft-poly(D,L-lactide) nanocomposites, *Composites science and technology*, C Vol. 134 234-241. doi: https://doi.org/10.1016/j.compscitech.2016.09.001.
[81] Hama, C., Umeda, T., Musha, Y., Koda, S., and Itatani, K. (2010). Preparation of novel hemostatic material containing spherical porous hydroxyapatite/alginate granules, *Journal of the ceramic society of Japan*, C Vol. 118 (1378), pp: 446-450. doi: 10.2109/jcersj2.118.446.
[82] Zhou, H. and Lee, J. (2011). Nanoscale hydroxyapatite particles for bone tissue engineering, *Acta biomaterialia*, C Vol. 7 (7), pp: 2769-2781.
[83] Neacsu, I.A., Stoica, A.E., Vasile, B.S., and Andronescu, E. (2019). Luminescent hydroxyapatite doped with rare earth elements for biomedical applications, *Nanomaterials*, C Vol. 9 (2), pp: 239.
[84] Sadat-Shojai, M., Khorasani, M.-T., Dinpanah-Khoshdargi, E., and Jamshidi, A. (2013). Synthesis methods for nanosized hydroxyapatite with diverse structures, *Acta biomaterialia*, C Vol. 9 (8), pp: 7591-7621.
[85] Chaudhuri, B., Mondal, B., Modak, D.K., Pramanik, K., and Chaudhuri, B.K. (2013). Preparation and characterization of nanocrystalline hydroxyapatite from egg shell and K2HPO4 solution, *Materials Letters*, C Vol. 97 148-150. doi: https://doi.org/10.1016/j.matlet.2013.01.082.
[86] Khoo, W., Nor, F.M., Ardhyananta, H., and Kurniawan, D. (2015). Preparation of Natural Hydroxyapatite from Bovine Femur Bones Using Calcination at Various Temperatures, *Procedia Manufacturing*, C Vol. 2 196-201. doi: https://doi.org/10.1016/j.promfg.2015.07.034.
[87] Ripamonti, U., Crooks, J., Khoali, L., and Roden, L. (2009). The induction of bone formation by coral-derived calcium carbonate/hydroxyapatite constructs, *Biomaterials*, C Vol. 30 (7), pp: 1428-1439. doi: https://doi.org/10.1016/j.biomaterials.2008.10.065.
[88] Vecchio, K.S., Zhang, X., Massie, J.B., Wang, M., and Kim, C.W. (2007). Conversion of bulk seashells to biocompatible hydroxyapatite for bone implants, *Acta biomaterialia*, C Vol. 3 (6), pp: 910-918.
[89] Rivera, E.M., Araiza, M., Brostow, W., Castaño, V.M., Díaz-Estrada, J.R., Hernández, R., and Rodríguez, J.R. (1999). Synthesis of hydroxyapatite from eggshells, *Materials Letters,* C Vol. 41 (3), pp: 128-134. doi: https://doi.org/10.1016/S0167-577X(99)00118-4.
[90] Lee, S.J. and Oh, S.H. (2003). Fabrication of calcium phosphate bioceramics by using eggshell and phosphoric acid, *Materials Letters,* C Vol. 57 (29), pp: 4570-4574. doi: https://doi.org/10.1016/S0167-577X(03)00363-X.
[91] Balázsi, C., Wéber, F., Kövér, Z., Horváth, E., and Németh, C. (2007). Preparation of calcium–phosphate bioceramics from natural resources, *Journal of the European Ceramic Society*, C Vol. 27 (2), pp: 1601-1606. doi: https://doi.org/10.1016/j.jeurceramsoc.2006.04.016.
[92] Cüneyt Tas, A. (2000). Synthesis of biomimetic Ca-hydroxyapatite powders at 37°C in synthetic body fluids, *Biomaterials*, C Vol. 21 (14), pp: 1429-1438. doi: https://doi.org/10.1016/S0142-9612(00)00019-3.
[93] Abdulrahman, I., Tijani, H.I., Mohammed, B.A., Saidu, H., Yusuf, H., Jibrin, M.N., and Mohammed, S. (2014). From garbage to biomaterials: an overview on egg shell based hydroxyapatite, *J. Mater*, C Vol. 2014 802467.
[94] Kumar, G.S., Thamizhavel, A., and Girija, E.K. (2012). Microwave conversion of eggshells into flower-like hydroxyapatite nanostructure for biomedical applications, *Materials Letters*, C Vol. 76 198-200. doi: https://doi.org/10.1016/j.matlet.2012.02.106.
[95] Abdulrahman, I., Tijani, H.I., Mohammed, B.A., Saidu, H., Yusuf, H., Ndejiko Jibrin, M., and Mohammed, S. (2014). From Garbage to Biomaterials: An Overview on Egg Shell Based Hydroxyapatite, *Journal of Materials*, C Vol. 2014 802467. doi: 10.1155/2014/802467.
[96] Türk, S., Altınsoy, İ., ÇelebiEfe, G., Ipek, M., Özacar, M., and Bindal, C. (2017). Microwave–assisted biomimetic synthesis of hydroxyapatite using different sources of calcium, *Materials Science and Engineering: C,* C Vol. 76 528-535. doi: https://doi.org/10.1016/j.msec.2017.03.116.
[97] Gergely, G., Wéber, F., Lukács, I., Tóth, A.L., Horváth, Z.E., Mihály, J., and Balázsi, C. (2010). Preparation and characterization of hydroxyapatite from eggshell, *Ceramics International*, C Vol. 36 (2), pp: 803-806. doi: https://doi.org/10.1016/j.ceramint.2009.09.020.
[98] Rhee, S.-H. (2002). Synthesis of hydroxyapatite via mechanochemical treatment, *Biomaterials*, C Vol. 23 (4), pp: 1147-1152. doi: https://doi.org/10.1016/S0142-9612(01)00229-0.

[99] Sanosh, K.P., Chu, M.-C., Balakrishnan, A., Kim, T.N., and Cho, S.-J. (2009). Utilization of biowaste eggshells to synthesize nanocrystalline hydroxyapatite powders, *Materials Letters*, C Vol. 63 (24), pp: 2100-2102. doi: https://doi.org/10.1016/j.matlet.2009.06.062.
[100] Wu, S.-C., Tsou, H.-K., Hsu, H.-C., Hsu, S.-K., Liou, S.-P., and Ho, W.-F. (2013). A hydrothermal synthesis of eggshell and fruit waste extract to produce nanosized hydroxyapatite, *Ceramics International*, C Vol. 39 (7), pp: 8183-8188. doi: https://doi.org/10.1016/j.ceramint.2013.03.094.
[101] Bernard, L., Freche, M., Lacout, J.L., and Biscans, B. (1999). Preparation of hydroxyapatite by neutralization at low temperature—influence of purity of the raw material, *Powder Technology*, C Vol. 103 (1), pp: 19-25. doi: https://doi.org/10.1016/S0032-5910(99)00009-1.
[102] Guo, G., Sun, Y., Wang, Z., and Guo, H. (2005). Preparation of hydroxyapatite nanoparticles by reverse microemulsion, *Ceramics International*, C Vol. 31 (6), pp: 869-872. doi: https://doi.org/10.1016/j.ceramint.2004.10.003.
[103] Mann, S. and Ozin, G.A. (1996). Synthesis of inorganic materials with complex form, *Nature*, C Vol. 382 (6589), pp: 313-318.
[104] Mann, S., Archibald, D.D., Didymus, J.M., Douglas, T., Heywood, B.R., Meldrum, F.C., and Reeves, N.J. (1993). Crystallization at inorganic-organic interfaces: biominerals and biomimetic synthesis, *Science*, C Vol. 261 (5126), pp: 1286-1292.
[105] Muthukumar, M., Ober, C., and Thomas, E. (1997). Competing interactions and levels of ordering in self-organizing polymeric materials, *Science*, C Vol. 277 (5330), pp: 1225-1232.
[106] Boskey, A., *Will biomimetics provide new answers for old problems of calcified tissues?*, 1998, Springer.
[107] Chang, M.C., Ko, C.-C., and Douglas, W.H. (2003). Preparation of hydroxyapatite-gelatin nanocomposite, *Biomaterials*, C Vol. 24 (17), pp: 2853-2862. doi: https://doi.org/10.1016/S0142-9612(03)00115-7.
[108] İnce, T., Kaygili, O., Tatar, C., Bulut, N., Koytepe, S., and Ates, T. (2018). The effects of Ni-addition on the crystal structure, thermal properties and morphology of Mg-based hydroxyapatites synthesized by a wet chemical method, *Ceramics International*, C Vol. 44 (12), pp: 14036-14043.
[109] Shi, D., (2006). *Introduction to biomaterials*, 清华大学出版社有限公司,
[110] Hahn, B.-D., Lee, J.-M., Park, D.-S., Choi, J.-J., Ryu, J., Yoon, W.-H., Lee, B.-K., Shin, D.-S., and Kim, H.-E. (2010). Aerosol deposition of silicon-substituted hydroxyapatite coatings for biomedical applications, *Thin Solid Films*, C Vol. 518 (8), pp: 2194-2199.
[111] Balamurugan, A., Rebelo, A., Lemos, A., Rocha, J., Ventura, J., and Ferreira, J. (2008). Suitability evaluation of sol–gel derived Si-substituted hydroxyapatite for dental and maxillofacial applications through in vitro osteoblasts response, *Dental Materials*, C Vol. 24 (10), pp: 1374-1380.
[112] Ali, A.F., Alrowaili, Z.A., El-Giar, E.M., Ahmed, M.M., and El-Kady, A.M. (2021). Novel green synthesis of hydroxyapatite uniform nanorods via microwave-hydrothermal route using licorice root extract as template, *Ceramics International*, C Vol. 47 (3), pp: 3928-3937.
[113] Aminian, A., Solati-Hashjin, M., Samadikuchaksaraei, A., Bakhshi, F., Gorjipour, F., Farzadi, A., Moztarzadeh, F., and Schmücker, M. (2011). Synthesis of silicon-substituted hydroxyapatite by a hydrothermal method with two different phosphorous sources, *Ceramics International*, C Vol. 37 (4), pp: 1219-1229.
[114] Tamm, T. and Peld, M. (2006). Computational study of cation substitutions in apatites, *Journal of Solid State Chemistry*, C Vol. 179 (5), pp: 1581-1587.
[115] Lin, K., Liu, P., Wei, L., Zou, Z., Zhang, W., Qian, Y., Shen, Y., and Chang, J. (2013). Strontium substituted hydroxyapatite porous microspheres: surfactant-free hydrothermal synthesis, enhanced biological response and sustained drug release, *Chemical engineering journal*, C Vol. 222 49-59.
[116] Kaygili, O., Keser, S., Bulut, N., and Ates, T. (2018). Characterization of Mg-containing hydroxyapatites synthesized by combustion method, *Physica B: Condensed Matter*, C Vol. 537 63-67.
[117] Ren, F., Leng, Y., Xin, R., and Ge, X. (2010). Synthesis, characterization and ab initio simulation of magnesium-substituted hydroxyapatite, *Acta biomaterialia*, C Vol. 6 (7), pp: 2787-2796.
[118] Sogo, Y., Sakurai, T., Onuma, K., and Ito, A. (2002). The most appropriate (Ca+ Zn)/P molar ratio to minimize the zinc content of ZnTCP/HAP ceramic used in the promotion of bone formation, *Journal of Biomedical Materials Research: An Official Journal of The Society for Biomaterials, The Japanese Society for Biomaterials, and The Australian Society for Biomaterials and the Korean Society for Biomaterials*, C Vol. 62 (3), pp: 457-463.
[119] Ofudje, E.A., Adeogun, A.I., Idowu, M.A., and Kareem, S.O. (2019). Synthesis and characterization of Zn-Doped hydroxyapatite: scaffold application, antibacterial and bioactivity studies, *Heliyon*, C Vol. 5 (5), pp: e01716.

[120] Miyaji, F., Kono, Y., and Suyama, Y. (2005). Formation and structure of zinc-substituted calcium hydroxyapatite, *Materials Research Bulletin*, C Vol. 40 (2), pp: 209-220.
[121] Šupová, M. (2015). Substituted hydroxyapatites for biomedical applications: A review, *Ceramics International*, C Vol. 41 (8), pp: 9203-9231.
[122] Basar, B., Tezcaner, A., Keskin, D., and Evis, Z. (2010). Improvements in microstructural, mechanical, and biocompatibility properties of nano-sized hydroxyapatites doped with yttrium and fluoride, *Ceramics International*, C Vol. 36 (5), pp: 1633-1643.
[123] Sakae, T., Ookubo, A., LeGeros, R.Z., Shimogoryou, R., Sato, Y., Lin, S., Yamamoto, H., and Kozawa, Y. (2003). Bone formation induced by several carbonate-and fluoride-containing apatite implanted in dog mandible. in *Key Engineering Materials*. Trans Tech Publ.
[124] Wieszczycka, K., Staszak, K., Woźniak-Budych, M.J., and Jurga, S. (2019). Lanthanides and tissue engineering strategies for bone regeneration, *Coordination Chemistry Reviews*, C Vol. 388 248-267.
[125] Massari, S. and Ruberti, M. (2013). Rare earth elements as critical raw materials: Focus on international markets and future strategies, *Resources Policy*, C Vol. 38 (1), pp: 36-43.
[126] Lu, Y. and Wang, E. (2010). Rare earth polyoxometalate complexes, *Rare earth coordination chemistry: fundamentals and applications*, C Vol. 193-223.
[127] Vidaud, C., Bourgeois, D., and Meyer, D. (2012). Bone as target organ for metals: the case of f-elements, *Chemical research in toxicology*, C Vol. 25 (6), pp: 1161-1175.
[128] Ciobanu, C.S., Popa, C.L., and Predoi, D. (2016). Cerium-doped hydroxyapatite nanoparticles synthesized by the co-precipitation method, *Journal of the Serbian Chemical Society*, C Vol. 81 (4), pp: 433–446-433–446.
[129] Morais, D., Fernandes, S., Gomes, P., Fernandes, M., Sampaio, P., Ferraz, M.P., Santos, J., Lopes, M., and Hussain, N.S. (2015). Novel cerium doped glass-reinforced hydroxyapatite with antibacterial and osteoconductive properties for bone tissue regeneration, *Biomedical Materials*, C Vol. 10 (5), pp: 055008.
[130] Lin, Y., Yang, Z., and Cheng, J. (2007). Preparation, Characterization and Antibacterial Property of Cerium Substituted Hydroxyapatite Nanoparticles, *Journal of Rare Earths*, C Vol. 25 (4), pp: 452-456. doi: https://doi.org/10.1016/S1002-0721(07)60455-4.
[131] Priyadarshini, B. and Vijayalakshmi, U. (2018). Development of cerium and silicon co-doped hydroxyapatite nanopowder and its in vitro biological studies for bone regeneration applications, *Advanced Powder Technology*, C Vol. 29 (11), pp: 2792-2803.
[132] Alshemary, A.Z., Akram, M., Goh, Y.-F., Kadir, M.R.A., Abdolahi, A., and Hussain, R. (2015). Structural characterization, optical properties and in vitro bioactivity of mesoporous erbium-doped hydroxyapatite, *Journal of Alloys and Compounds*, C Vol. 645 478-486.
[133] Gitty, P., Kailasnath, M., and Nampoori, V.P. (2019). Synthesis, structure and luminescence characterization of erbium doped hydroxyapatite nanoparticles by precipitation method, *Current Physical Chemistry*, C Vol. 9 (3), pp: 218-225.
[134] Sato, M., Sambito, M.A., Aslani, A., Kalkhoran, N.M., Slamovich, E.B., and Webster, T.J. (2006). Increased osteoblast functions on undoped and yttrium-doped nanocrystalline hydroxyapatite coatings on titanium, *Biomaterials*, C Vol. 27 (11), pp: 2358-2369.
[135] Gülgün, M.A., Voytovych, R., Maclaren, I., Rühle, M., and Cannon, R.M. (2002). Cation segregation in an oxide ceramic with low solubility: yttrium doped α-alumina, *Interface Science*, C Vol. 10 (1), pp: 99-110.
[136] Nathanael, A.J., Mangalaraj, D., Hong, S., and Masuda, Y. (2011). Synthesis and in-depth analysis of highly ordered yttrium doped hydroxyapatite nanorods prepared by hydrothermal method and its mechanical analysis, *Materials characterization*, C Vol. 62 (12), pp: 1109-1115.
[137] Owada, H., Yamashita, K., Umegaki, T., Kanazawa, T., and Nagai, M. (1989). Humidity-sensitivity of yttrium substituted apatite ceramics, *Solid State Ionics*, C Vol. 35 (3-4), pp: 401-404.
[138] Owada, H., Yamashita, K., and Kanazawa, T. (1991). High-temperature stability of hydroxyl ions in yttrium-substituted oxyhydroxyapatites, *Journal of materials science letters*, C Vol. 10 (1), pp: 26-28.
[139] Khalid, M. and Mushtaq, A. (2005). Preparation and in vitro stability of (n, γ) yttrium-90 hydroxyapatite, *Applied radiation and isotopes*, C Vol. 62 (4), pp: 587-590.
[140] Cacaina, D., Ylänen, H., Simon, S., and Hupa, M. (2008). The behaviour of selected yttrium containing bioactive glass microspheres in simulated body environments, *Journal of Materials Science: Materials in Medicine*, C Vol. 19 (3), pp: 1225-1233.
[141] Piconi, C. and Maccauro, G. (1999). Zirconia as a ceramic biomaterial, *Biomaterials*, C Vol. 20 (1), pp: 1-25.
[142] Ergun, C., Webster, T.J., Bizios, R., and Doremus, R.H. (2002). Hydroxylapatite with substituted magnesium, zinc, cadmium, and yttrium. I. Structure and microstructure, *Journal of Biomedical*

Materials Research: An Official Journal of The Society for Biomaterials, The Japanese Society for Biomaterials, and The Australian Society for Biomaterials and the Korean Society for Biomaterials, C Vol. 59 (2), pp: 305-311.

[143] Agid, R.S., (2020). *Investigation of the effects of praseodymium doping on the structural properties of hydroxyapatite: An experimental and theoretical study*, *Fen Bilimleri Enstitüsü*. Ph.D. thesis,

[144] Zamani, H.A., Arvinfar, A., Rahimi, F., Imani, A., Ganjali, M.R., and Meghdadi, S. (2011). Praseodymium analysis in aqueous solution by Pr3+–PVC membrane sensor based on N, N′-bis (4-hydroxysalicylidene)-1-3-phenylenediamine, *Materials Science and Engineering: C*, C Vol. 31 (2), pp: 307-312.

[145] Fricker, S.P. (2006). The therapeutic application of lanthanides, *Chemical Society Reviews*, C Vol. 35 (6), pp: 524-533.

[146] Sastri, V., Perumareddi, J., Rao, V.R., Rayudu, G., and Bunzli, J.-C., (2003). *Modern aspects of rare earths and their complexes*, Elsevier,

[147] Wei, G. and Ma, P.X. (2004). Structure and properties of nano-hydroxyapatite/polymer composite scaffolds for bone tissue engineering, *Biomaterials*, C Vol. 25 (19), pp: 4749-4757.

[148] Kalita, S.J., Bhardwaj, A., and Bhatt, H.A. (2007). Nanocrystalline calcium phosphate ceramics in biomedical engineering, *Materials Science and Engineering: C*, C Vol. 27 (3), pp: 441-449.

[149] Mostafa, N.Y. and Brown, P.W. (2007). Computer simulation of stoichiometric hydroxyapatite: Structure and substitutions, *Journal of Physics and Chemistry of Solids*, C Vol. 68 (3), pp: 431-437.

[150] Teixeira, S., Rodriguez, M., Pena, P., De Aza, A., De Aza, S., Ferraz, M., and Monteiro, F. (2009). Physical characterization of hydroxyapatite porous scaffolds for tissue engineering, *Materials Science and Engineering: C*, C Vol. 29 (5), pp: 1510-1514.

[151] Guo, L., Huang, M., and Zhang, X. (2003). Effects of sintering temperature on structure of hydroxyapatite studied with Rietveld method, *Journal of Materials Science: Materials in Medicine*, C Vol. 14 (9), pp: 817-822.

[152] Kantharia, N., Naik, S., Apte, S., Kheur, M., Kheur, S., and Kale, B. (2014). Nano-hydroxyapatite and its contemporary applications, *Bone*, C Vol. 34 (15.2), pp: 1.71.

[153] de Lange, G.L. and Donath, K. (1989). Interface between bone tissue and implants of solid hydroxyapatite or hydroxyapatite-coated titanium implants, *Biomaterials*, C Vol. 10 (2), pp: 121-125. doi: https://doi.org/10.1016/0142-9612(89)90044-6.

[154] Blüthmann, H. (1977). Chromatography of histones on hydroxyapatite columns, *Journal of Chromatography A*, C Vol. 137 (1), pp: 222-227. doi: https://doi.org/10.1016/S0021-9673(00)89262-6.

[155] Venugopal, J., Prabhakaran, M.P., Zhang, Y., Low, S., Choon, A.T., and Ramakrishna, S. (2010). Biomimetic hydroxyapatite-containing composite nanofibrous substrates for bone tissue engineering, *Philosophical Transactions of the Royal Society A: Mathematical, Physical and Engineering Sciences*, C Vol. 368 (1917), pp: 2065-2081.

[156] Prabhakaran, M.P., Venugopal, J., and Ramakrishna, S. (2009). Electrospun nanostructured scaffolds for bone tissue engineering, *Acta biomaterialia*, C Vol. 5 (8), pp: 2884-2893. doi: https://doi.org/10.1016/j.actbio.2009.05.007.

[157] Venugopal, J., Vadgama, P., Kumar, T.S., and Ramakrishna, S. (2007). Biocomposite nanofibres and osteoblasts for bone tissue engineering, *Nanotechnology*, C Vol. 18 (5), pp: 055101.

[158] Palazzo, B., Iafisco, M., Laforgia, M., Margiotta, N., Natile, G., Bianchi, C.L., Walsh, D., Mann, S., and Roveri, N. (2007). Biomimetic hydroxyapatite–drug nanocrystals as potential bone substitutes with antitumor drug delivery properties, *Advanced Functional Materials*, C Vol. 17 (13), pp: 2180-2188.

[159] Loo, S., Moore, T., Banik, B., and Alexis, F. (2010). Biomedical applications of hydroxyapatite nanoparticles, *Current pharmaceutical biotechnology*, C Vol. 11 (4), pp: 333-342.

[160] Library, S.i.C.-B., https://guides.libraries.uc.edu/c.php?g=222784&p=1473460, Access:

[161] Tomberg, A. (2020). Gaussian 09w Tutorial an Introduction to Computational Chemistry Using G09w and Avogadro Software, Vol.

[162] Fischer, C.F. (1987). General hartree-fock program, *Computer physics communications*, C Vol. 43 (3), pp: 355-365.

[163] Abdulsattar, M.A. (2012). SiGe superlattice nanocrystal infrared and Raman spectra: A density functional theory study, *Journal of Applied Physics*, C Vol. 111 (4), pp: 044306.

[164] Kohn, W. (1999). Nobel Lecture: Electronic structure of matter—wave functions and density functionals, *Reviews of Modern Physics*, C Vol. 71 (5), pp: 1253.

[165] Born, M. and Oppenheimer, R. (1927). Zur quantentheorie der molekeln, *Annalen der physik*, C Vol. 389 (20), pp: 457-484.

[166] Van Mourik, T., Bühl, M., and Gaigeot, M.-P., *Density functional theory across chemistry, physics and biology*, 2014, The Royal Society Publishing.
[167] Slater, J.C. (1930). Atomic shielding constants, *Physical Review*, C Vol. 36 (1), pp: 57.
[168] Boys, S.F. (1950). Electronic wave functions-I. A general method of calculation for the stationary states of any molecular system, *Proceedings of the Royal Society of London. Series A. Mathematical and Physical Sciences*, C Vol. 200 (1063), pp: 542-554.
[169] Joiţa, D.-M., Tomescu, M.A., Bàlint, D., and Jäntschi, L. (2021). An Application of the Eigenproblem for Biochemical Similarity, *Symmetry*, C Vol. 13 (10), pp: 1849.
[170] Jäntschi, L. (2019). The eigenproblem translated for alignment of molecules, *Symmetry*, C Vol. 11 (8), pp: 1027.
[171] Abegg, P. and Ha, T.-K. (1974). Ab initio calculation of the spin-orbit coupling constant from gaussian lobe SCF molecular wavefunctions, *Molecular Physics*, C Vol. 27 (3), pp: 763-767.
[172] Binkley, J.S., Pople, J.A., and Hehre, W.J. (1980). Self-consistent molecular orbital methods. 21. Small split-valence basis sets for first-row elements, *Journal of the American Chemical Society*, C Vol. 102 (3), pp: 939-947.
[173] Pietro, W.J., Francl, M.M., Hehre, W.J., DeFrees, D.J., Pople, J.A., and Binkley, J.S. (1982). Self-consistent molecular orbital methods. 24. Supplemented small split-valence basis sets for second-row elements, *Journal of the American Chemical Society*, C Vol. 104 (19), pp: 5039-5048.
[174] Pople, J.A. (1999). Quantum chemical models (Nobel lecture), *Angewandte Chemie International Edition*, C Vol. 38 (13-14), pp: 1894-1902.
[175] Bálint, D. and Jäntschi, L. (2021). Comparison of Molecular Geometry Optimization Methods Based on Molecular Descriptors, *Mathematics*, C Vol. 9 (22), pp: 2855.
[176] Schrödinger, E. (1926). An undulatory theory of the mechanics of atoms and molecules, *Physical Review*, C Vol. 28 (6), pp: 1049.
[177] Diudea, M.V., Gutman, I., and Jantschi, L., (2001). *Molecular topology*, Nova Science Publishers Huntington, NY,
[178] Hohenberg, P. and Kohn, W. (1964). Inhomogeneous electron gas, *Physical Review*, C Vol. 136 (3B), pp: B864.
[179] Petersson, G.A., Malick, D.K., Wilson, W.G., Ochterski, J.W., Montgomery Jr, J.A., and Frisch, M.J. (1998). Calibration and comparison of the Gaussian-2, complete basis set, and density functional methods for computational thermochemistry, *The Journal of chemical physics*, C Vol. 109 (24), pp: 10570-10579.
[180] Spies, M. (1999). Transducer field modeling in anisotropic media by superposition of Gaussian base functions, *The Journal of the Acoustical Society of America*, C Vol. 105 (2), pp: 633-638.
[181] Kayano, M., Dozono, K., and Konishi, S. (2010). Functional cluster analysis via orthonormalized Gaussian basis expansions and its application, *Journal of Classification*, C Vol. 27 (2), pp: 211-230.
[182] Hoffmann, M.R., Martin, S.T., Choi, W., and Bahnemann, D.W. (1995). Environmental applications of semiconductor photocatalysis, *Chemical reviews*, C Vol. 95 (1), pp: 69-96.
[183] Ischenko, A.A., Fetisov, G.V., and Aslalnov, L.A., (2014). *Nanosilicon: properties, synthesis, applications, methods of analysis and control*, CRC Press,
[184] Perdew, J.P., Yang, W., Burke, K., Yang, Z., Gross, E.K., Scheffler, M., Scuseria, G.E., Henderson, T.M., Zhang, I.Y., and Ruzsinszky, A. (2017). Understanding band gaps of solids in generalized Kohn–Sham theory, *Proceedings of the national academy of sciences*, C Vol. 114 (11), pp: 2801-2806.
[185] Dharma, J., Pisal, A., and Shelton, C. (2009). Simple method of measuring the band gap energy value of TiO2 in the powder form using a UV/Vis/NIR spectrometer, *Application note*, C Vol.
[186] 苟高章, 王泽锋, 黄兆龙, 周波, 严和平, and 刘卫. (2016). Gaussian 09 软件在电子圆二色谱教学中的应用, *化学教育*, C Vol. 37 (2), pp: 61-64.
[187] Ahmed, L. and Rebaz, O. (2021). 1H-Pyrrole, Furan, and Thiophene Molecule Corrosion Inhibitor Behaviors, *Journal of Physical Chemistry and Functional Materials*, C Vol. 4 (2), pp: 1-4.
[188] Hegazy, M., Rashwan, S., Kamel, M., and El Kotb, M. (2015). Synthesis, surface properties and inhibition behavior of novel cationic gemini surfactant for corrosion of carbon steel tubes in acidic solution, *Journal of Molecular Liquids*, C Vol. 211 126-134.
[189] Deng, S. and Li, X. (2012). Inhibition by Ginkgo leaves extract of the corrosion of steel in HCl and H2SO4 solutions, *Corrosion Science*, C Vol. 55 407-415.
[190] Muthukumar, N., Ilangovan, A., Maruthamuthu, S., Palaniswamy, N., and Kimura, A. (2009). 1-Aminoanthraquinone derivatives as a novel corrosion inhibitor for carbon steel API 5L-X60 in white petrol–water mixtures, *Materials Chemistry and Physics*, C Vol. 115 (1), pp: 444-452.

[191] Saratha, R. and Vasudha, V. (2009). Inhibition of mild steel corrosion in 1N H2SO4 medium by acid extract of Nyctanthes arbortristis leaves, *E-journal of Chemistry*, C Vol. 6 (4), pp: 1003-1008.
[192] Al-Otaibi, M., Al-Mayouf, A., Khan, M., Mousa, A., Al-Mazroa, S., and Alkhathlan, H. (2014). Corrosion inhibitory action of some plant extracts on the corrosion of mild steel in acidic media, *Arabian Journal of Chemistry*, C Vol. 7 (3), pp: 340-346.
[193] Obot, I., Obi-Egbedi, N., and Umoren, S. (2009). Antifungal drugs as corrosion inhibitors for aluminium in 0.1 M HCl, *Corrosion Science*, C Vol. 51 (8), pp: 1868-1875.
[194] Yıldırım, A. and Çetin, M. (2008). Synthesis and evaluation of new long alkyl side chain acetamide, isoxazolidine and isoxazoline derivatives as corrosion inhibitors, *Corrosion Science*, C Vol. 50 (1), pp: 155-165.
[195] Hansson, C., Mammoliti, L., and Hope, B. (1998). Corrosion inhibitors in concrete—part I: the principles, *Cement and concrete research*, C Vol. 28 (12), pp: 1775-1781.
[196] Abdel-Gaber, A., Abd-El-Nabey, B., Khamis, E., and Abd-El-Khalek, D. (2011). A natural extract as scale and corrosion inhibitor for steel surface in brine solution, *Desalination*, C Vol. 278 (1-3), pp: 337-342.
[197] Salasi, M., Shahrabi, T., Roayaei, E., and Aliofkhazraei, M. (2007). The electrochemical behaviour of environment-friendly inhibitors of silicate and phosphonate in corrosion control of carbon steel in soft water media, *Materials Chemistry and Physics*, C Vol. 104 (1), pp: 183-190.
[198] Blustein, G., Romagnoli, R., Jaén, J., Di Sarli, A., and Del Amo, B. (2006). Zinc basic benzoate as eco-friendly steel corrosion inhibitor pigment for anticorrosive epoxy-coatings, *Colloids and Surfaces A: Physicochemical and Engineering Aspects*, C Vol. 290 (1-3), pp: 7-18.
[199] Bommersbach, P., Alemany-Dumont, C., Millet, J.-P., and Normand, B. (2005). Formation and behaviour study of an environment-friendly corrosion inhibitor by electrochemical methods, *Electrochimica Acta*, C Vol. 51 (6), pp: 1076-1084.
[200] Lecante, A., Robert, F., Blandinières, P., and Roos, C. (2011). Anti-corrosive properties of S. tinctoria and G. ouregou alkaloid extracts on low carbon steel, *Current Applied Physics*, C Vol. 11 (3), pp: 714-724.
[201] Radojčić, I., Berković, K., Kovač, S., and Vorkapić-Furač, J. (2008). Natural honey and black radish juice as tin corrosion inhibitors, *Corrosion Science*, C Vol. 50 (5), pp: 1498-1504.
[202] Omar, R., Koparir, P., and Koparir, M. (2021). Synthesis of 1, 3-Thiazole derivatives, *Indian Drugs*, C Vol. 1 58.
[203] Lashgari, S.M., Yari, H., Mahdavian, M., Ramezanzadeh, B., Bahlakeh, G., and Ramezanzadeh, M. (2021). Synthesis of graphene oxide nanosheets decorated by nanoporous zeolite-imidazole (ZIF-67) based metal-organic framework with controlled-release corrosion inhibitor performance: Experimental and detailed DFT-D theoretical explorations, *Journal of Hazardous Materials*, C Vol. 404 124068.
[204] Singh, A.K. and Quraishi, M. (2010). The effect of some bis-thiadiazole derivatives on the corrosion of mild steel in hydrochloric acid, *Corrosion Science*, C Vol. 52 (4), pp: 1373-1385.
[205] Musa, A.Y., Jalgham, R.T., and Mohamad, A.B. (2012). Molecular dynamic and quantum chemical calculations for phthalazine derivatives as corrosion inhibitors of mild steel in 1 M HCl, *Corrosion Science*, C Vol. 56 176-183.
[206] Yadav, D.K. and Quraishi, M.A. (2012). Application of some condensed uracils as corrosion inhibitors for mild steel: gravimetric, electrochemical, surface morphological, UV–visible, and theoretical investigations, *Industrial & engineering chemistry research*, C Vol. 51 (46), pp: 14966-14979.
[207] Bobina, M., Kellenberger, A., Millet, J.-P., Muntean, C., and Vaszilcsin, N. (2013). Corrosion resistance of carbon steel in weak acid solutions in the presence of l-histidine as corrosion inhibitor, *Corrosion Science*, C Vol. 69 389-395.
[208] El Sayed, H. and Senior, S.A. (2011). QSAR of lauric hydrazide and its salts as corrosion inhibitors by using the quantum chemical and topological descriptors, *Corrosion Science*, C Vol. 53 (3), pp: 1025-1034.
[209] Zhao, H., Zhang, X., Ji, L., Hu, H., and Li, Q. (2014). Quantitative structure–activity relationship model for amino acids as corrosion inhibitors based on the support vector machine and molecular design, *Corrosion Science*, C Vol. 83 261-271.
[210] Rebaz, O., Koparir, P., Qader, I., and Ahmed, L. (2022). Theoretical Determination of Corrosion Inhibitor Activities of Naphthalene and Tetralin, *Gazi University Journal of Science*, C Vol. 1-1.
[211] Omer, R.A., Koparir, P., and Ahmed, L.O. (2022). Characterization and Inhibitor Activity of Two Newly Synthesized Thiazole, *Journal of Bio-and Tribo-Corrosion*, C Vol. 8 (1), pp: 1-12.

[212] Koparir, P., Rebaz, O., Karatepe, M., and Ahmed, L. (2020). Synthesis, Characterization, and theoretical inhibitor study for (1E, 1'E)-2, 2'-thiobis (1-(3-mesityl-3-methylcyclobutyl) ethan-1-one) dioxime, *El-Cezeri*, C Vol. 8 (3), pp: 1495-1510.
[213] Ahmed, L. and Rebaz, O. (2020). Spectroscopic properties of Vitamin C: A theoretical work, *Cumhuriyet Science Journal*, C Vol. 41 (4), pp: 916-928.
[214] Omer, R.A., Koparir, P., Ahmed, L., and Koparir, M. (2021). Computational and spectroscopy study of melatonin, *Indian Journal of Chemistry-Section B (IJC-B)*, C Vol. 60 (5), pp: 732-741.
[215] Bentiss, F., Mernari, B., Traisnel, M., Vezin, H., and Lagrenée, M. (2011). On the relationship between corrosion inhibiting effect and molecular structure of 2, 5-bis (n-pyridyl)-1, 3, 4-thiadiazole derivatives in acidic media: Ac impedance and DFT studies, *Corrosion Science*, C Vol. 53 (1), pp: 487-495.
[216] Ahamad, I., Prasad, R., and Quraishi, M. (2010). Adsorption and inhibitive properties of some new Mannich bases of Isatin derivatives on corrosion of mild steel in acidic media, *Corrosion Science*, C Vol. 52 (4), pp: 1472-1481.
[217] Obot, I. and Gasem, Z. (2014). Theoretical evaluation of corrosion inhibition performance of some pyrazine derivatives, *Corrosion Science*, C Vol. 83 359-366.
[218] Rebaz, O., Koparir, P., Qader, I.N., and Ahmed, L. (2021). Structure reactivity analysis for Phenylalanine and Tyrosine, *Cumhuriyet Science Journal*, C Vol. 42 (3), pp: 576-585.
[219] Ahmed, L. and Rebaz, O. (2021). The Role of the Various Solvent Polarities on Piperine Reactivity and Stability, *Journal of Physical Chemistry and Functional Materials*, C Vol. 4 (2), pp: 10-16.
[220] Omer, L.A. and Anwer, R.O. (2020). Population Analysis and UV-Vis spectra of Dopamine Molecule Using Gaussian 09, *Journal of Physical Chemistry and Functional Materials*, C Vol. 3 (2), pp: 48-58.
[221] Omer, R.A., Ahmed, L.O., Koparir, M., and Koparir, P. (2020). Theoretical analysis of the reactivity of chloroquine and hydroxychloroquine, *Indian Journal of Chemistry-Section A (IJCA)*, C Vol. 59 (12), pp: 1828-1834.
[222] Rebaz, O., Koparir, P., Ahmed, L., and Koparir, M. (2020). Computational determination the reactivity of salbutamol and propranolol drugs, *Turkish Computational and Theoretical Chemistry*, C Vol. 4 (2), pp: 67-75.
[223] Ahmed, L. and Rebaz, O. (2020). Computational Study on Paracetamol Drug, *Journal of Physical Chemistry and Functional Materials*, C Vol. 3 (1), pp: 9-13.
[224] Ahmed, L. and Rebaz, O. (2019). A theoretical study on Dopamine molecule, *Journal of Physical Chemistry and Functional Materials*, C Vol. 2 (2), pp: 66-72.
[225] Becke, A.D. (1996). Density-functional thermochemistry. IV. A new dynamical correlation functional and implications for exact-exchange mixing, *The Journal of chemical physics*, C Vol. 104 (3), pp: 1040-1046.
[226] Beytur, M., Irak, Z.T., Manap, S., and Yüksek, H. (2019). Synthesis, characterization and theoretical determination of corrosion inhibitor activities of some new 4, 5-dihydro-1H-1, 2, 4-Triazol-5-one derivatives, *Heliyon*, C Vol. 5 (6), pp: e01809.
[227] De Araujo, T., De Souza, S., and De Sousa, E. (2010). Effect of Zn2+, Fe3+ and Cr3+ addition to hydroxyapatite for its application as an active constituent of sunscreens. in *Journal of Physics: Conference Series*. IOP Publishing.
[228] Kaygili, O. and Keser, S. (2016). Zr/Mg, Zr/Sr and Zr/Zn co-doped hydroxyapatites: synthesis and characterization, *Ceramics International*, C Vol. 42 (7), pp: 9270-9273.
[229] Yogamalar, R., Srinivasan, R., Vinu, A., Ariga, K., and Bose, A.C. (2009). X-ray peak broadening analysis in ZnO nanoparticles, *Solid State Communications*, C Vol. 149 (43-44), pp: 1919-1923.
[230] Mansour, S., El-Dek, S., Dorozhkin, S., and Ahmed, M. (2017). Physico-mechanical properties of Mg and Ag doped hydroxyapatite/chitosan biocomposites, *New Journal of Chemistry*, C Vol. 41 (22), pp: 13773-13783.
[231] Acar, S., Kaygili, O., Ates, T., Dorozhkin, S.V., Bulut, N., Ates, B., Koytepe, S., Ercan, F., Kebiroglu, H., and Hssain, A.H. (2022). Experimental characterization and theoretical investigation of Ce/Yb co-doped hydroxyapatites, *Materials Chemistry and Physics*, C Vol. 276 125444.
[232] Korkmaz, A.A., Ahmed, L.O., Kareem, R.O., Kebiroglu, H., Ates, T., Bulut, N., Kaygili, O., and Ates, B. (2022). Theoretical and experimental characterization of Sn-based hydroxyapatites doped with Bi, *Journal of the Australian Ceramic Society*, C Vol. 1-13.
[233] Landi, E., Tampieri, A., Celotti, G., and Sprio, S. (2000). Densification behaviour and mechanisms of synthetic hydroxyapatites, *Journal of the European Ceramic Society*, C Vol. 20 (14-15), pp: 2377-2387.

[234] Kim, D.J., Hyun, S.H., Kim, S.G., and Yashima, M. (1994). Effective ionic radius of Y3+ determined from lattice parameters of fluorite-type HfO2 and ZrO2 solid solutions, *Journal of the American Ceramic Society*, C Vol. 77 (2), pp: 597-599.
[235] Wu, M., Song, E., Chen, Z., Ding, S., Ye, S., Zhou, J., Xu, S., and Zhang, Q. (2016). Single-band red upconversion luminescence of Yb 3+–Er 3+ via nonequivalent substitution in perovskite KMgF 3 nanocrystals, *Journal of Materials Chemistry C*, C Vol. 4 (8), pp: 1675-1684.
[236] Jesser, W. and Kuhlmann-Wilsdorf, D. (1967). On the theory of interfacial energy and elastic strain of epitaxial overgrowths in parallel alignment on single crystal substrates, *physica status solidi (b)*, C Vol. 19 (1), pp: 95-105.
[237] Zak, A.K., Majid, W.A., Abrishami, M.E., and Yousefi, R. (2011). X-ray analysis of ZnO nanoparticles by Williamson–Hall and size–strain plot methods, *Solid State Sciences*, C Vol. 13 (1), pp: 251-256.
[238] Venkateswarlu, K., Bose, A.C., and Rameshbabu, N. (2010). X-ray peak broadening studies of nanocrystalline hydroxyapatite by Williamson–Hall analysis, *Physica B: Condensed Matter*, C Vol. 405 (20), pp: 4256-4261.
[239] Erdem, U. and Turkoz, M.B. (2021). La3+ and F− dual-doped multifunctional hydroxyapatite nanoparticles: Synthesis and characterization, *Microscopy Research and Technique*, C Vol. 84 (12), pp: 3211-3220.
[240] Goldberg, M.A., Gafurov, M.R., Murzakhanov, F.F., Fomin, A.S., Antonova, O.S., Khairutdinova, D.R., Pyataev, A.V., Makshakova, O.N., Konovalov, A.A., and Leonov, A.V. (2021). Mesoporous iron (III)-doped hydroxyapatite nanopowders obtained via iron oxalate, *Nanomaterials*, C Vol. 11 (3), pp: 811.
[241] Murzakhanov, F., Mamin, G., Goldberg, M., Knotko, A., Gafurov, M., and Orlinskii, S. (2020). EPR of Radiation-Induced Nitrogen Centers in Hydroxyapatite: New Approaches to the Study of Electron-Nuclear Interactions, *Russian Journal of Coordination Chemistry*, C Vol. 46 (11), pp: 729-737.
[242] Goldberg, M., Protsenko, P., Smirnov, V., Antonova, O., Smirnov, S., Konovalov, A., Vorckachev, K., Kudryavtsev, E., Barinov, S., and Komlev, V. (2020). The enhancement of hydroxyapatite thermal stability by Al doping, *Journal of Materials Research and Technology*, C Vol. 9 (1), pp: 76-88.
[243] Sánchez-Campos, D., Reyes Valderrama, M.I., López-Ortíz, S., Salado-Leza, D., Fernández-García, M.E., Mendoza-Anaya, D., Salinas-Rodríguez, E., and Rodríguez-Lugo, V. (2021). Modulated monoclinic hydroxyapatite: the effect of pH in the microwave assisted method, *Minerals*, C Vol. 11 (3), pp: 314.
[244] Pereira, M., França, D., Araújo, R.C., Silva Filho, E.C., Rigaud, B., Fonseca, M., and Jaber, M. (2020). Amino hydroxyapatite/chitosan hybrids reticulated with glutaraldehyde at different pH values and their use for diclofenac removal, *Carbohydrate polymers*, C Vol. 236 116036.
[245] Waheed, S., Sultan, M., Jamil, T., and Hussain, T. (2015). Comparative analysis of hydroxyapatite synthesized by sol-gel, ultrasonication and microwave assisted technique, *Materials Today: Proceedings*, C Vol. 2 (10), pp: 5477-5484.
[246] Senra, M.R., de Lima, R.B., Souza, D.d.H.S., Marques, M.d.F.V., and Monteiro, S.N. (2020). Thermal characterization of hydroxyapatite or carbonated hydroxyapatite hybrid composites with distinguished collagens for bone graft, *Journal of Materials Research and Technology*, C Vol. 9 (4), pp: 7190-7200.
[247] Mahmood, B.K., Kaygili, O., Bulut, N., Dorozhkin, S.V., Ates, T., Koytepe, S., Gürses, C., Ercan, F., Kebiroglu, H., and Agid, R.S. (2020). Effects of strontium-erbium co-doping on the structural properties of hydroxyapatite: An Experimental and theoretical study, *Ceramics International*, C Vol. 46 (10), pp: 16354-16363.
[248] Speight, J.G. (2005). Inorganic Chemistry, *Lange's Handbook of Chemistry, 16th ed.; McGraw-Hill: New York, NY, USA*, C Vol. 1.128-1.131.
[249] Ibrahimzade, L., Kaygili, O., Dundar, S., Ates, T., Dorozhkin, S.V., Bulut, N., Koytepe, S., Ercan, F., Gürses, C., and Hssain, A.H. (2021). Theoretical and experimental characterization of Pr/Ce co-doped hydroxyapatites, *Journal of Molecular Structure*, C Vol. 1240 130557.
[250] Yasukawa, A., Gotoh, K., Tanaka, H., and Kandori, K. (2012). Preparation and structure of calcium hydroxyapatite substituted with light rare earth ions, *Colloids and Surfaces A: Physicochemical and Engineering Aspects*, C Vol. 393 53-59.
[251] ToolBox, E. (2005). Elements of the Periodic System, Vol.
[252] Rabiei, M., Palevicius, A., Monshi, A., Nasiri, S., Vilkauskas, A., and Janusas, G. (2020). Comparing methods for calculating nano crystal size of natural hydroxyapatite using X-ray diffraction, *Nanomaterials*, C Vol. 10 (9), pp: 1627.

[253] Fluri, A., Pergolesi, D., Roddatis, V., Wokaun, A., and Lippert, T. (2016). In situ stress observation in oxide films and how tensile stress influences oxygen ion conduction, *Nature communications*, C Vol. 7 (1), pp: 1-9.

[254] Clark, S.J., Segall, M.D., Pickard, C.J., Hasnip, P.J., Probert, M.I., Refson, K., and Payne, M.C. (2005). First principles methods using CASTEP, *Zeitschrift für kristallographie-crystalline materials*, C Vol. 220 (5-6), pp: 567-570.

[255] Kaygili, O., Vural, G., Keser, S., Yahia, I., Bulut, N., Ates, T., Koytepe, S., Temuz, M.M., Ercan, F., and İnce, T. (2021). Ce/Sm co-doped hydroxyapatites: synthesis, characterization, and band structure calculation, *Journal of the Australian Ceramic Society*, C Vol. 57 (1), pp: 305-317.

[256] Jiménez-Flores, Y., Suárez-Quezada, M., Rojas-Trigos, J., Lartundo-Rojas, L., Suárez, V., and Mantilla, A. (2017). Characterization of Tb-doped hydroxyapatite for biomedical applications: optical properties and energy band gap determination, *Journal of Materials Science*, C Vol. 52 (17), pp: 9990-10000.

[257] Tsukada, M., Wakamura, M., Yoshida, N., and Watanabe, T. (2011). Band gap and photocatalytic properties of Ti-substituted hydroxyapatite: Comparison with anatase-TiO2, *Journal of Molecular Catalysis A: Chemical*, C Vol. 338 (1-2), pp: 18-23.

[258] Helmenstine, A.M., Ph.D. Elements Listed by Density, *ThoughtCo.*, C Vol.

[259] Koopmans, T. (1934). Über die Zuordnung von Wellenfunktionen und Eigenwerten zu den einzelnen Elektronen eines Atoms, *physica*, C Vol. 1 (1-6), pp: 104-113.

[260] Plakhutin, B.N. and Davidson, E.R. (2009). Koopmans' theorem in the restricted open-shell Hartree−Fock Method. 1. A variational approach, *The Journal of Physical Chemistry A*, C Vol. 113 (45), pp: 12386-12395.

[261] Koparir, P., Omer, R.A., Karatepe, A., and Ahmed, L.O. (2022). Theoretical determination of corrosion inhibitor activities of 4-allyl-5-(pyridin-4-yl)-4H-1, 2, 4-triazole-3-thiol-thione tautomerism, Vol.

[262] Jesudason, E.P., Sridhar, S., Malar, E.P., Shanmugapandiyan, P., Inayathullah, M., Arul, V., Selvaraj, D., and Jayakumar, R. (2009). Synthesis, pharmacological screening, quantum chemical and in vitro permeability studies of N-Mannich bases of benzimidazoles through bovine cornea, *European journal of medicinal chemistry*, C Vol. 44 (5), pp: 2307-2312.

[263] Gökce, H. and Bahçeli, S. (2011). A study on quantum chemical calculations of 3-, 4-nitrobenzaldehyde oximes, *Spectrochimica Acta Part A: Molecular and Biomolecular Spectroscopy*, C Vol. 79 (5), pp: 1783-1793.

[264] Masoud, M.S., Ali, A.E., Shaker, M.A., and Elasala, G.S. (2012). Synthesis, computational, spectroscopic, thermal and antimicrobial activity studies on some metal–urate complexes, *Spectrochimica Acta Part A: Molecular and Biomolecular Spectroscopy*, C Vol. 90 93-108.

[265] Pearson, R.G. (1988). Absolute electronegativity and hardness: application to inorganic chemistry, *Inorganic chemistry*, C Vol. 27 (4), pp: 734-740.

[266] Chen, S., He, B., Liu, Y., Wang, Y., and Zhu, J. (2014). Quantum chemical study of some benzimidazole and its derivatives as corrosion ınhibitors of steel in HCl solution, *Int. J. Electrochem. Sci*, C Vol. 9 5400-5408.

[267] El Adnani, Z., Mcharfi, M., Sfaira, M., Benzakour, M., Benjelloun, A., and Touhami, M.E. (2013). DFT theoretical study of 7-R-3methylquinoxalin-2 (1H)-thiones (RH; CH3; Cl) as corrosion inhibitors in hydrochloric acid, *Corrosion Science*, C Vol. 68 223-230.

[268] Koch, E.C. (2005). Acid-Base Interactions in Energetic Materials: I. The Hard and Soft Acids and Bases (HSAB) Principle–Insights to Reactivity and Sensitivity of Energetic Materials, *Propellants, Explosives, Pyrotechnics: An International Journal Dealing with Scientific and Technological Aspects of Energetic Materials*, C Vol. 30 (1), pp: 5-16.

[269] Kaya, S., Kariper, S.E., Ungördü, A., and Kaya, C. (2014). Effect of some electron donor and electron acceptor groups on stability of complexes according to the principle of HSAB, *Journal of New Results in Science*, C Vol. 3 (4), pp: 1-1.

APPENDICES

APPENDIX- 1:

Figure A. 1. The prepared samples in the oven to dry

Figure A. 2. Hydroxyapatite sample

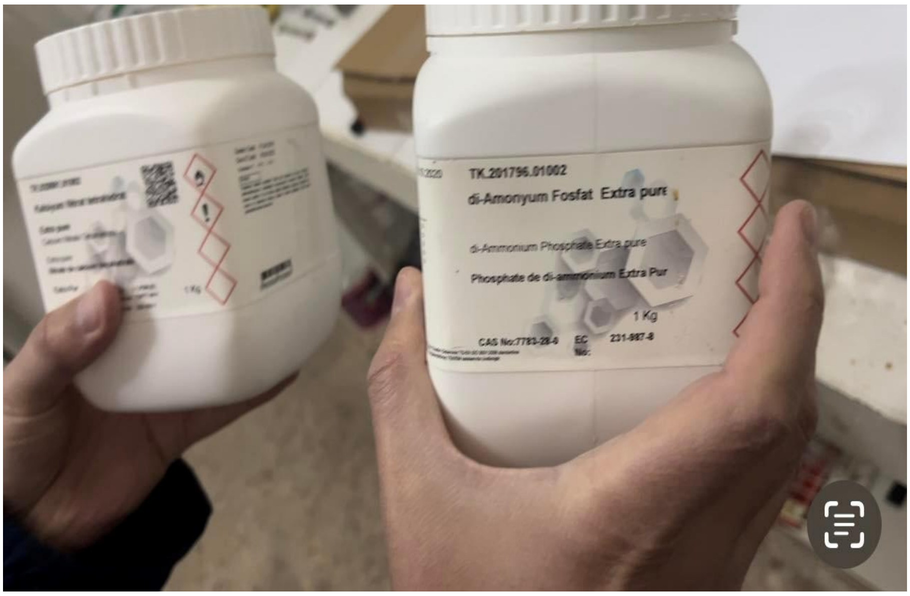

Figure A. 3. Di-ammonium hydrogen phosphate materials

Figure A. 4. Yttrium (III) nitrate hexahydrate material

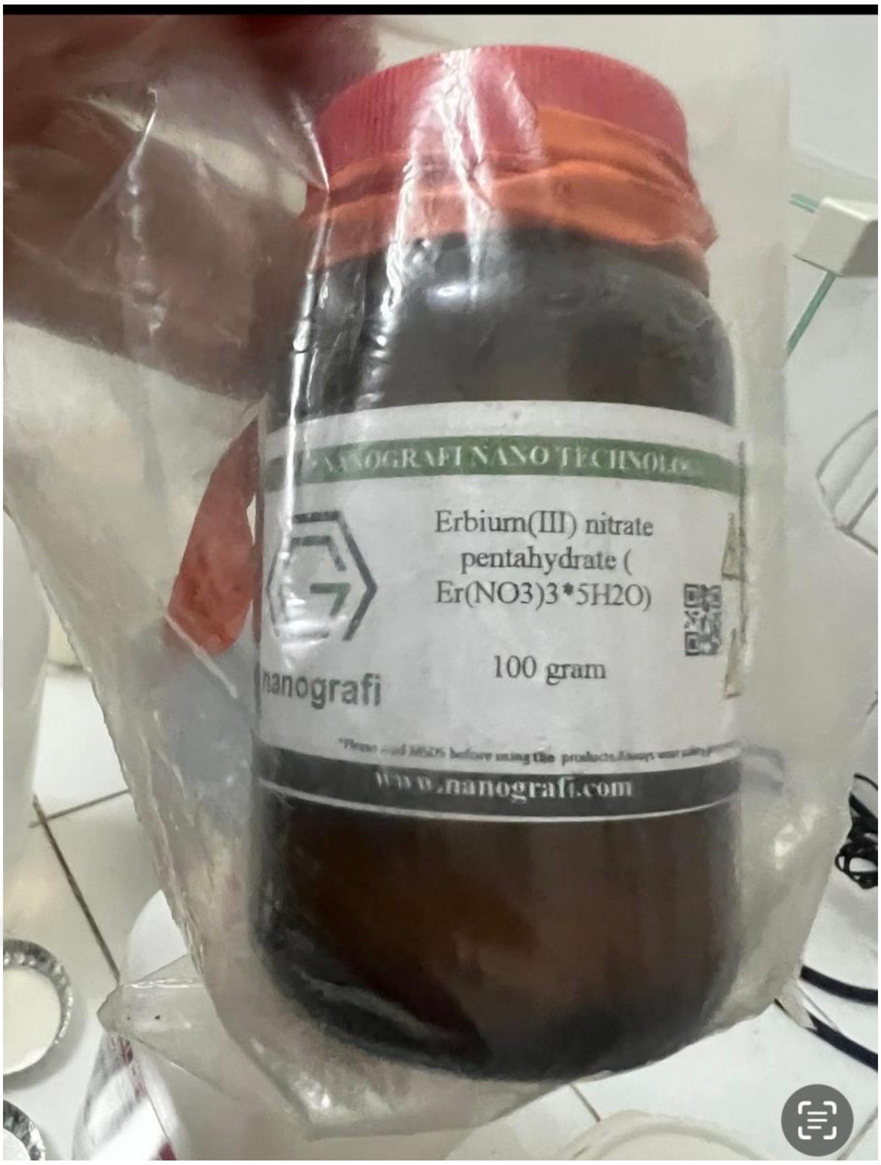

Figure A. 5. Erbium nitrate pentahydrate material

Figure A. 6. Preparing milky solution procedure

CURRICULUM VITAE

Lana Omer Ahmed

[redacted]

[redacted]

[redacted]

[redacted]

[redacted]

ACADEMIC ACTIVITIES

1. Omer, R., Koparir, P., Koparir, M., Rashid, R., Ahmed, L., and Hama, J. (2022). Synthesis, Characterization and DFT Study of 1-(3-Mesityl-3-methylcyclobutyl)-2-((4-phenyl-5-(thiophen-2-yl)-4H-1, 2, 4-triazol-3-yl) thio) ethan-1-one, *Protection of Metals and Physical Chemistry of Surfaces*. 1-13.

2. Ahmed, L.O., Bulut, N., Kebiroglu, H., Alkhedher, M., Ates, T., Koytepe, S., Ates, B., Kaygili, O., and Din, E.M.T.E. (2022). Effects of Yttrium Doping on Erbium-Based Hydroxyapatites: Theoretical and Experimental Study, *Materials*, C Vol. 15 (20), pp: 7211.
3. Koparir, P., Omar, R.A., Sarac, K., Ahmed, L.O., Karatepe, A., Taskin-Tok, T., and Safin, D.A. (2022). Synthesis, Characterization and Computational Analysis of Thiophene-2, 5-Diylbis ((3-Mesityl-3-Methylcyclobutyl) Methanone), *Polycyclic Aromatic Compounds*, Vol. 1-19.
4. Korkmaz, A.A., Ahmed, L.O., Kareem, R.O., Kebiroglu, H., Ates, T., Bulut, N., Kaygili, O., and Ates, B. (2022). Theoretical and experimental characterization of Sn-based hydroxyapatites doped with Bi, *Journal of the Australian Ceramic Society*, Vol. 1-13.
5. Omer, R.A., Koparir, P., and Ahmed, L.O. (2022). Characterization and Inhibitor Activity of Two Newly Synthesized Thiazole, *Journal of Bio-and Tribo-Corrosion*, Vol. 8 (1), pp: 1-12.
6. Rebaz, O., Koparir, P., Qader, I., and Ahmed, L. (2022). Theoretical Determination of Corrosion Inhibitor Activities of Naphthalene and Tetralin, *Gazi University Journal of Science*, C Vol. 1-1.
7. Rebaz, O., Ahmed, L., Qader, I., and Koparir, P. Theoretical Analysis of the Reactivity of Carmustine and Lomustine Drugs, Journal of Physical Chemistry and Functional Materials, Vol. 5 (1), pp: 84-96.
8. Rebaz, O., Ahmed, L., Koparir, P., and Jwameer, H. Impact of Solvent Polarity on the molecular properties of Dimetridazole, *El-Cezeri*, Vol. 9 (2), pp: 740-747.
9. Rebaz, O., Ahmed, L., Jwameer, H., and Koparir, P. Structural Analysis of Epinephrine by Combination of Density Functional Theory and Hartree-Fock Methods, *El-Cezeri*,Vol. 9 (2), pp: 760-776.
10. Koparir, P., Omer, R.A., Karatepe, A., and Ahmed, L.O. (2022). Theoretical determination of corrosion inhibitor activities of 4-allyl-5-(pyridin-4-yl)-4H-1, 2, 4-triazole-3-thiol-thione tautomerism, Vol.
11. Koparir, P., Rebaz, O., Karatepe, M., and Ahmed, L. (2020). Synthesis, Characterization, and theoretical inhibitor study for (1E, 1'E)-2, 2'-thiobis (1-(3-mesityl-3-methylcyclobutyl) ethan-1-one) dioxime, *El-Cezeri*, Vol. 8 (3), pp: 1495-1510.
12. Omer, R.A., Koparir, P., Ahmed, L., and Koparir, M. (2021). Computational and spectroscopy study of melatonin, *Indian Journal of Chemistry-Section B (IJC-B)*, Vol. 60 (5), pp: 732-741.
13. Rebaz, O., Koparir, P., Qader, I.N., and Ahmed, L. (2021). Structure reactivity analysis for Phenylalanine and Tyrosine, *Cumhuriyet Science Journal*, Vol. 42 (3), pp: 576-585.
14. Ahmed, L.O., Al-Arif, M., Chaqmaqchee, F., and Omer, R. (2021). Risk Elements in Drinking Water of Koya City, Vol.
15. Ahmed, L. and Rebaz, O. (2020). Spectroscopic properties of Vitamin C: A theoretical work, *Cumhuriyet Science Journal*, Vol. 41 (4), pp: 916-928.
16. Ahmed, L. and Rebaz, O. (2021). 1H-Pyrrole, Furan, and Thiophene Molecule Corrosion Inhibitor Behaviors, *Journal of Physical Chemistry and Functional Materials*, Vol. 4 (2), pp: 1-4.
17. Ahmed, L. and Rebaz, O. (2021). The Role of the Various Solvent Polarities on Piperine Reactivity and Stability, *Journal of Physical Chemistry and Functional Materials*, Vol. 4 (2), pp: 10-16.
18. Ahmed, L. and Rebaz, O. (2020). Population Analysis and UV-Vis spectra of Dopamine Molecule Using Gaussian 09, *Journal of Physical Chemistry and Functional Materials*, Vol. 3 (2), pp: 48-58.

19. Omer, R.A., Ahmed, L.O., Koparir, M., and Koparir, P. (2020). Theoretical analysis of the reactivity of chloroquine and hydroxychloroquine, *Indian Journal of Chemistry-Section A (IJCA),* Vol. 59 (12), pp: 1828-1834.
20. Rebaz, O., Koparir, P., Ahmed, L., and Koparir, M. (2020). Computational determination the reactivity of salbutamol and propranolol drugs, *Turkish Computational and Theoretical Chemistry*, Vol. 4 (2), pp: 67-75.
21. Ahmed, L. and Rebaz, O. (2020). Computational Study on Paracetamol Drug, *Journal of Physical Chemistry and Functional Materials*, Vol. 3 (1), pp: 9-13.
22. Omer, R.A., Gheni, A.I., Omar, K.A., and Ahmed, L.O. (2019). Antimicrobial Activity of Nylon Nanocomposites Against Staphylococcus Aureus and Escherichia Coli Bacteria, *Science Journal of University of Zakho*, Vol. 7 (4), pp: 138-143.
23. Ahmed, L. and Rebaz, O. (2019). A theoretical study on Dopamine molecule, *Journal of Physical Chemistry and Functional Materials*, Vol. 2 (2), pp: 66-72.